THESE DE DOCTORAT

Université de Lille 1-Science et Technologies

Ecole Doctorale : Science de la Matière, du Rayonnement et de l'Environnement

Discipline : Optique et Laser – Physico-Chimie – Atmosphère

Présenté par

Oleksii LAGUTA

Magneto-optical investigations of Bismuth-doped silica glasses

Soutenue le 19 octobre 2016 devant le jury composé de :

M. Douay	Université Lille 1	Examinateur
T. Amand	Institut National des Sciences Appliquées	Rapporteur
E. Zhukov	Université Technique de Dortmund	Rapporteur
I. Razdobreev	Université Lille 1	Directeur de thèse
M. Bouazaoui	Université Lille 1	Co-directeur de thèse
R. Mahiou	Institute de Chimie de Clermont-Ferrand	Examinateur
H. El Hamzaoui	Université Lille 1	Invité

Etudes magnéto-optiques des verres de silice dopés par le Bismuth

Résumé

Les verres de silice dopés par le Bismuth sont très prometteurs en raison de leurs applications potentielles en termes de lasers à fibres et d'amplificateurs optiques large bande destinés aux télécommunications optiques. Toutefois, la nature des centres optiquement actifs dans de tels verres demeure un sujet d'intenses débats.

Les méthodes spectroscopiques magnéto-optiques sont des outils puissants pour l'étude des centres paramagnétiques au sein de la matière condensée. Dans ce travail de thèse, les techniques de dichroïsme circulaire magnétique, de polarisation circulaire magnétique de l'émission et de résonance magnétique détectée optiquement ont été mises en œuvre pour étudier les verres dopés par le Bismuth.

En association avec les méthodes spectroscopiques conventionnelles, nous avons montré la coexistence d'au moins deux types de centres optiquement actifs dans des verres de silice dopés par le Bismuth sans autres co-dopants et de trois types dans un verre aluminosilicate dopé par la Bismuth. L'analyse des données expérimentales a révélé que tous les centres proviennent de systèmes ayant un nombre pair d'électrons (ou de trous). Deux centres ont été identifiés aux ions Bi^+ et aux défauts du réseau vitreux qui interagissent via des processus de transfert d'énergie. Le troisième centre est attribué aux clusters d'ions Bismuth et a été observé seulement dans des verres aluminosilicates fortement dopés.

Pour la première fois, nous avons montré expérimentalement que l'effet laser dans le proche infrarouge est due à une transition interdite à partir du premier état excité d'un défaut du réseau vitreux.

Mots-clés: bismuth, verre, défaut, luminescence, spectroscopie, effets magnéto-optiques, résonance magnétique.

Magneto-optical investigations of Bismuth-doped Silica glasses

Abstract

Bismuth-doped silica glasses are interesting due to the promising applications in fiber lasers and amplifiers for the communication purposes. Unfortunately, the nature of the optical active centre(s) in such glasses is still a subject of intense debuts.

Magneto-optical methods of spectroscopy are very powerful tools for the investigation of paramagnetic centres in condensed matters. In this thesis, the magnetic circular dichroism, magnetic circular polarization of luminescence and optically detected magnetic resonance techniques were implemented to investigate Bi-doped silica glasses.

Together with the methods of the conventional optical spectroscopy, we demonstrate the coexistence of at least two types of optical centres in a Bi-doped silica glass without other co-dopants and three types in a Bi-doped aluminosilicate glass. The analysis of experimental data revealed that all centres originate from systems with an even number of electrons (or holes). Two centres were identified as Bi^+ ion and some defect in the glass network that interact via the energy transfer processes. The third centre is assigned to the clusters of Bi ions and it was observed only in the highly doped aluminosilicate sample.

For the first time, we showed experimentally that the lasing related near-infrared luminescence is caused by a forbidden transition from the first excited state of the defect centre.

Keywords: bismuth, glass, defect, luminescence, spectroscopy, magneto-optical effects, magnetic resonance.

Acknowledgements

This work was performed in the laboratory of Physics of Laser, Atoms and Molecules of University of Lille 1, therefore I am deeply thankful to the directorate for the given opportunity.

I am very grateful to the thesis committee for accepting to be the jury of my Ph.D. defence and useful discussion.

Many thanks to my supervisors, Igor Razdobreev and Mohamed Bouazaoui, for their priceless guidance and help. Thanks to them I have obtained important new knowledge and skills.

Also I appreciate sincerely my family and friends for their support not only during these three years of my PhD study.

And last but not least, I express my special thanks to Boris Denker and Hicham El Hamzaoui for fabrication and providing of samples, otherwise this work would be impossible.

List of Abbreviations

ES	excited state
ESR	electron spin resonance
FS	fine structure
GS	ground state
hf	hyperfine
lcp	left circularly polarized light
LIA	lock-in amplifier
LWPF	long wave pass filter
MCD	magnetic circular dichroism
MCPL	magnetic circular polarization of luminescence
MF	magnetic field
MW	microwave
NIR	near-infrared
ODC	oxygen-deficiency centre
ODMR	optically detected magnetic resonance
PEM	photoelastic modulator
PL	photoluminescence
PMT	photomultiplier
rcp	right circularly polarized light
SNS	spin noise spectroscopy
UV	ultraviolet
ZFS	zero-field splitting

x

Contents

List of Figures

List of Tables

Chapter 1

Introduction

Information is one of the most important and valuable phenomena of our world. "As a general rule, the most successful man in life is the man who has the best information" said Benjamin Disraeli [1]. Like any other thing of value, information needs some ways or channels to be distributed among humanity. In the early 1840s Daniel Colladon and Jacques Babinet [2, 3] proposed to use the total internal reflection for guiding and confining light — the basic guiding mechanism in an optical fiber. Only in the second half of the 20th century the technology development allowed the commercial production of optical fibers with essentially low propagating losses ($\simeq$1 dB/km), which led to the new communication era.

Modern optical fibers almost always are made from the high purity silica glass. This material has the lowest light attenuation near $1.5\,\mu$m. For this reason the near-infrared (NIR) spectral region is used for the communication purposes. However some other materials, such as fluoride, phosphate and chalcogenide glasses, etc., are used for applications in the mid-infrared. The doping with laser-active ions, for example rare-earth ions, allows the fabrication of fiber lasers and amplifiers. Such devices are widely used not only in communications, but in material processing, medicine, science as well [4].

Nowadays a huge number of high power and highly efficient fiber lasers and amplifiers has been developed. These devices are based on the rare-earth doped

fibers. Fig. 1.1 illustrates the operating spectral ranges of some rare-earth based amplifiers. They have a relatively narrow operating spectral range, which do not completely cover the near-infrared region. Moreover, Praseodymium doped fiber lasers have low efficiency, the maximal value around 1% was reported by Guy et al. [5]. At the same time, the spectral region around $1.3\,\mu$m is important due
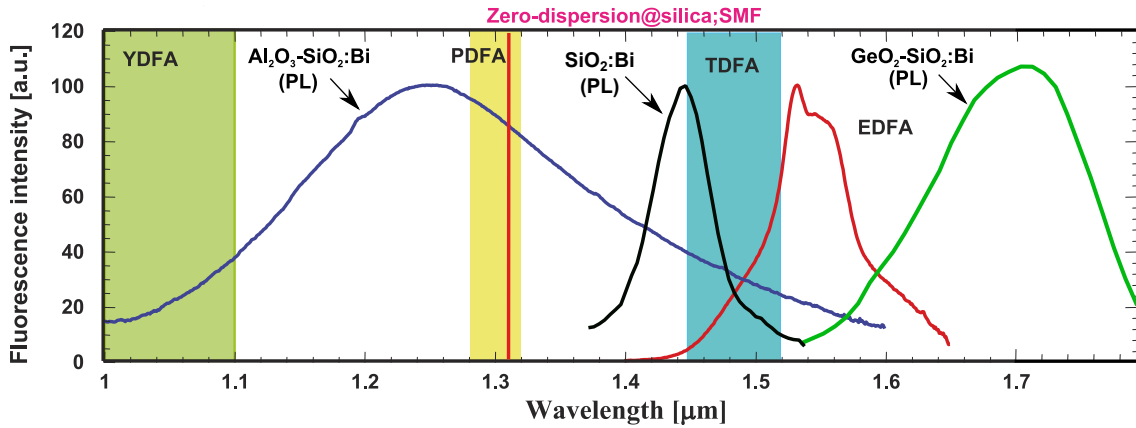
FIGURE 1.1: The operating spectral ranges of the rare earth (Yb, Pr, Tm and Er) doped fiber amplifiers and the examples of PL spectra of Bismuth-doped alumino-, germanosilicate and pure silica glasses [6–9].

to the promising application in the fiber communication (silica glass has zero-dispersion at 1300 nm [10]), bioimaging [11] and phosphors [12].

In contrast to the rare-earth, Bismuth doped glasses exhibit broadband (several hundreds of nm) photoluminescence (PL) in the range of 1100-1600 nm [13]. The characteristic decay time of this luminescence is rather long (millisecond range). Also it is strongly affected by the co-dopants, for example it is possible to shift the NIR PL band in a wide range, as it is shown in Fig. 1.2 [7–9, 13–15]. The introduction of co-dopants in the silica matrix usually causes the shift of the NIR PL band to the short-wavelength region. All these experimental facts show the possibility of using Bi-doped glasses as an active medium for fiber lasers and amplifiers in NIR.
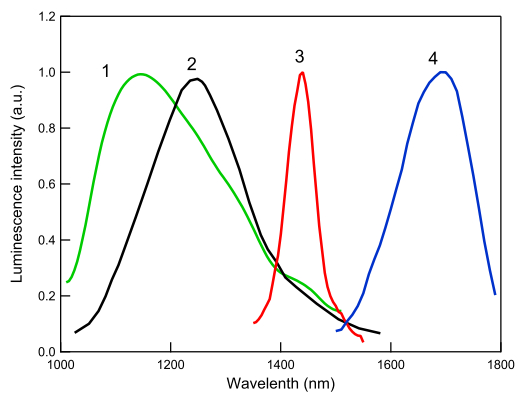
FIGURE 1.2: The influence of co-dopants on NIR PL properties of Bi-doped silica glass. 1 – aluminosilicate [8], 2 – phosphosilicate [15], 3 – pure silica [9], 4– germanosilicate [6]

For the first time, the continuous wave lasing with efficiency of 14.3% at 1215 nm in Bi-doped aluminosilicate glass fiber was demonstrated by Dianov et al. [16] in 2005. Nowadays, the lasing is obtained in the following types of Bismuth-doped silica fibers [13]: germanosilicate, aluminosilicate, aluminogermanosilicate, phosphosilicate and pure silica.

Despite this significant progress in the fabrication of Bi-doped fiber lasers and amplifiers, there is still a need to elucidate several points. First, the amplification and lasing were observed only in the fibers with low doping levels. As a consequence sufficiently long fibers are necessary for the achievement of efficient devices. Another problem is a relatively low efficiency of these lasers and amplifiers comparing to their rare-earth analogues. Finally, the poor understanding of the nature of this NIR photoluminescence (PL) is the major fundamental problem which remains the subject of intense controversies [17]. The different hypothesis on the origin of the NIR PL can be summarized in three main groups:

- Bismuth in higher valency (Bi^{5+} and related molecules) [7, 8]

- Bismuth in lower valency and related molecules (Bi^+, Bi^0, BiO, Bi_2^- dimers . . .) [18–27]

- Point defects [28–32]

Also, it is possible that the NIR emitting system may result from several interacting defects.

The main aim of this thesis is to contribute to the elucidation of the origin of NIR PL in Bismuth-doped silica glasses. Since the conventional optical spectroscopy is not able to solve this problem, one of the goals of the thesis was the implementation of advanced spectroscopical techniques, namely the magnetic circular dichroism (MCD), magnetic circular polarization of luminescence (MCPL) and optically detected magnetic resonance (ODMR), for experimental investigations of Bi-doped silica glasses.

All these techniques are based on the Zeeman effect which consists in the splitting of energy levels of atoms or ions by a magnetic field (MF). Because of the relative technical simplicity and the richness of information that can be obtained, the non-resonance methods (MCD and MCPL) are widespread. The investigation of temperature and MF dependences provides a valuable information about the ground (GS) and excited (ES) states, such as spin multiplicity, g-factor, zero-field splitting (ZFS) [33–35]. The implementation of the photon counting technique to study MCPL can provide some information about the correlation of the ES's lifetime and spin-lattice relaxation time [36]. The only disadvantage of MCD and MCPL is their low accuracy compared to the magnetic resonance techniques. In general, ODMR can be observed in the absorption and emission as well [37, 38]. The amplitude modulation of microwave (*mw*) radiation allows the direct measurement of the spin-lattice relaxation time [37, 39]. However, in the case of ES measurements some cautions must be taken into account. The spin-lattice relaxation time has to be less than the lifetime of this ES. Otherwise the ODMR signal recovery (after the applied microwave pulse) may result from the optical re-population of this excited state.

The thesis begins with a brief review of hypotheses on the origin of the NIR PL in Bi-doped glasses (Chapter 2). The theoretical aspects of the established techniques are given in Chapter 3. The methodology of the experimental data analysis is explained as well in this Chapter. Chapter 4 is devoted to the description of

the experimental setups for MCD and MCPL measurements and the specifics of the signal acquisition and data processing. The results of MCD/MCPL investigations in Bismuth doped aluminosilicate and pure silica glasses are presented in Chapters 5 and 6, respectively, and the theoretical models of the luminescent centres in these glasses are suggested. Chapter 7 describes the ODMR spectrometer operating in the microwave V band (58–62 GHz) and the results of experiments on Bi-doped aluminosilicate. The final chapter gives conclusions and prospects.

Chapter 2

Review of hypotheses of Near-infrared photoluminescence origin

Since the first report on the near-infrared photoluminescence (NIR PL) in Bi-doped silica glass in 1999 [40] the nature of this PL remains unclear and it is a subject of spirited discussion [17]. In this section the hypothesis of the origin of NIR PL in Bi-doped glasses are reviewed.

2.1 $\mathbf{Bi}^{5+}$

The first attempts to observe the ESR (X-band, liquid nitrogen) in Bi-doped aluminosilicate glass was performed by Fujimoto et al. [7]. Since no ESR signal was observed they excluded the defects with unpaired electron, such as E$'$ centres, non-bridging oxygen hole centres, etc [41]. Also they excluded diamagnetic B$_2$-centre (also known as ODC(II)) because no visible luminescence was observed under $250\,\mathrm{nm}$ ($\equiv$Si–Si$\equiv$) excitation [41]. For this reason they suggested that the NIR emission is caused by Bi^{5+} ion. This ion has the singlet ground state, $^1S_0$ term, and it cannot produce any ESR signal.
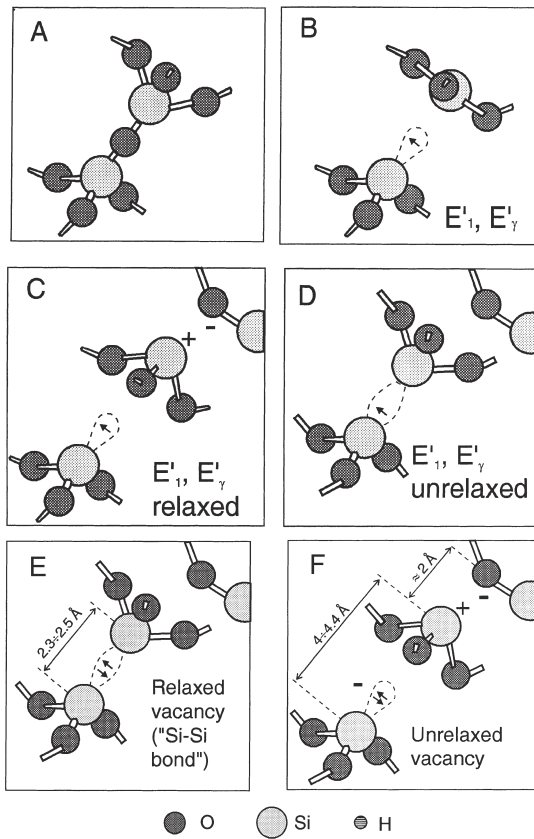
FIGURE 2.1: Some models of E′ and ODC(I,II) defect centres in silica. (A) Fragment of a perfect lattice, (B) "classical" model, refined model in the stable (C) and metastable (D) configurations of E′ centre; structure of ODC(I) (E) and ODC(II) (F) defects. Adapted from [41]

To find evidences of Bi^{5+} presence in Bismuth-doped glasses Fujimoto et. al [8] used the extended X-ray absorption fine structure (EXAFS) technique and X-ray photoelectron spectroscopy (XPS). As reference materials, that contain Bi^{5+}, Bi^{3+} and Bi^0, they used $NaBiO_3$, α-Bi_2O_3 and Bi-metal, respectively. EXAFS experiments have shown that the Bi-O distances of the first and second coordination spheres in Bi-doped samples match those in the reference ($NaBiO_3$ and α-Bi_2O_3) samples. Thus, the coexistence of Bi^{5+} and Bi^{3+} in Bi-doped aluminosilicate glass was concluded. According to the Bi ($4f_{5/2}$, $4f_{7/2}$) peaks position in XPS experiments the bonding energies (BE) were sorted to the increasing sequence, as follows:

$$BE(Bi\text{-metal}) < BE(Bi_2O_3) < BE(NaBiO_3) = BE(Bi\text{-doped glass})$$

Because the bonding energy usually increases with the valence state, this result seems to be reasonable and, Y. Fujimoto concluded that the investigated Bi-doped samples contain Bi^{5+} ions.

There are several experimental facts against the Bi^{5+} hypothesis. It is worth noting among them the following:

- At high temperatures, i.e. melting temperature of the silica glass, Bi_2O_3 reduces to Bi and forms Bismuth clusters and/or nanoparticles [24, 27].

- In the stable state Bi^{5+} ions often exist in compounds with alkali or alkaline earth content ($LiBiO_3$, $NaBiO_3$, $KBiO_3$, etc.) [22]. Nevertheless, Bi^{5+} easily reduces, due to its decomposition, to Bi^{3+} by heating above 300 °C, that is significantly lower than the melting temperature of Bi-doped glasses.

2.2 Bi$^+$
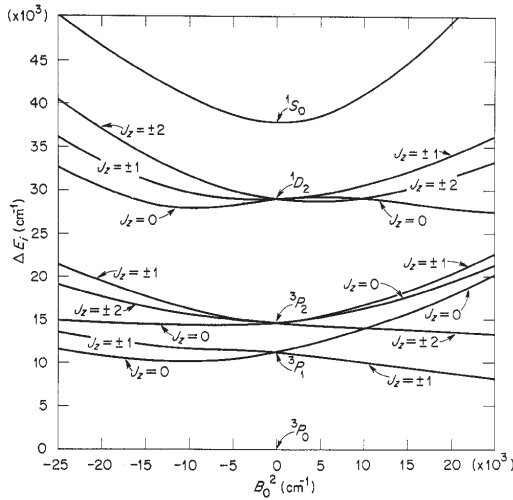
FIGURE 2.2: Ligand field energy levels of a p^2 configuration as a function of the crystal field parameter B_0^2. After [42].

Meng et al. [18] suggested Bi^+ ion as an optically active centre responsible for the NIR PL in aluminophosphate glass. It is also the ESR non-active ion (ground state term is $^3P_0$) and they assigned the observed absorption peaks at $\simeq$500 (20000 cm^{-1}), $\simeq$700 (15000 cm^{-1}), $\simeq$800 (12500 cm^{-1}) and $\simeq$1000 nm (10000 cm^{-1}) to the transitions $^3P_0 \longrightarrow {}^1S_0$, $^1D_2$, $^3P_2$ and $^3P_1$, respectively, NIR PL being caused by $^3P_1 \longrightarrow {}^3P_0$ transition. Later this hypothesis was used to explain the NIR emission in Bi-doped single crystals [43–46] and silicate glasses [19–21]. In Fig. 2.2 we show the crystal field dependence of energy levels of Bi^+ ion. It is seen that levels $^1S_0$ and $^1D_2$ lie above 30000 cm^{-1} and they cannot cause the absorption at $\sim$500 and $\sim$700 nm. If we assume that the NIR PL originates from the $J_z = \pm 1$ multiplet of $^3P_1$ state, the next allowed transition will occur at $\simeq$500 nm [47]. Moreover, in the case of the Bismuth doped silica

glass without other co-dopants the energy of the first ES is $\simeq$7000 cm^{-1} (1400 nm) [48]. The situation is even worse in GeO_2 glass where the first excited state was found at 6000 cm^{-1} ($\simeq$1660 nm) [15].

2.3 BiO

Ren et. al [22] investigated the influence of various alkaline-earth metal oxides on the NIR PL in Bi-doped silicate glasses. They observed NIR emission in the range of 1000–1600 nm. The authors showed that the intensity and position of this PL can be adjusted by the selection of the alkaline-earth metal oxide in the glasses. On the other hand, it is known that BiO molecules in gas phase emit in the NIR spectral region due to the $X_2{}^2\Pi_{3/2} \longrightarrow X_2{}^2\Pi_{1/2}$ transition [49]. Based on the similarity of these two NIR emissions, Ren et al. concluded that the BiO molecules are responsible for the NIR PL in Bi-doped glasses. Murata et al. [23] followed this approach. They concluded that the adding of Al_2O_3 in the melt favours the Bi clusters decomposition and, as a consequence, increases the BiO concentration. At the same time, further experiments on Bi/Dy co-doped chalco-halide glasses have contradicted this hypothesis due to the absence of oxygen [50].

2.4 Bi dimers

Khonthon et al. [24] reported on the ESR signals with $g \approx 2.2$ and $g \approx 4.7$ in Bi- and Te-doped oxide glasses and glass-ceramics. The signal corresponding to $g \approx 2.2$ appeared only in the NIR emitting samples, i.e. pink coloured zinc aluminosilicate oxide glass and glass-ceramics. In contrast the second ESR signal was detected in all samples and may be derived from impurities, e.g. Fe^{3+}. So, Khonton et al. concluded that the ESR signal at $g \approx 2.0$ was related to the NIR

emitting centre. Since ESR spectra in Bi-doped and Te^{2-} containing glasses had similar structure, the detected signal was attributed to Bi$_2^-$, and Bi$_2$/Bi$_2^-$ dimers were proposed as the origin of NIR PL.

To verify this hypothesis Sokolov et al. [25] performed quantum-chemical calculations of electronic states of Bi$_2^-$ and Bi$_2^{2-}$ dimers in aluminosilicate network. The results showed that such dimers indeed can cause NIR PL, they have similar spectra of NIR luminescence and an indexation of transition bands was performed. Since Bi$_2^-$ has unpaired electron, it can produce ESR signal and the corresponding g-factor was calculated. The authors found $g \approx 2.19$ which was in a good agreement with that obtained by Khonton et al. [24]. Also, Sokolov et al. observed NIR PL in Bi-doped magnesium cordierite (2MgO-2Al$_2$O$_3$-5SiO$_2$) [25]. Schwartz et al. [51] showed that in Bismuth doped magnesium cordierite two Bi atoms, being located at neighbouring sites, can form Bi$_2$ dimers. The glass composition and preparation conditions dramatically change the concentration ratio of Bi$_2^-$/Bi$_2^{2-}$. Thus, in this model the absence of ESR signal can be explained by the low Bi$_2^-$ concentration.

One more evidence in favour of Bi dimers hypothesis is the quadratic dependence of the absorption coefficient on the Bismuth concentration observed by Denker et al. [26, 52, 53]. Moreover, they found out that the total charge of two Bi ions forming a dimer is equal +5. Taken into account these results and the spectral similarity with irradiated Pb-doped crystals Dianov [54] suggested Bi$^{2+}-$Bi^{3+} dimer as a possible origin of NIR PL.

2.5   Bi^0

Peng et al. [27] investigated the influence of the melting temperature on the absorption and emitting properties of bismuthate glasses. They concluded that

Bi_2O_3 decomposes to the elementary Bi atoms. The increasing of melting temperature stimulates this process and the intensity of NIR PL increases. Therefore the Bi^0 was proposed as a possible origin of this PL. Also, the absorption and emission properties of Bi-doped glasses have better matching with those of Bi^0 than Bi^+. Absorption bands at 320, 500, 700, 800 and 1000 nm were assigned to $^4S_{3/2} \longrightarrow {}^2P_{3/2}$, $^4S_{3/2} \longrightarrow {}^2P_{1/2}$, $^4S_{3/2} \longrightarrow {}^2D_{5/2}$, $^4S_{3/2} \longrightarrow {}^2D_{3/2}(2)$ and $^4S_{3/2} \longrightarrow {}^2D_{3/2}(2)$, respectively, and NIR PL to $^2D_{3/2} \longrightarrow {}^4S_{3/2}$ ($^2D_{3/2}(1,2)$ — two crystal-field split sublevels of $^2D_{3/2}$ state). It is worth noting that the ground state $^4S_{3/2}$ is degenerated and the ESR signal could be detected. Nevertheless, the observation of the ESR signal was not reported.

2.6 Defects in the glass network

Sharonov et al. [28, 55] performed spectroscopical study of Bi-, Pb-, Sb-, Sn-, Te and In-doped germanate glasses. The authors found that all samples (except Te- and In-doped) exhibit similar absorption and emission properties and decay times of luminescence. Also, they observed that the decay consists of a main long- and several short-lived components. It was concluded that these fast components are not the initial stage of the main decay but they are related to different optical centres. The authors emphasized that Bi and Pb belong to 9th row of the Periodic Table while Sb and Sn — to 7th. In their opinion it is doubtful that the elements from different rows may have similar optical bands because of significant difference in the spin-orbit coupling constants. For this reason they suggested to consider the point defects and localized states in glasses as a possible origin of NIR PL.

Dianov [32] followed this idea and by the analogy with Tl- and Pb-doped crystals supposed that the three types of centres could be considered as the origin of

NIR PL: Bi^{2+} ion + oxygen vacancy, $Bi^{2+}-Bi^{3+}$ dimer with Bi ion adjacent to oxygen vacancy and Bi^+ ion flanked by a pair of oxygen vacancy. The appearance of these centres strongly depends on the glass composition and preparation conditions. The E$'$ centre (oxygen vacancy with a trapped hole) is paramagnetic, thus it is not considered. So the author decided in favour of the "Bi ion + ODC(I,II)" structure (see common models of ODC centres in Fig. 2.1). The ODC (II) defect has an absorption band at $\lambda = 242$ nm and under this excitation transforms to the E$'$ centre [41]. Indeed, Dianov et al. [32] have shown that after the treatment of Bi-doped germanosilicate fiber with 244 nm laser radiation the intensity of the NIR luminescence while excited at 1460 nm significantly decreased compared to the pristine sample. The significant enhancement of the background loss level of absorption author explained by the UV absorption bands of E$'$- and other induced centres. In our opinion, it is necessary to perform additional, magnetic resonance related experiments before make any definitive conclusions.

According to the model of Dianov, Sokolov et al. [30, 31] performed calculations of different Bi-related centres in SiO_2, GeO_2, $Al_2O_3-GeO_2$ and $Al_2O_3-SiO_2$ hosts. Based on the matching of the calculated and measured transition bands the authors supposed that Bi–ODCs are most likely responsible for the NIR PL. Leaving aside the criticism of the methods of calculations one can note that the GS of this model centre is doubly degenerate with total angular momentum J = 1/2 (See Fig.3 in [31]). It means that the centre must be ESR active, that is in the contradiction with experiments [7, 56].

The detailed research work on the NIR PL in Ga/Bi co-doped silica glass at extremely low doping was performed by Razdobreev et al. [29]. In the time resolved experiments they observed unusual decay kinetics in both visible and NIR regions. Such kinetics can occur due to the energy transfer by dipole-dipole, dipole-quadrupole and quadrupole-quadrupole interactions between the donor and acceptor. The fitting of kinetic curves put in evidence the energy transfer

caused by the quadrupole-quadrupole interaction. Based on these results Razdo-breev et al. proposed the model of two interacting centres. One of these centres is Bi+ ion while the second one is presumably some lattice defect. Obviously, these centres do not form a single centre, i.e. molecule.

2.7 Conclusions

It is seen from the above short review, that despite the significant number of experimental and theoretical results, there is no consensus among researchers regarding the nature of NIR PL in the various Bi-doped glasses. Moreover, some experimental observations appear contradictory. It is well known that not only the sample composition, but also preparation conditions considerably influence its optical properties. Furthermore, it is possible to assume that the different Bi-doped systems may have different optical centres. As a consequence, the new advanced experiments are highly desirable to clarify the nature of the luminescent centres in Bi-doped glasses.

Chapter 3

Experimental techniques (Theoretical aspects)

The magneto-optical methods (MCD, MCPL, ODMR, etc.) are based on the Zeeman effect. Unfortunately, the number of textbooks on magneto-optical effects and their application in physics of solid state is very limited. For this reason in this chapter the introduction to the physical principles and theoretical aspects of MCD, MCPL and ODMR techniques is given.

3.1 Zeeman effect and spin Hamiltonian

In general, Zeeman effect means the splitting of energy levels of a paramagnetic species by a magnetic field. In the simplest case of a free atom (ion) with the electronic magnetic dipole moment $\boldsymbol{\mu_J} = -g_J \mu_B \boldsymbol{J}$ the Hamiltonian of its interaction with a magnetic field $\boldsymbol{B}$ is:

$$\mathscr{H} = -(\boldsymbol{\mu_J}.\boldsymbol{B}) = g_J \mu_B (\boldsymbol{B}.\boldsymbol{J}),\qquad(3.1)$$

where g_J is a Landé g-factor of the electronic state with an angular momentum $\boldsymbol{J}$, μ_B is the Bohr magneton and $\boldsymbol{B}$ is a magnetic field.

The energy of a stationary state with a magnetic quantum number $M_J = J, J-1, \ldots, -J$ in a magnetic field $\boldsymbol{B}$ is:

$$W = g_J \mu_B B M_J \tag{3.2}$$

Therefore an external magnetic field removes the degeneracy and the energy separation between levels increases linearly with MF increase, as it is shown in Fig. 3.1. However, this simple form of (3.1) and (3.2) is valid only if:

- (2J+1) levels are degenerated when $B = 0$;

- the groups of (2J+1) levels with different J are well separated, i.e. Zeeman energy is much less than the energy interval to the nearest level or group of levels
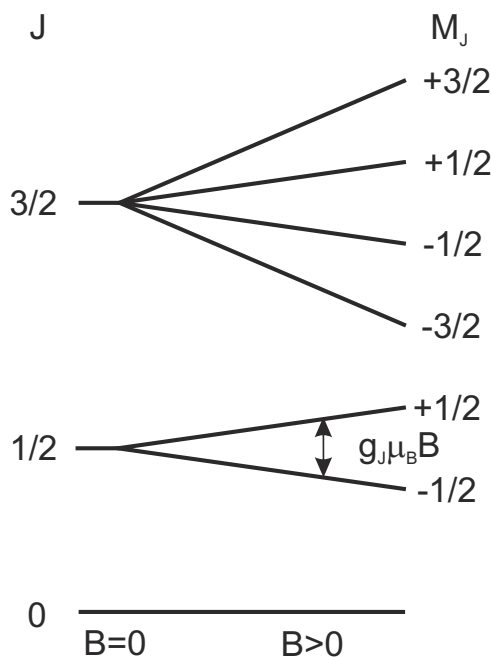
FIGURE 3.1: Splitting of levels with different $\boldsymbol{J}$ by magnetic field.

As opposed to the free atoms, in solids a paramagnetic ion is affected by a strong electrostatic field (so-called 'ligand' or crystal field) produced by the lattice ions. As a consequence, the Hamiltonian in the form of (3.1) may not correctly describe the properties of a paramagnetic ion and the interaction with crystal field has to be taken into account. Usually this interaction is called the fine-structure interaction. It is essentially important for the elements with partly filled p shells (5p, 6p groups of the periodic table) where the energy of this interaction can exceed the energy of the spin-orbit and Zeeman interactions [42].

In the electrostatic potential of the crystal field the electronic levels of ions experience a 'Stark splitting'. Since the crystal field reflects the symmetry of the local position, the splitting of levels can be predicted by the group theory and, in the case of low symmetry, the degeneracy may be completely removed. Kramers formulated an important theorem concerning the residual degeneracy: in the absence of a magnetic field the energy level is at least doubly degenerate for half-integer spin, i.e. odd number of electrons. Such a pair of states ('Kramers doublet') is time conjugate and cannot be split by an electrostatic field, which has time-even operator. A magnetic perturbation in turn is odd under time reversal, thus removes the residual degeneracy of a Kramers doublet.

To keep the simple form (3.1) of Zeeman interaction in complexes, the concept of an 'effective spin' S has been introduced. An effective spin is a fictitious angular momentum and its value is such that the degeneracy of a group of levels of interest is (2S+1), for example, in the case of 3-fold degeneracy $S = 1$. The use of effective spin allows to set up the 'effective spin Hamiltonian' which can correctly describe the behaviour of a group of levels in a similar form as for a free atom or ion.

In most cases, the spin Hamiltonian can be written as a sum of five components [37]:

$$\mathcal{H} = \mathcal{H}_{EZ} + \mathcal{H}_{FS} + \mathcal{H}_{HF} + \mathcal{H}_{NZ} + \mathcal{H}_Q, \tag{3.3}$$

where

- $\mathcal{H}_{EZ} = \mu_B S \cdot \tilde{g} \cdot B$ is an electron Zeeman interaction,

- $\mathcal{H}_{FS} = S \cdot \tilde{D} \cdot S$ — fine structure (FS) interaction,

- $\mathcal{H}_{HF} = I \cdot \tilde{A} \cdot S$ — hyperfine (hf) interaction,

- $\mathcal{H}_{NZ} = g_n \mu_n I \cdot B$ — nuclear Zeeman interaction,

- $\mathscr{H}_Q = \boldsymbol{I} \cdot \tilde{Q} \cdot \boldsymbol{I}$ — nuclear quadrupole interaction,

$\tilde{g}$, $\tilde{D}$, $\tilde{A}$ and $\tilde{Q}$ are tensor quantities, g_n and μ_n — nuclear g factor and Bohr magneton, respectively. The hf and nuclear quadrupole interactions occur due to the interaction of the unpaired electron with nuclear magnetic dipole and electric quadrupole moments of the impurity atom, respectively. Usually, the splitting associated with $\mathscr{H}_{HF}$, $\mathscr{H}_{NZ}$ and $\mathscr{H}_Q$ are considerably smaller than those of electron Zeeman and FS interactions and can be neglected in MCD/MCPL analysis. Thus, only the first two components of Eq. (3.3) will be considered in the following discussions.

The influence of the crystal field is essentially strong for the elements with unpaired p electron(s), e.g. Bi, Pb, Te, Sn, Sb, etc., because p electrons occupy the outer shell and p orbitals are spatially extended in comparison with d orbitals and even more with f orbitals. The energy associated with a FS interaction can introduce the main contribution to the spin Hamiltonian (3.3) and produce the main part of the level splitting. That is why in the next subsection this phenomena will be discussed in more details.

3.2   Fine structure interaction

In the presence of a strong (comparing to the Zeeman interaction) ligand field of axial symmetry, the (2S+1)-fold degenerate states will be split into $(S + 1/2)$ doublets if S is half-integer, or S doublets and one singlet if S is integer. In the first case each doublet can be treated as a Kramers doublet with the effective spin $S = 1/2$. The case of integer S is rather different due to the mixing of wave functions. Moreover, the addition of a rhombic distortion leads to the removal of the residual degeneracy. The Hamiltonian of such a system with a magnetic field $\boldsymbol{B}$ applied at an angle θ to the symmetry axis (z-axis) can be written in the form

as follows [57]:

$$\mathscr{H} = D\left\{S_z^2 - \frac{1}{3}S(S+1)\right\} + E(S_x^2 - S_y^2) + g_\parallel \mu_B B S_z \cos\theta + g_\perp \mu_B B S_x \sin\theta,$$

(3.4)

where $g_\parallel = g_{zz}$ and $g_\perp = g_{xx} = g_{yy}$ are the parallel and perpendicular g-factors, D and E are the axial and rhombic components of the zero-field splitting, respectively.
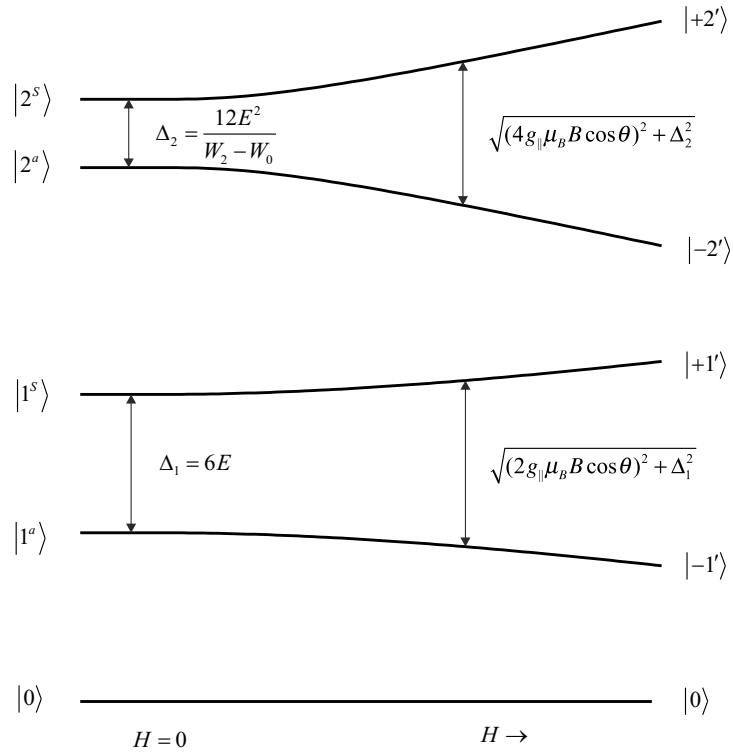
FIGURE 3.2: Energy levels and states in the assumption of the Hamiltonian (3.4).

The useful trick which significantly simplifies the solving and analysis of Eq. (3.4) is to use as the basis (for each spin doublet) a linear combination of the form:

$$\begin{aligned}
|+'\rangle &= \cos\alpha\,|+\rangle + \sin\alpha\,|-\rangle \\
|-'\rangle &= \sin\alpha\,|+\rangle - \cos\alpha\,|-\rangle,
\end{aligned}$$

(3.5)

then one obtains the energy of levels (for $S = 2$ system) in the following form:

$$W_\pm = D' \pm \frac{1}{2}\sqrt{(\tilde{g}_\parallel \mu_B B \cos\theta)^2 + \Delta^2}, \tag{3.6}$$

where $\tan 2\alpha = \Delta/(\tilde{g}_\parallel \mu_B B \cos\theta)$; $\tilde{g}_\parallel = 4g_\parallel$, $D' = 2D$, $\Delta = 12E^2/(W_2 - W_0)$ for the $|\pm 2\rangle$ doublet, and $\tilde{g}_\parallel = 2g_\parallel$, $D' = -D$, $\Delta = 6E$ for the $|\pm 1\rangle$ doublet.

The energy levels and their magnetic field dependence are shown in Fig. 3.2. In the limit of high magnetic fields ($H \gg \Delta$) the wave functions become pure $|\pm\rangle$ and the energy of levels linearly depends on the MF. In the absence of magnetic field the states have symmetric and antisymmetric wave functions $1/\sqrt{2}(|+\rangle \pm |-\rangle)$ (left part of Fig. 3.2).

3.3 Rate equations and spin-lattice relaxation

In all experiments based on the Zeeman effect the measured paramagnetic signal depends on the occupation difference of levels, so a brief discussion of the rate equations is necessary. The rate equations for the simplest two level system with $S = 1/2$ (Fig. 3.3) are:

$$\begin{aligned}
\frac{dN_1}{dt} &= -(W_{12} + R_{12})N_1 + (W_{21} + R_{21})N_2, \\
\frac{dN_2}{dt} &= (W_{12} + R_{12})N_1 - (W_{21} + R_{21})N_2,
\end{aligned} \tag{3.7}$$

where W_{12}, W_{21} are the probabilities of magnetic dipole transitions induced by a microwave field (present in the electron spin resonance (ESR) and related experiments) and R_{12}, R_{21} are relaxation transition probabilities, N_2 and N_1 — populations of $|\pm 1/2\rangle$ states, respectively.

Let us consider the case of absence of microwave induced transitions, i.e. $W_{12} = W_{21} = 0$. In the thermal equilibrium $\frac{dN_i}{dt} = 0$ and taking into account

the Boltzmann distribution, from (3.7) it follows that the population difference is:

$$\Delta N_0 = N_1 - N_2 = N \tanh\left(\frac{\Delta E}{kT}\right), \tag{3.8}$$

where $N = N_1 + N_2$ is a total number of spins. This expression is valid only for the Kramers doublets. In the general case of an effective spin S the population difference is given by the Brillouin function [37, 57]:

$$B_S\left(-\frac{\Delta E}{kT}\right) = B_S(x) = \frac{2S+1}{2S}\coth\left(\frac{2S+1}{2S}x\right) - \frac{1}{2S}\coth\left(\frac{x}{2S}\right) \tag{3.9}$$

Obviously, if $S = 1/2$ Eq. (3.9) transforms to the simple hyperbolic tangent.
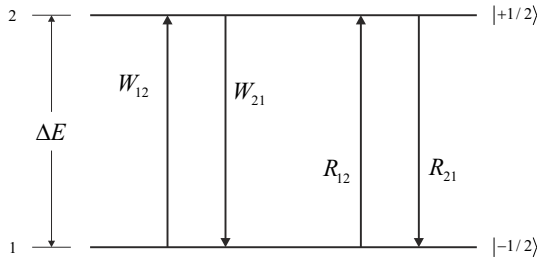
FIGURE 3.3: Kramers doublet with the microwave absorption (W_{12}), emission (W_{21}) and spin-lattice relaxation (R_{12} and R_{21}) transition probabilities.

After some perturbation the spin system will exponentially return to its thermal equilibrium with a characteristic time T_1:

$$\Delta N(t) = A \exp\left(-\frac{t}{T_1}\right) + \Delta N_0 \tag{3.10}$$

$$T_1 = \frac{1}{R_{12} + R_{21}} \tag{3.11}$$

The characteristic time T_1 is usually called longitudinal spin-lattice relaxation time, because it deals with the longitudinal magnetization along the MF direction.

The nature of the spin-lattice relaxation originates from the interaction between spins and phonons. Due to the thermal vibrations, the adjacent magnetic atoms create fluctuating local magnetic field with the oscillating component at the resonance frequency as well. There are three main mechanisms of spin-lattice relaxation [37, 57–59]:

- Direct process. The spin system absorbs a phonon with the energy $\hbar\omega_{12} =$

$E_2 - E_1$ which results in the spin flip (transition $1 \longrightarrow 2$ in Fig. 3.4a). The reverse spin flip ($2 \longrightarrow 1$ transition) leads to the emission of a phonon with the same energy $\hbar\omega_{12}$. The spin-lattice relaxation time changes as $T_1 \sim 1/T$.

- Raman process. A phonon of any energy $\hbar\omega_1$ interacts with the spin and causes a transition (up or down, see Fig. 3.4b). The scattered phonon has the energy $\hbar\omega_2 = \hbar\omega_1 \pm \hbar\omega_{12}$. $T_1 \sim 1/T^n$, where $n = 5, 7, 9$ for a multiplet with a small splitting, non-Kramers and Kramers doublets, respectively.

- Orbach process. A phonon with the resonance frequency excites the spin system to a much higher state. Then the exited spin relaxes to another state under the emission of phonon with the corresponding energy, Fig. 3.4c. $T_1 \sim \exp\dfrac{\hbar\omega_{13}}{kT}$.
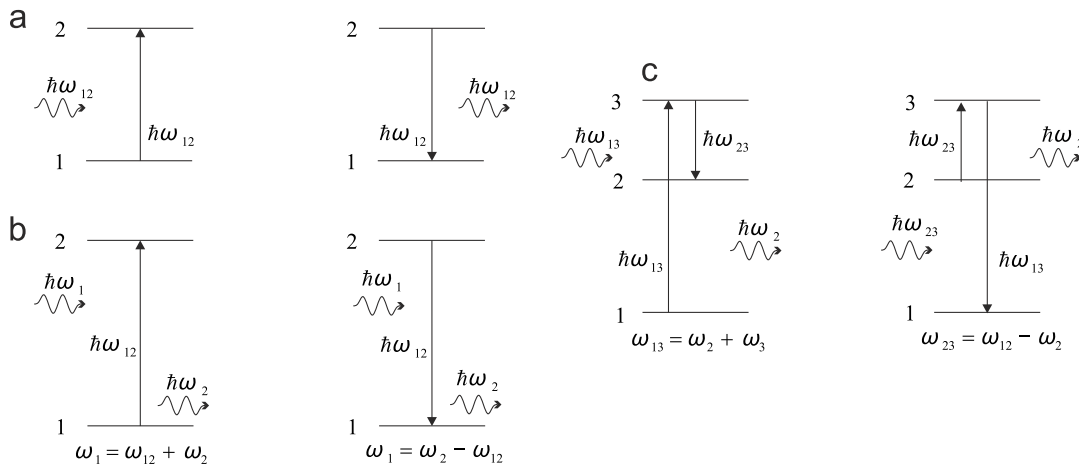
FIGURE 3.4: Spin-lattice relaxation mechanisms: direct process (a), Raman process (b) and Orbach process (c).

Though the Raman process is a second order process, it may have grater influence on the spin-lattice relaxation than the direct process at high temperatures, i.e. $\dfrac{\hbar\omega}{kT} \ll 1$. In this temperature region the density of phonons involved in the Raman process is higher than in the direct. Since all mechanisms have different temperature dependences it is possible to distinguish them by measuring the

temperature dependence of T_1. However, in practice it is a very tough task, because of several reasons. Firstly, T_1 varies rapidly with temperature and in a very wide range and, secondly, usually several processes occur simultaneously. However, at low temperatures ($\frac{\hbar\omega}{kT} \gg 1$) the direct process predominates.

3.4   MCD and MCPL
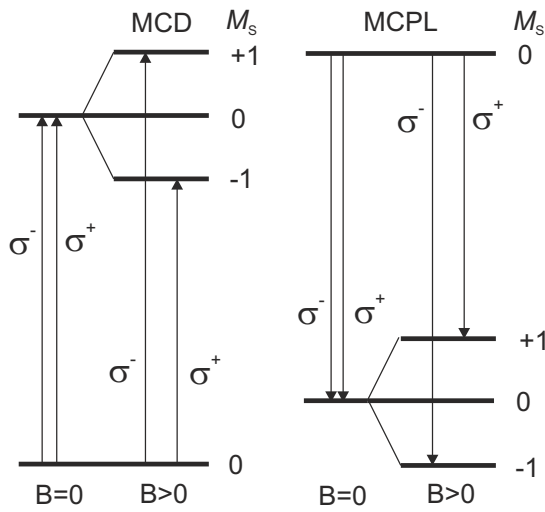
FIGURE 3.5: Examples of systems exhibiting the $\mathscr{A}$ term. On the left: in the MCD. On the right: in the MCPL.

The magnetic circular dichroism and magnetic circular polarization of luminescence are universal well-known techniques for the investigation of the paramagnetic ions and defects. In MCD experiments, the difference in absorption of right (σ^+) and left circular (σ^-) polarized light induced by a magnetic field is measured, e.g. $\Delta A = A^+ - A^-$. The MCPL signal is defined as $\Delta_{MCPL} = \dfrac{I^+ - I^-}{I^+ + I^-} = \dfrac{\Delta I}{I_{tot}}$, where $I^{\pm}$ is the intensity of σ^+ and σ^- components of emitted light. In general, both effects are treated as a sum of three terms, $\mathscr{A}, \mathscr{B}$ and $\mathscr{C}$ [60, 61]:

$$\frac{\Delta A}{E}, \frac{\Delta I}{E} \sim B \left[\mathscr{A} \frac{\partial f(E)}{\partial E} + \left(\mathscr{B} + \frac{\mathscr{C}}{kT} \right) f(E) \right], \tag{3.12}$$

where $f(E)$ is a lineshape function, B is a magnetic field.

The diamagnetic $\mathscr{A}$ term (Fig. 3.5, 3.6) occurs if any (initial or final) state is degenerate. This term is field dependent only and has a derivative-like spectral shape. The magnitude of the $\mathscr{A}$ term for $|A\rangle \longrightarrow |J\rangle$ (MCD) and $|J\rangle \longrightarrow |A\rangle$
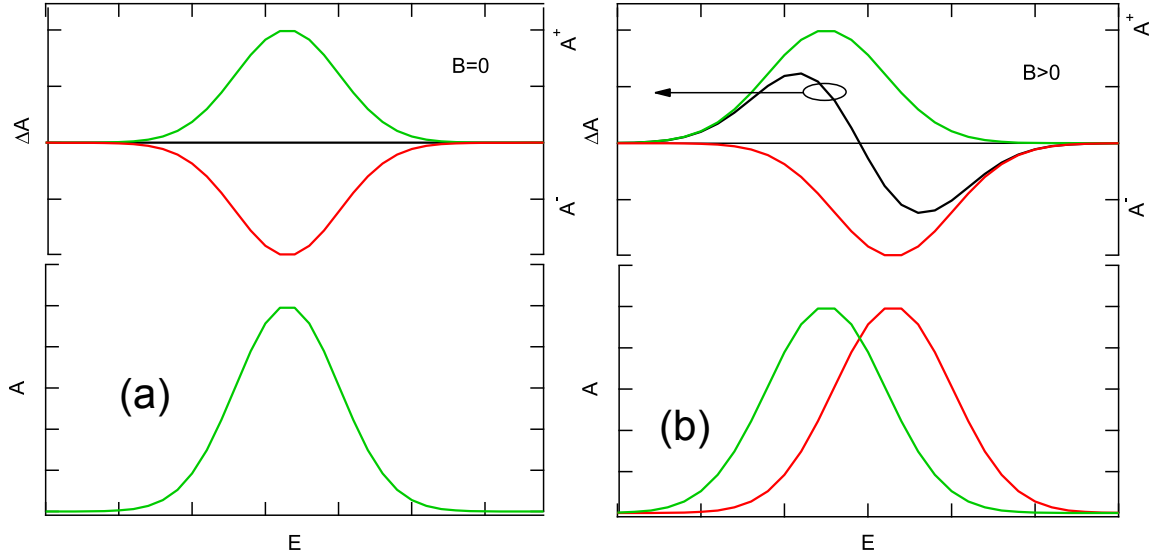
FIGURE 3.6: Origin of the $\mathscr{A}$ term

(MCPL) transitions is [35, 62–65]

$$MCD : \mathscr{A} \approx \sum_{A,J} \left(\langle J | \, \mu_z \, | J \rangle - \langle A | \, \mu_z \, | A \rangle \right) \tag{3.13}$$

$$\times \left(| \, \langle A | \, m_+ \, | J \rangle \, |^2 - | \, \langle A | \, m_- \, | J \rangle \, |^2 \right)$$

$$MCPL : \mathscr{A} \approx \sum_{A,J} \left(\langle J | \, \mu_z \, | J \rangle - \langle A | \, \mu_z \, | A \rangle \right) \tag{3.14}$$

$$\times \left(| \, \langle J | \, m_+ \, | A \rangle \, |^2 - | \, \langle J | \, m_- \, | A \rangle \, |^2 \right),$$

where $m_\pm = \mp 1/\sqrt{2}(m_x \pm i m_y)$ is $\sigma^\pm$ electric dipole moment, μ_z is magnetic dipole moment and the summation is over all components of $|A\rangle$ and $|J\rangle$ states.

The first part of Eq. (3.13) and (3.14) is the difference in the Zeeman splitting of the final and initial states. In the absence of a magnetic field the absorption/emission of σ^+ and σ^- components are equal. Thus no MCD/MCPL signal can be observed as it is shown in Fig. 3.6(a). When a magnetic field is applied the degenerate states split due to the Zeeman effect, $\sigma^\pm$ bands linearly separate and the signal increases with increasing of B.

The population difference of the initial Zeeman sub-levels causes a paramagnetic $\mathscr{C}$ term. This term is field and temperature dependent and it is defined as

follow [35, 62–65]:

$$MCD : \mathscr{C} \approx \sum_{A,J} \langle A | \, \mu_z \, | A \rangle$$

$$\times \left(| \, \langle A | \, m_+ \, | J \rangle \, |^2 - | \, \langle A | \, m_- \, | J \rangle \, |^2 \right) \tag{3.15}$$

$$MCPL : \mathscr{C} \approx \sum_{A,J} \langle J | \, \mu_z \, | J \rangle$$

$$\times \left(| \, \langle J | \, m_+ \, | A \rangle \, |^2 - | \, \langle J | \, m_- \, | A \rangle \, |^2 \right), \tag{3.16}$$

where the notations are the same as in (3.13) and (3.14). Here the first part has only the initial state Zeeman term. The example of a system with the paramagnetic term is shown in Fig. 3.7(a). At low temperatures ($\Delta E >> kT$) the lowest Zeeman sub-level has much greater population and the $|-1\rangle \longrightarrow |0\rangle$ transition is the most intense. It results in the $f(E)$ bandshape (Fig. 3.7(b)) of the MCD and MCPL signal. With the increasing of temperature $\mathscr{C}$ term decreases and when the population of magnetic sub-levels becomes equal, only $\mathscr{A}$ term contributes to the ΔA and ΔI producing the same spectral band as in Fig. 3.6(b).
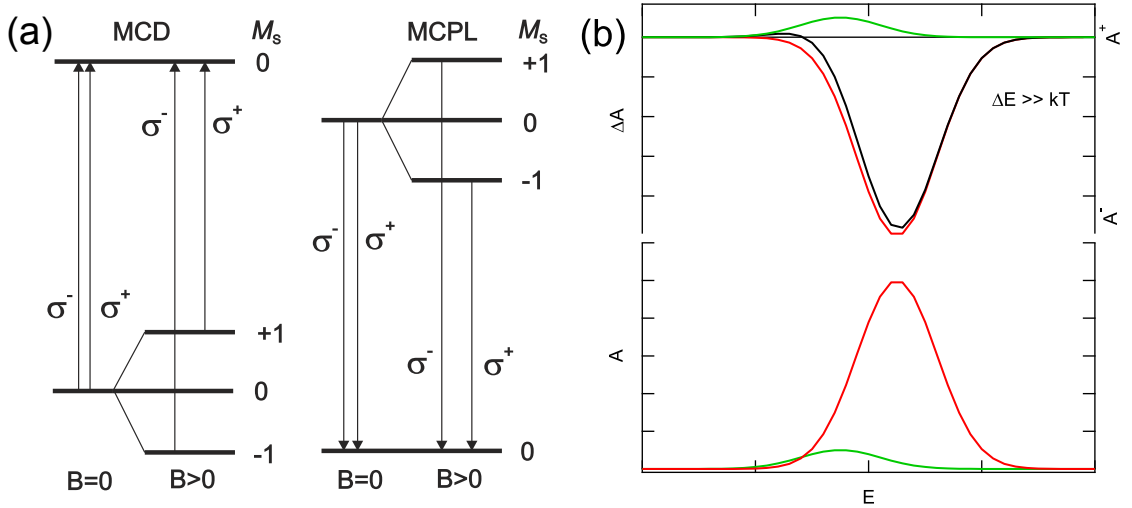
FIGURE 3.7: (a) Examples of system exhibiting the $\mathscr{C}$ term; (b) its origin.

The $\mathscr{B}$ term is a result of the field-induced mixing of $|A\rangle$ and $|J\rangle$ with the intermediate state $|K\rangle$ [35, 62–65]:

$$
\begin{aligned}
MCD : \mathscr{B} \approx Re \sum_{A,J} \Bigg[&\sum_{K \neq J} \frac{-\langle J | \, \mu_z \, | K \rangle}{\Delta E_{KJ}} (\langle A | \, m_+ \, | J \rangle \langle K | \, m_+ \, | A \rangle \\
&- \langle A | \, m_- \, | J \rangle \langle K | \, m_- \, | A \rangle) \\
&+ \sum_{K \neq A} \frac{-\langle K | \, \mu_z \, | A \rangle}{\Delta E_{KA}} (\langle A | \, m_+ \, | J \rangle \langle J | \, m_+ \, | K \rangle \\
&- \langle A | \, m_- \, | J \rangle \langle J | \, m_- \, | K \rangle) \Bigg]
\end{aligned}
\tag{3.17}
$$

The expression for the MCPL case is similar but $|A\rangle$ and $|J\rangle$ are swapped in the bra-kets, e.g. $\langle A | \, m_\pm \, | J \rangle \longrightarrow \langle J | \, m_\pm \, | A \rangle$. Both ground and excited states can be affected, but usually $\mathscr{B}$ term is larger for the excited states due to the small energy difference between mixing states. This term is field dependent but in contrast to $\mathscr{A}$ term it has $f(E)$ bandshape.

The relative magnitudes of $\mathscr{A}$, $\mathscr{B}$ and $\mathscr{C}$ terms depend on the absorption/emission bandwidth Δ, energy distance ΔE to the closest field-induced mixing state and temperature [60]: $\mathscr{A} : \mathscr{B} : \mathscr{C} = 1/\Delta : 1/\Delta E : 1/kT$. In the typical case of broad bands at room temperature $\Delta = 10^3$ cm^{-1}, $\Delta E = 10^4$ cm^{-1} and $kT = 200$ cm^{-1} we get $\mathscr{A} : \mathscr{B} : \mathscr{C} = 10^{-3} : 10^{-4} : 5 \times 10^{-3}$. If the measurements are taken at 15 K the relative magnitudes are $10^{-3} : 10^{-4} : 0.1$. It is clear that at low temperatures the $\mathscr{C}$ term provides the main contribution to ΔA and ΔI.

In disordered systems, such as investigated glasses in this Thesis, the orientational averaging of ΔA and ΔI must be performed [66]:

$$
\langle \Delta \varepsilon \rangle = \frac{1}{8\pi^2} \int_{\phi=0}^{\pi} \int_{\psi=0}^{2\pi} \int_{\theta=0}^{\pi} \Delta \epsilon \sin \theta \, d\theta \, d\phi \, d\psi,
\tag{3.18}
$$

where $\Delta \varepsilon$ is ΔA or ΔI regarding which experiment we deal with, ϕ, ψ, θ are the

Eulerian angles that give the relationship between the molecule-fixed and space-fixed sets of axes with θ being the angle between z axes of these sets. Usually the space-fixed z axis is defined by the direction of the external magnetic field $\boldsymbol{B}$, thus θ is the same angle as in Eq. (3.4)

The major information about the ground and excited states can be obtained by measuring the temperature and field dependences of MCD and MCPL signals at fixed wavelength. Usually these saturation magnetization data are presented in two formats (Fig. 3.8, 3.10). For a magnetic field dependence the intensity of MCD or MCPL signal is plotted versus $\mu_B B/2kT$ and each curve (isotherm) represents one temperature. The temperature dependence is plotted as a function of $1/T$ and each curve has fixed magnitude of the magnetic field. These saturation curves are measured at the peak of the transition band, where the $\mathscr{A} = 0$. This approach significantly simplifies the analysis of the experimental data.
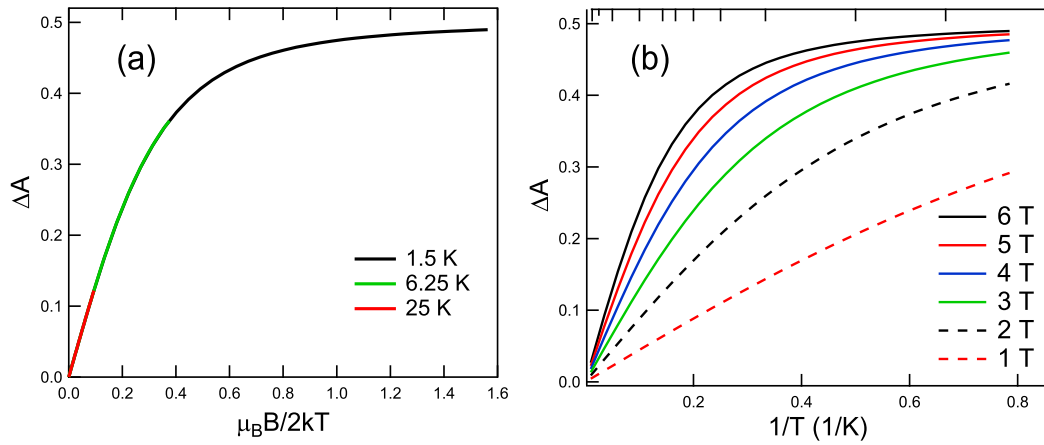
FIGURE 3.8: MCD saturation curves for an isolated effective Kramers doublet with $g_\parallel = 2$. (a) – MF dependences; (b) – temperature dependences

Let us consider the simple case when only the initial state is degenerate and $S = 1/2$, i.e. Kramers doublet. The MCD $\mathscr{C}$ term and its orientation averaging lead to [33]

$$\Delta A = A_{sat} \int_0^1 \cos\theta \tanh\left(\frac{g_\parallel \mu_B B \cos\theta}{2kT}\right) d\cos\theta, \qquad (3.19)$$

where A_{sat} is the maximum value of ΔA at the saturation (hereinafter we omit the $\langle \rangle$ notations) and it scales the curves only. In the case of MCPL the effect of photoselection must be taken into account [60, 66]. The resulting expression is a counterpart of Eq. (3.19) but with an additional factor $\cos^2 \theta$ in the integrand. This effect has only a small quantitative influence on the saturation curves, so all further discussions are valid for both the MCD and MCPL experiments. All curves of the $\mu_B B / 2kT$ plot superimpose, as it is shown in Fig. 3.8(a). The increase of $g_\parallel$ will cause the saturation of isotherms at lower MF. The decrease of temperature results in the increasing of $\Delta \varepsilon$, at low temperatures and high fields it saturates and the curves superimpose.
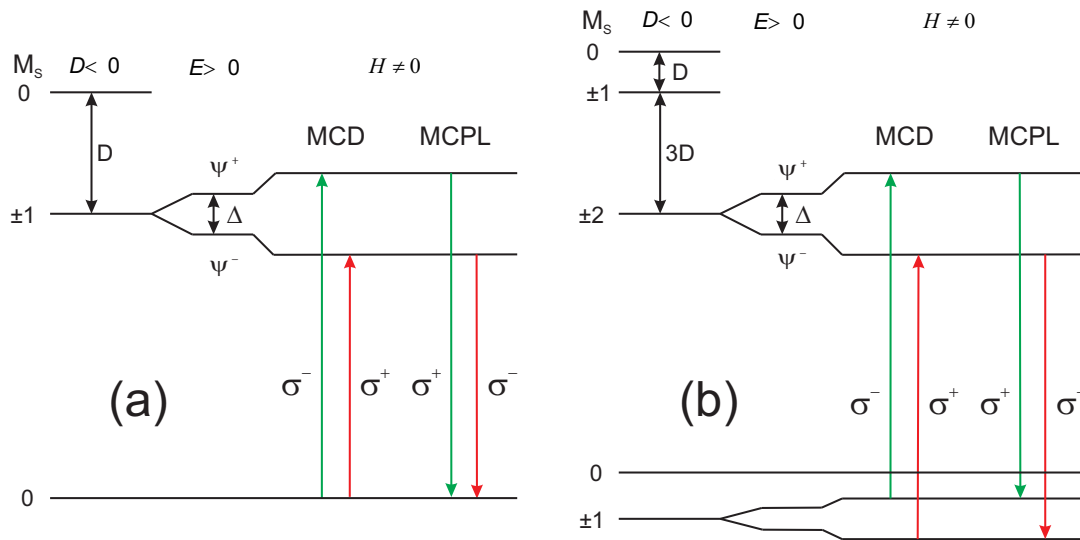
FIGURE 3.9: Energy level diagrams of the systems with $D < 0$. (a) - spin-singlet GS and isolated non-Kramers doublet from $S = 1$ ES. (b) - both GS and ES are spin-multiplets.

The more general case is a system described by the spin Hamiltonian (3.4). Let's assume that the initial state has $S = 1$, then the negative axial component of the zero-field splitting $D < 0$ brings the $M_S = \pm 1$ doublet to the lowest position and the rhombic component $2E = \Delta$ removes the residual degeneracy as it is shown in Fig. 3.9. This non-Kramers doublet produces a $\mathscr{C}$ term and it is isolated if $|D| \gg \Delta$. In the absence of a magnetic field the wave functions of the doublet

are $1/\sqrt{2}(|+1\rangle \pm |-1\rangle)$. However $\Delta\varepsilon$ is non-zero only in the presence of a magnetic field, because both MCD and MCPL require complex wave functions. If $g_\parallel \gg g_\perp$
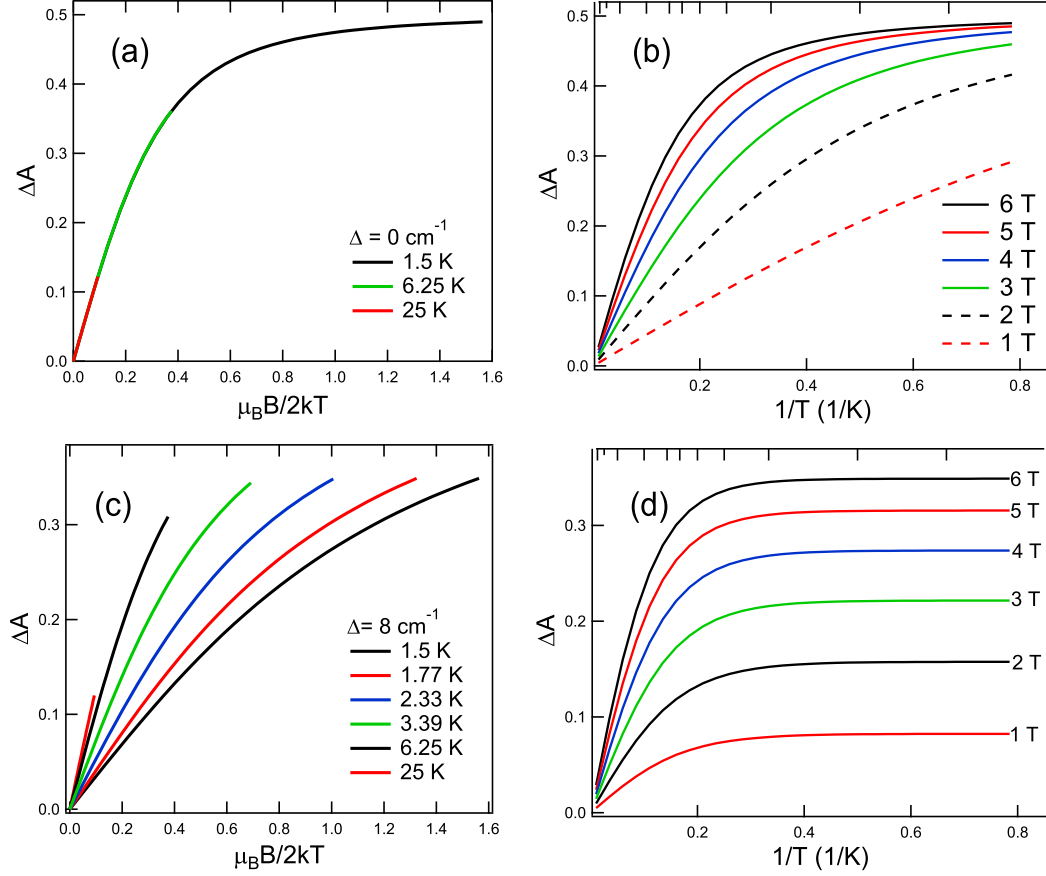
FIGURE 3.10: The effect of rhombicity on the saturation curves for an isolated non-Kramers doublet with $g_\parallel = 2$. (a,c) – MF dependences; (b,d) – temperature dependences

the $\mathscr{C}$ term related MCD intensity is [33]

$$\Delta A = A_{sat} \int_0^1 \frac{2g_\parallel \mu_B B \cos^2\theta}{\sqrt{\Delta^2 + (2g_\parallel \mu_B B \cos\theta)^2}} \tanh\left(\frac{\sqrt{\Delta^2 + (2g_\parallel \mu_B B \cos\theta)^2}}{2kT}\right) d(\cos\theta)$$

(3.20)

Again, to obtain the expression for MCPL, the factor $\cos^2\theta$ must be added. The example of the saturation curves calculated using the Eq. (3.20) is given in Fig. 3.10. The upper part has no rhombic component of ZFS and, obviously, it coincides with the case of an effective Kramers doublet. The lower part shows the

influence of the rhombicity with $\Delta = 8$ cm^{-1}. The isotherms of the field dependences exhibit well pronounced nesting behaviour and its degree is proportional to the magnitude of Δ. In the $1/T$ representation the curves exhibit saturation even at low magnetic fields and the saturation values are different for each MF. The magnitude of the zero-field splitting defines the values of the temperature and magnetic field at which the saturation appears: the higher Δ, the lower MF and higher temperature. Also it is seen that the presence of rhombic ZFS component reduces the maximum value of ΔA. The $\mathscr{C}$ term for a non-Kramers doublet arises from the unequal mixing between $|+1\rangle$ and $|-1\rangle$ states and the Boltzmann contribution among them. It is a mixing between the sub-levels of a doublet that causes the latter effect.

The influence of the non-zero $g_\perp$ and $\mathscr{B}$ term also can be taken into account [33]. For example, to include the linear $\mathscr{B}$ term into consideration the adding of simple $b_0 B$ term to Eq. (3.19) or Eq. (3.20) is sufficient. Here b_0 indicates the magnitude of the initial state linear $\mathscr{B}$ term. Eventually it causes the fan out behaviour of saturation curves plotted as a function of $\mu_B B/2kT$. As a consequence, for an effective Kramers doublet interacting with another energy level the isotherms also do not superimpose.

MCPL technique can be utilized to study some aspects of the spin dynamics in excited states. The idea consists in the measurement of the temporal dependence of PL polarization degree $\Delta_{MCPL} = \Delta I/I_{tot}$ as it is shown in Fig. 3.11. A pulsed excitation creates the non-equilibrium population distribution among the spin sublevels of ES, thus the degree of the emission polarization is also deviated from its thermal equilibrium value. The spin relaxation forces the system to reach the Boltzmann distribution and if the spin relaxation time T_1 is less than the radiative decay time, the PL polarization degree will reach its equilibrium value.
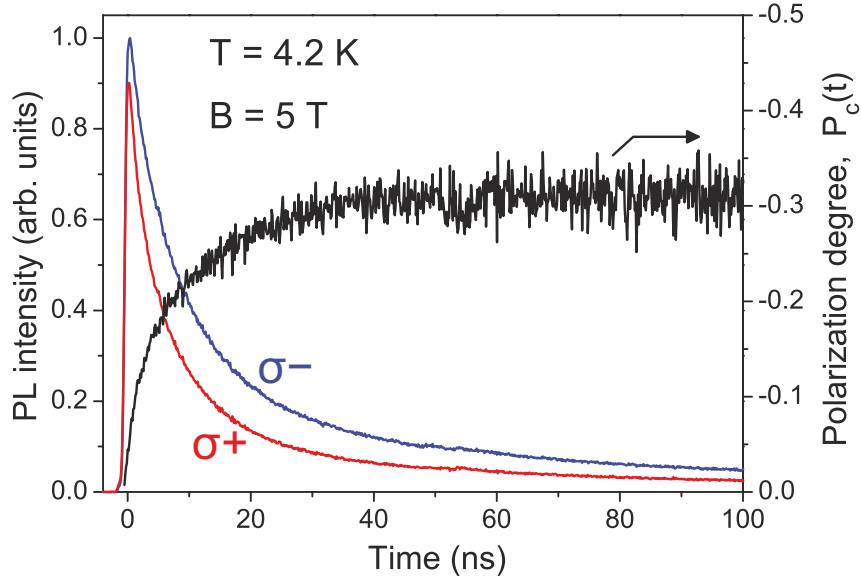
FIGURE 3.11: Time-resolved MCPL spectroscopy in CdSe/CdS core/thick-shell nanocrystals (After [36])

The polarization dynamics can be described by a simple expression

$$\Delta_{MCPL}(t) = \Delta_{MCPL}^0 \left[1 - \exp\left(-\frac{t}{T_1} \right) \right],$$
(3.21)

where Δ_{MCPL}^0 is an equilibrium value of the polarization degree. The spin relaxation depends on the temperature and magnetic field as it was discussed in Sec. 3.3. Thus the time-resolved MCPL spectroscopy allows one to study the spin relaxation mechanism by measuring the MF and temperature dependence of T_1.

3.5 Optically detected magnetic resonance

The optically detected magnetic resonance is a double resonance experiment. In ODMR experiment we measure the changes of MCD or MCPL signal under microwave radiation at the resonant frequency:

$$\Delta\rho = \Delta\varepsilon - \Delta\varepsilon^0,$$
(3.22)

where $\Delta\varepsilon$ is MCD/MCPL signal under applied microwave pumping and $\Delta\varepsilon^0$ — in the absence of MW radiation. If the frequency of MW radiation does not match the energy interval between spin sublevels, the ODMR signal $\Delta\rho = 0$. The microwave pumping at the resonance frequency tends to equalize the population of the spin sublevels, and, as a consequence, decreases the MCD/MCPL signal.

Usually ODMR experiment can be performed in two regimes. The first one consists in recording of the field dependence of $\Delta\rho$ in the particular MCD/MCPL band. This regime allows to define the magnetic properties of a particular optical centre. In the second regime the spectrum is recorded at a constant magnetic field (Fig. 3.12). This experiment allows to distinguish the optical transitions from different centres.
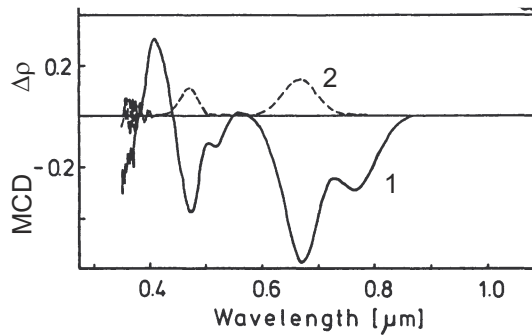
FIGURE 3.12: MCD (curve 1) and ODMR in absorption (curve 2) in $SrF_2 : Pb^{2+}$ ($T = 10K, B = 1.25T, f = 24GHz$) (Adapted from [67])

The spin-lattice relaxation time T_1 can be directly measured in the ODMR experiment in ground and excited states as well. First, the system has to be driven out of thermal equilibrium. It can be done by the fast change of the temperature or magnetic field, or by applying a microwave pulse of the resonance frequency. Then one observes the recovery of the $\Delta\varepsilon$ to the equilibrium value. The most convenient way to disturb the system is a saturating MW pulse. Modern sources of the microwave radiation can produce pulses with the duration of several nanoseconds. Therefore the operating frequency of the photoelastic modulator limits the shortest measurable T_1 by tens of microseconds. However, measurements of the excited states require certain precautions. The spin-lattice relaxation time should be less than the lifetime of this ES. Otherwise

the ODMR signal recovery (after the applied microwave pulse) is due to the optical re-population of this excited state.

One important feature of the ODMR technique is its very high sensitivity. The enhancement of the sensitivity comparing to the conventional ESR method is approximately the ratio of optical and microwave frequencies, e.g. $10^{15}/10^{10} = 10^5$, so the sensitivity of 10^5 spins per mT linewidth can be achieved.

The ESR technique can be used for the investigations of magnetic properties of excited electronic states. In such experiments a sufficient population of ES is achieved by the continuous optical excitation, usually by a laser source. However, successful implementation of this method was obtained only for the long-lived excited states. If the decay time $\tau_r \leq 1$ ms the steady state population may be too low for the ESR detection. Much higher sensitivity of the ODMR removes this limitation and allows one to perform investigations of the short-lived excited states.

3.6 Conclusions

Ions with p electronic outer shells (such as Bi, Pb, Sn, etc) are essentially affected by the (fine) crystal field interaction, which may produce the main contribution to the splitting of energy levels. In this thesis glasses with extremely broad optical transitions were investigated. For this reason only Zeeman and FS interactions were taken into account in the analysis of the experimental data. In general, MCD and MCPL effects are considered as a sum of three parts: diamagnetic $\mathscr{A}$, $\mathscr{B}$ and paramagnetic $\mathscr{C}$ terms. In the case of the broad transition bands only paramagnetic term can be taken into account. The investigation of MCD and MCPL saturation curves gives quantitative information about zero-field splitting energy and Landé g-factor of the ground and excited states, respectively. The ODMR method combines MCD/MCPL and magnetic resonance techniques, that leads

to the high precision determination of parameters of the investigated system and high spectrometer sensitivity. Also, ODMR experiments allow to establish the direct correspondence of optical transitions to the particular defect centre. The use of a microwave resonator, even a tunable one, results in very narrow frequency range. As a consequence to cover the entire GHz range it is necessary to have a set of microwave systems. It is not always possible due to the limited inner space of a helium cryostat.

Chapter 4

MCD/MCPL spectrometer

This chapter describes the MCD/MCPL spectrometer and some aspects of data acquisition. Usually, MCD/MCPL experiments are performed in two main regimes: *a)* spectral measurements at fixed magnetic field and temperature, and *b)* field and temperature dependences at a fixed wavelength. In the latter case, the most useful forms of the MCD/MCPL signal representation are the plots in coordinate $(\Delta A,\ \mu_B B/2kT)$ for the field dependence and $(\Delta A,\ 1/T)$ for the temperature dependence.

MCD and MCPL are measured in the Faraday geometry, i.e. the direction of light propagation is collinear to the external magnetic field $\boldsymbol{B}$. In general, Si- and Ge-based photoreceivers, coupled to a lock-in amplifier, are used for signal detection. However, in the case of MCPL, the use of photon counting technique very often is more preferable, because a much higher signal-to-noise ratio can be achieved.

4.1 MCD spectrometer

Fig. 4.1 schematically shows the experimental setup for MDC measurements. Light from the quartz tungsten or UV enhanced Xenon lamp is dispersed by a monochromator with a spectral resolution 2.5 and 5 nm in the range 350–900

and 900–1600 nm, respectively. After the collimating lens and exchangeable filter (LWPF) the light is linearly polarized with a large aperture Glan-Thompson polarizer. The photoelastic modulator (II/FS20 optical head, Hinds Instruments) acts as a dynamic wave plate oriented at 45° to the polarization plane of the incident light beam. In order to transform the linear polarization of the light to $\sigma^{\pm}$, PEM periodically creates retardation $\delta = \delta_0 Sin(2\pi f_{PEM}t)$, where $\delta_0 = \lambda/4$ is the peak retardation, $f_{PEM} = 20$ KHz is the modulator frequency. Then the light beam is chopped at $f_{CH} \sim$300 Hz, passes through the sample and detected by a photoreceiver.
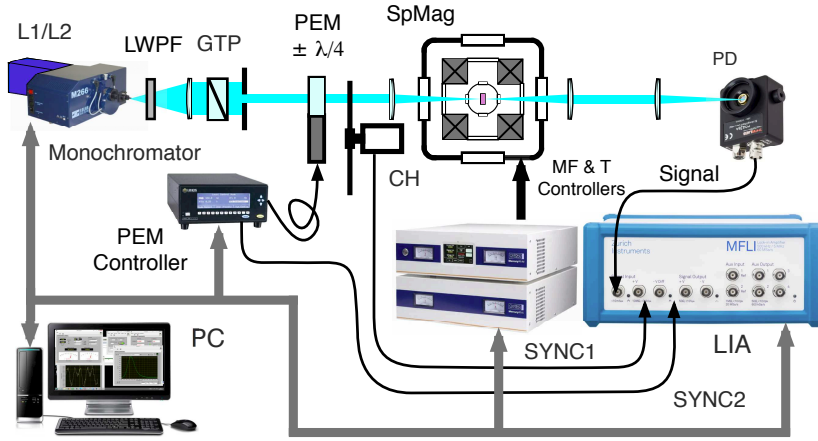
FIGURE 4.1: Setup for MCD measurements. L1/L2 - UV Xenon or quartz tungsten lamp, LWPF - long wave pass filter; GTP - Glan-Thompson polarizer; PEM - photoelastic modulator; CH - chopper; SpMag - cryomagnetic system; PD - Si or Ge amplified photo-detector; LIA - multi-frequency lock-in amplifier.

Without the chopper the signal consists of two components $V_{det} = V_{AC} + V_{DC}$. A dc component V_{DC} is proportional to the intensity of the light passed through the sample. A small ac component V_{AC} is caused by a difference in absorbance of $\sigma^{\pm}$ light, i.e. it is proportional to the MCD. In the case of small dichroism $\Delta A < 0.1$ the ratio of these components can be approximated by [35]:

$$V_{AC}/V_{DC} \approx 1.1515 \Delta A \delta_0 Sin(\omega_{PEM}t) \qquad (4.1)$$

and

$$\Delta A = V_{AC} / \left[1.1515 V_{DC} \delta_0 Sin(\omega_{PEM} t) \right] \tag{4.2}$$

It is seen that MCD signal ΔA is proportional to $V_{AC}/Sin(\omega_{PEM}t)$. The phase-sensitive technique with lock-in amplifier (LIA) is used to detect this small signal at the modulator frequency. The use of the chopper and the second demodulator of LIA locked to the chopper frequency allows the direct measurement of the V_{DC}.

4.2 MCPL spectrometer
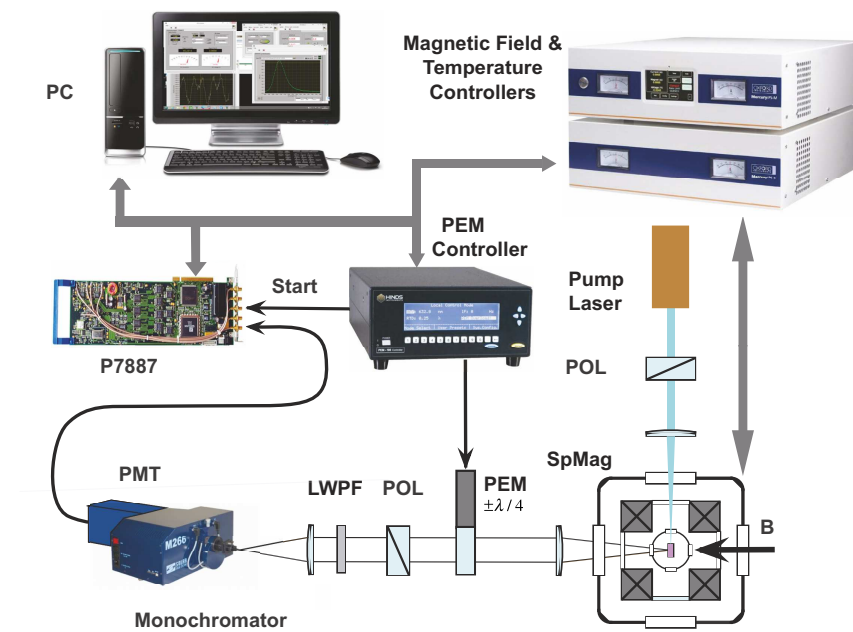
FIGURE 4.2: Setup for MCPL measurements. LWPF - long wave pass filter; POL - polarizer; PEM - photoelastic modulator; SpMag - cryomagnetic system; PMT - photomultiplier tube; P7887 - photon-counting cart.

The scheme of the MCPL spectrometer is shown in Fig. 4.2. The laser beam from a pump source is polarized by the polarizer (POL) and focused on the sample. The collimated beam of PL emission, propagating parallel to the magnetic

field B, passes through the PEM, linear polarizer and exchangeable longpass filter. Then it is dispersed by means of monochromator and detected by a photomultiplier (PMT). We used two different PMTs for NIR 900–1700 nm (InP/InGaAs, R5509-73, Hamamatsu Inc.) and visible 350–900 nm (GaAs, R943-02, Hamamatsu Inc.). The photon-counting technique is implemented to record the signal, because of its superior signal-to-noise ratio. As a pump source we used:

- Laser diode or frequency doubled tunable Ti:Sapphire (Coherent Inc.) in the spectral region 350–460 nm;

- CW laser Verdi, Coherent Inc., 532 nm;

- Tunable Ti:Sapphire laser (Coherent Inc.) in the spectral region 700–1010 nm
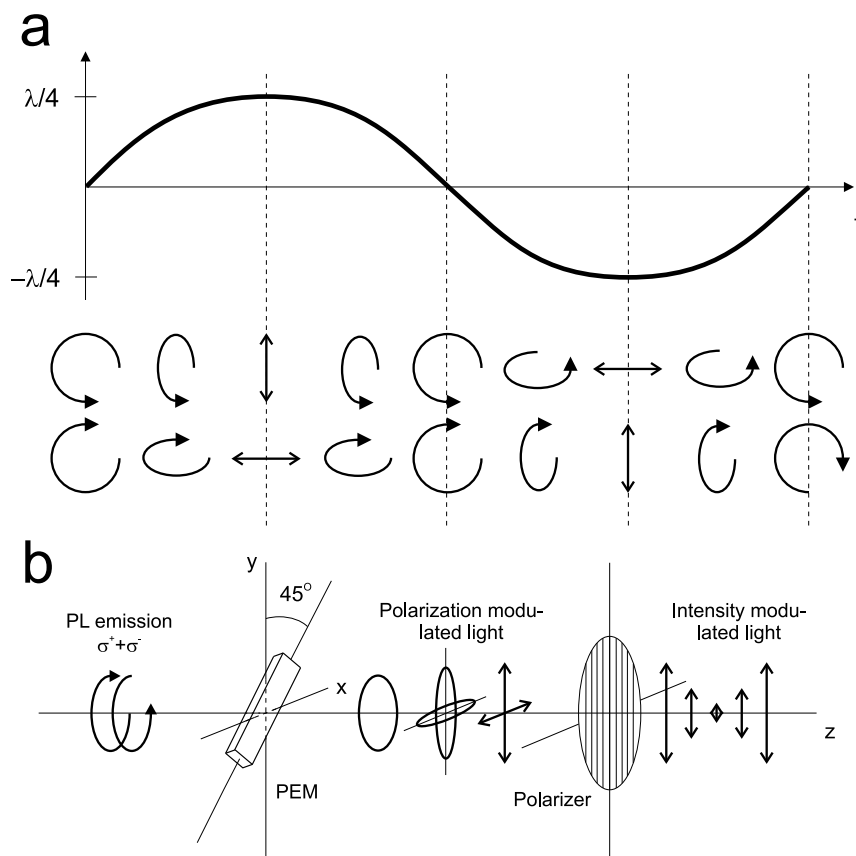
FIGURE 4.3: Transformation of rcp and lcp light by a photoelastic modulator (a) and methodology of MCPL signal measuring (b).

As it was discussed in Chapter 2, in the case of the spin degeneracy of excited and/or ground states, the emitted light consists of two circularly polarized components — σ^+ and σ^-. Photoelastic modulator periodically transforms each of them to linearly polarized light with orthogonal, vertical and horizontal, planes of polarization, as it is shown in Fig 4.3(a). At the peak retardation $\delta = \lambda/4$ *rcp* and *lcp* are transformed to the vertical and horizontal linearly polarized light, respectively, and vice versa when $\delta = -\lambda/4$. In other words, after PEM the PL emission consists of two polarization modulated components, that are analysed by the linear polarizer (Thorlabs LPVIS100 or LPNIR100 for visible and NIR, respectively) with vertically oriented transmission axis, Fig. 4.3(b). The horizontally polarized light is rejected by this polarizer. It is clear, that when the retardation is $\pm\lambda/4$, one measures the intensity I^+ or I^- of $\sigma^\pm$ components, respectively.

An example of the MCPL signal measured with the use of the photon-counting technique is shown in Fig. 4.4. In this particular case, the signal has a sinusoidal form with a low intensity in the first half-cycle. It follows that, the σ^+ component is less intense than σ^-, $\Delta I = I^+ - I^-$ is negative. The amplitude of this sinusoid is $\Delta I/2$ and the baseline defines the total intensity of photoluminescence $I_{tot}/2$. When the magnetic field is set to zero, the MCPL is absent and $\Delta I = 0$, as it is seen in Fig. 4.4.

The essential part of the MCD/MCPL spectrometer is a superconducting magnet and temperature stabilization system. In our experiments we use the helium closed-cycle magneto-optical cryostat SpectromagPT (Oxford Instruments). The sample is placed between the superconducting coils, which are able to produce magnetic field up to 7 T with the homogeneity of 0.01% over 10 mm diameter spherical volume. The temperature of the sample can be controlled in 1.4–300 K range with a thermal stability 0.01 K, except the range 4.2–10 K, where it is not better than 0.05 K.
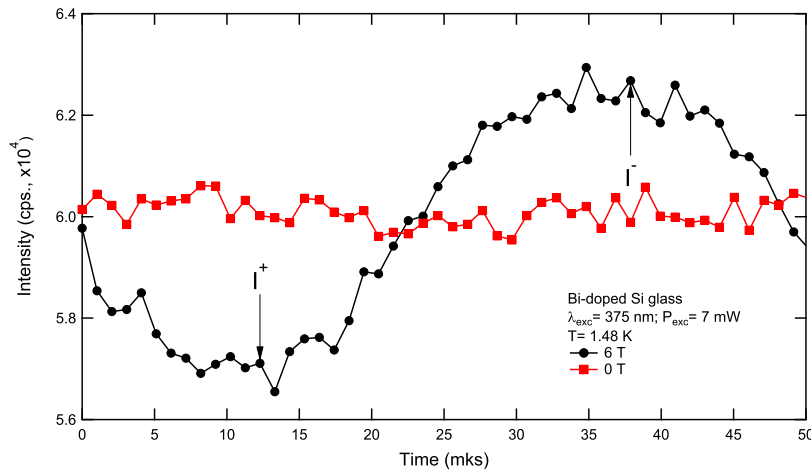
FIGURE 4.4: An example of the MCPL signal in the magnetic field of 6 T
(black circles) and 0 T (red squares).

All instruments are controlled by a personal computer, which is also used for data collection, visualisation and further processing.

4.3   Conclusions

With the present spectrometer we are able to perform MCD/MCPL measurements, that cover UV to NIR spectral range, namely 350–1600 nm, in magnetic fields up to 7 T and in the temperature range 1.4–300 K. In general, it is possible to use the phase-sensitive technique with a lock-in amplifier to detect the MCPL, though it has significantly lower signal-to-noise ratio than the photon-counting technique. The shorter acquisition time can be one of the reasons in favour of phase-sensitive detection. This approach is essentially useful for measurements of the magnetic field dependences, so that the MF can be continuously swept during the experiment. In practice, the choice of the detection technique should be made depending on the experimental conditions and signal magnitude. In all our samples the intensity of the NIR PL can be characterized as too weak to observe the variations at the $10^{-5} - 10^{-6}$ from base level. For this reason the photon-counting technique was implemented to study the MCPL.

Chapter 5

Bismuth doped Mg-Al-Si oxide glass

In this chapter we will present the results obtained from MCD and MCPL experiments performed on a Bi-doped aluminosilicate glass. A series of the samples was provided by Prof. B. I. Denker from A. M. Prokhorov General Physics Institute of Russian Academy of Science. The samples were fabricated by the traditional crucible melting technology (see details in [52]) and they have the following composition: 22.2 mol. % MgO + 22.2% Al_2O_3 + 55.6% SiO_2 + X% Bi_2O_3 (X raging from 0.031% to 0.5%). The samples with the dimensions of $3 \times 4 \times 5$ mm^3 were cut from the synthesized glasses. Compared to the pure silica glass, this composition has substantially lowered melting temperature $\approx$1500 °C and exhibits the spectral properties close to that of MCVD produced Bi-doped aluminosilicate fibers. In our experiments we investigated only one sample with the highest concentration of Bismuth, because the magnitude of the MCD and MCPL signals are proportional to the total number of the absorbing species. The investigation of the influence of the Bi doping level on the MCD and MCPL is an interesting and independent problem. The rather high concentration of Bi in the synthesized glass results in the sufficiently intense PL, MCD and MCPL signal.

5.1 Absorption, excitation, photoluminescence and MCD/MCPL spectra

The absorption spectrum of Bi-doped Al-Mg-Si glass in spectral range 350–1600 nm, shown in Fig. 5.1(a), reveals only two bands labelled D2 and B1 with corresponding peaks at 500 and 700 nm[1].
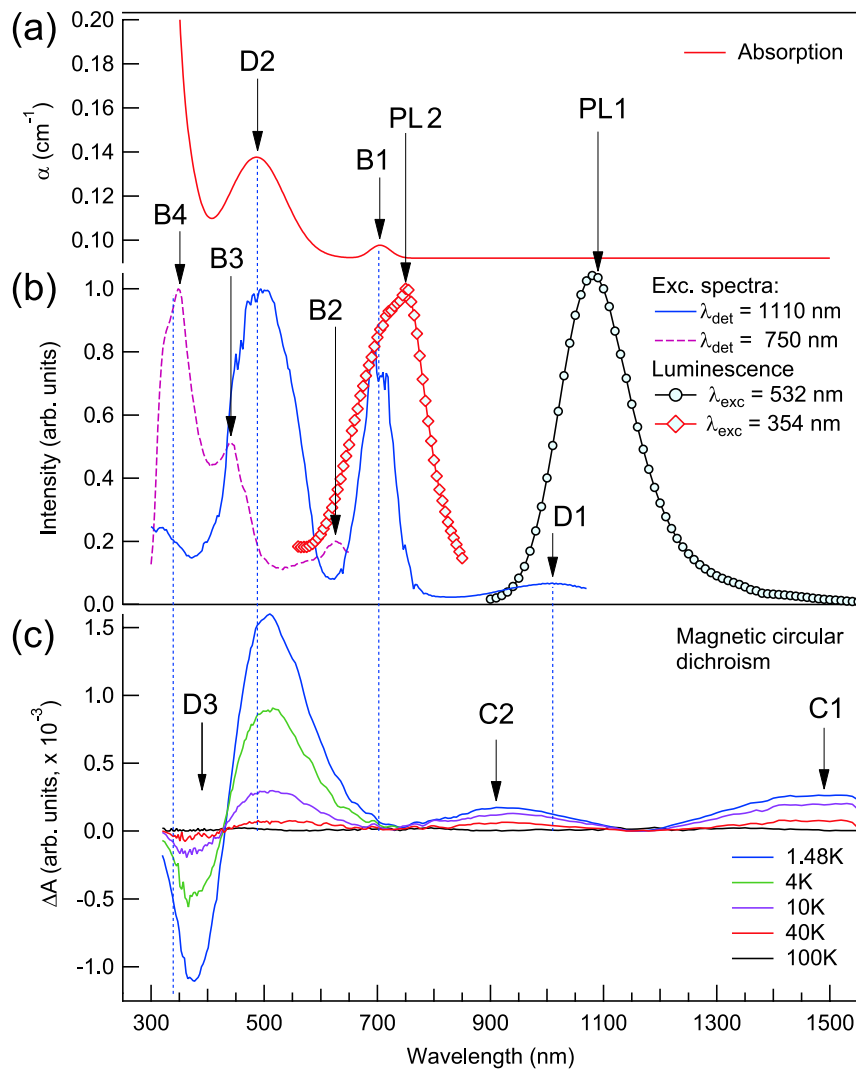
FIGURE 5.1: (a) Absorption spectrum; (b) normalized excitation and PL spectra measured at 300 K; (c) MCD spectra measured at different temperatures in the magnetic field of 6 T.

Excitation spectra of NIR PL1 and visible PL2 bands, shown in Fig. 5.1(b), were measured at 1110 and 750 nm, respectively. There are four bands in the

---

[1]Data on the absorption and excitation bands are collected in Appendix A

excitation spectrum of the NIR PL1 band with maximums at 1030, 700, 500 and near 310 nm (Fig. 5.1(b)). Excitation band D1 corresponds to the first excited state of the PL centre. The emission from this ES appears as a NIR PL1 band with the Stokes shift of ≈ 700 cm^{-1}. The bands at 700 and 500 nm can be put in the direct correspondence to the absorption bands B1 and D2, respectively. Because both bands appear in the excitation spectrum of NIR PL1 band one may suppose that B1 and D2 bands belong to the same optical centre. However, the excitation spectrum of the visible PL2 band at 750 nm reveals three bands at 625, 441 and 340 nm, which do not coincide with any band in the excitation spectrum of NIR PL1 band. This contradiction can be explained by the presence of two different centres with the energy transfer between them. Previously reported in [29], the presence of such an energy transfer has been shown experimentally in Ga/Bi co-doped silica glass, which is a counterpart of the aluminosilicate glass studied in this thesis. This energy transfer occurs due to the strong quadrupole-quadrupole interaction of the B1 band related state with another centre.

5.1.1 MCD spectra

Contrarily to the absorption, the MCD spectrum (Fig. 5.1(c)) reveals four bands: one negative with the peak at 375 nm (D3) and three positive peaked at 505 (D2), 940 (C2) and 1500 nm (C1). All these bands are temperature dependent. The latter, as it was discussed in Chapter 3, indicates the spin multiplicity of the corresponding ground state(s). The presence of only one common band (with the peak near 500 nm) in the MCD and absorption spectra is another strong argument supporting that the B1 and D2 bands belong to different centres. Obviously, the D2 band is due to the transition from the degenerate ground state. The absence of any MCD signal near 700 nm certainly reveals that the B1 band originates from the centre with a non-degenerate GS. The D2 band cannot be

assigned to the $^3P_0 \longrightarrow \, ^1D_2$ or $^3P_0 \longrightarrow \, ^1S_0$ transitions of Bi^+ ion as it has been proposed by many authors, for example in [18, 68]. On the other hand the band B1 can be attributed to the degenerate $M_J = \pm 1$ sublevel of the $^3P_1$ state of Bi^+ ion (E state in C_{3v} local symmetry). Such an assignment is in good agreement with the experimental fact of the absence of temperature dependent MCD near 700 nm because Bi^+ ion has non-degenerate ground state. Expanding this hypothesis on the other bands of the B series we attribute the transitions $^3P_0 \longrightarrow \, ^3P_2(M_J = 0), ^3P_0 \longrightarrow \, ^3P_2(M_J = \pm 1)$ and $^3P_0 \longrightarrow ^1D_2$ to the B2, B3 and B4 bands, respectively. The temperature dependences of the MCD bands in D and C series are rather different, therefore we assume their different nature.

5.1.2   MCPL spectra

Fig. 5.2 shows the spectra of the total (I_{tot}) and MCPL ($I^+ - I^-$) intensities in the NIR spectral region under excitation into the absorption band D2, $\lambda_{exc} = 532$ nm. The MCPL spectrum is temperature dependent, thus the initial state of the emission transition is a spin multiplet. However, it is red shifted comparing to the luminescence band (250 cm^{-1}) with a peak value of polarization $\Delta_{MCPL} = -0.024$ measured at 1110 nm in the magnetic field B = 6.5 T at 1.48 K. This shift indicates that the PL band consists of two transitions: the shortwavelength shoulder is dominated by the transition from $M_S = 0$ sublevel, while the longwave by the component with a non-zero spin projection of the excited state with the effective spin S. The broad shoulder near 1300 nm is, most probably, due to the presence of Bi ions clusters.

In the visible region under the same excitation at 532 nm we observed a broad emission band with the intensity peak at 700 nm (Fig. 5.3). The MCPL exhibits rather complicated temperature behaviour. At low temperatures it has negative sign with the peak at 660 nm. With increasing of temperature the MCPL changes
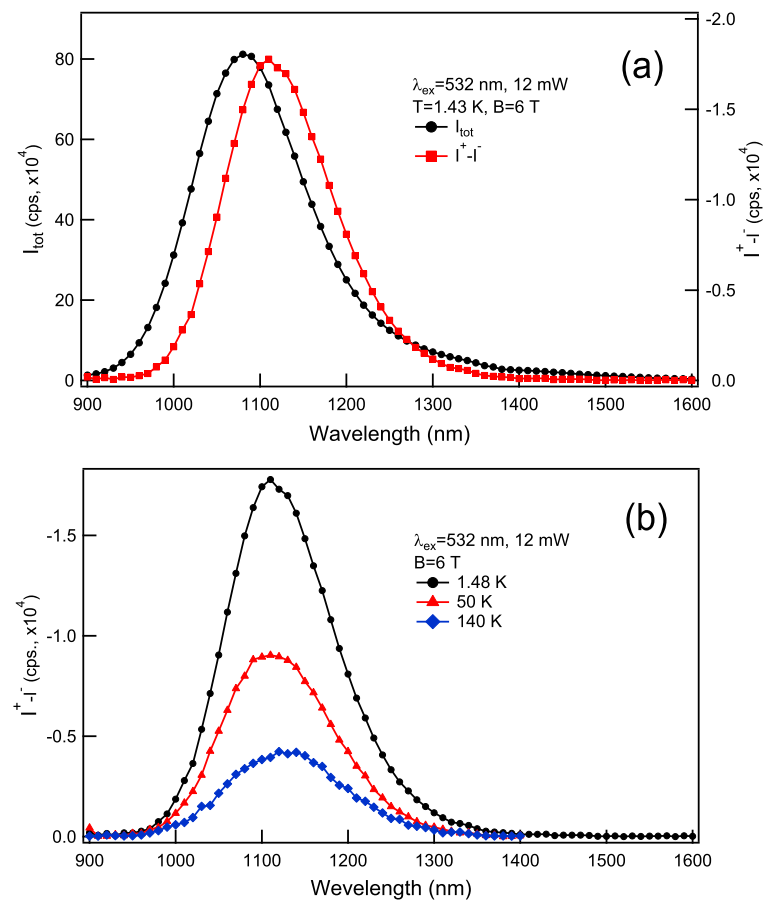
FIGURE 5.2: (a) Spectra of total intensity (I_{tot}) and MCPL ($I^+ - I^-$); (b) temperature dependence of the MCPL spectrum.
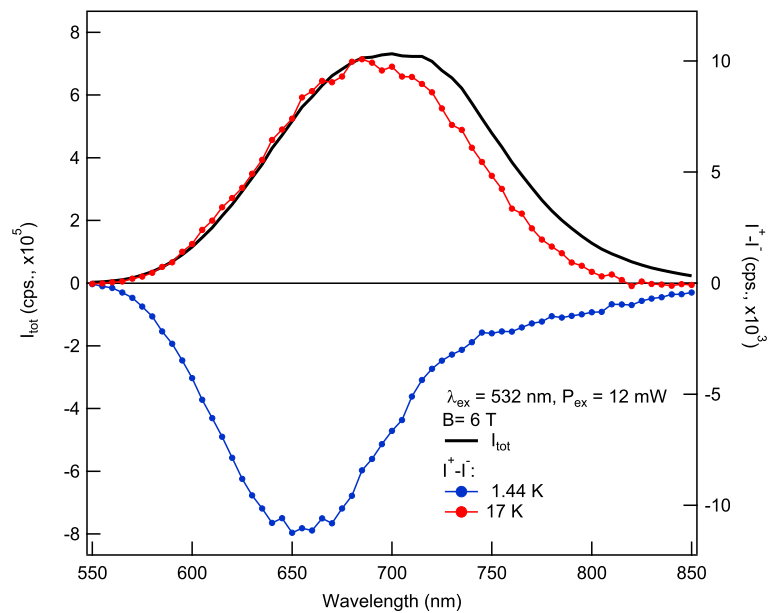
FIGURE 5.3: Spectra of the total (I_{tot}) and MCPL ($I^+ - I^-$) intensities measured under excitation at 532 nm.

its sign and shifts to the lognwavelength region with the peak at 690 nm measured
at 17 K. The change of the MCPL sign can be explained only by the presence of
two transitions at least. These transitions can occur within one centre, but also
they can originate from different centres.
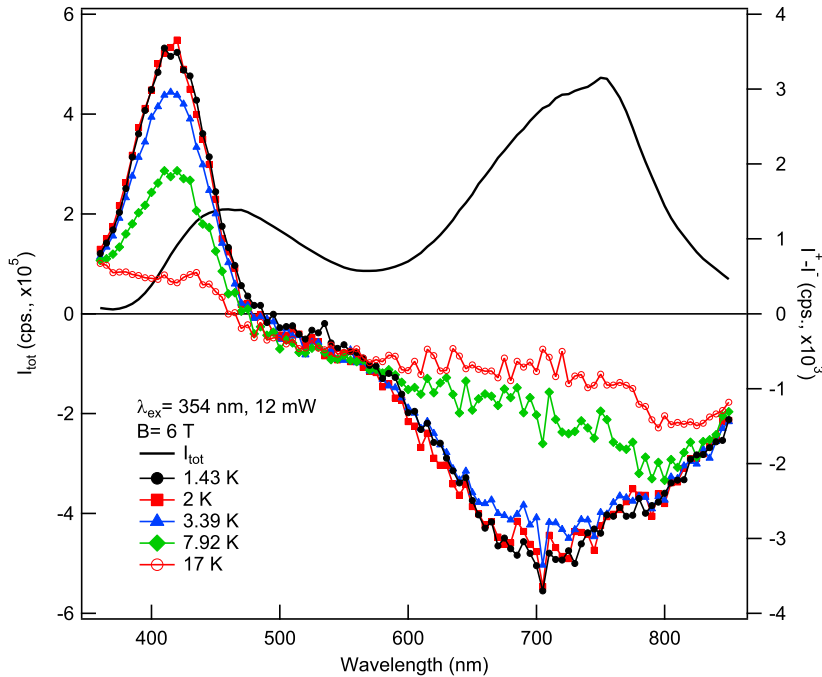
FIGURE 5.4: Spectra of total (I_{tot}) and MCPL ($I^+ - I^-$) intensities measured under
excitation at 354 nm.

Under excitation at 354 nm (B4 band) the 'red' luminescence slightly shifts to
the longwavelength region with the intensity peak at 750 nm, as it is shown in
Fig. 5.4. Apparently, like in the case of excitation at 532 nm, this band consists of
several transitions, which is confirmed by the MCPL measurements. In addition
to the main MCPL band peaked at 700 nm, there is a weak band with the intensity
peak near 800 nm. It is seen that the polarization degree of this MCPL decays
much slower with the temperature increase. Another luminescence band has its
intensity peak at 460 nm, however, the MCPL is significantly blue shifted. The
MCPL band is temperature dependent and almost vanishes at T = 17 K.

5.2 Saturation measurements

MCD saturation curves were recorded at the peaks of C1, C2, D2 and D3 bands. The magnetic field dependences of the MCD bands in the visible, D2 and D3, are shown in Fig. 5.5(a, c). It is seen that the MCD saturation curves for both bands exhibit a very small degree of the nesting and tend towards a saturation at high field magnitude. The temperature dependences recorded at fixed MF and plotted as a function of 1/T are shown in Fig. 5.5(b, d). They also do not exhibit any unusual peculiarities. The MCD signal increases with the temperature decrease. Saturation data of the MCD recorded at 375 and 505 nm are considerably similar. Thus it is natural to consider the D2 and D3 bands as belonging to the same centre. At first glance, this centre should have an odd number of electrons (or holes) since the form of the saturation curves is very similar to those inherent to the Kramers doublet (see Fig. 3.8). However, the simultaneous fit of the curves in Fig. 5.5(b,d) revealed the presence of a small rhombic zero-field splitting, which is possible only for a system with an integer effective spin.

In the NIR region the increase of magnetic field causes the well pronounced saturation of ΔA (Fig. 5.5(e, g)). This fast saturation indicates relatively high value of g-factor, while the nesting of the isotherms in MF dependences reveals that the ground state of C1 and C2 bands is a non-Kramers doublet. For magnetic fields 3 T and higher, the curves of temperature dependences ($1/T$ plots, Fig. 5.5(f, h)) are saturated below 5 K and they lie very close to each other. Such a behaviour is also characteristic of systems with an even number of electrons (integer effective spin).

In Fig. 5.6 we show the saturation curves of the MCPL in the NIR PL band recorded at the peak of the MCPL – 1110 nm (see also Fig. 5.2(b)). The isotherms in Fig. 5.6(a) exhibit a very high degree of the nesting and the saturation is completely absent even in the high magnetic fields and low temperatures. On the
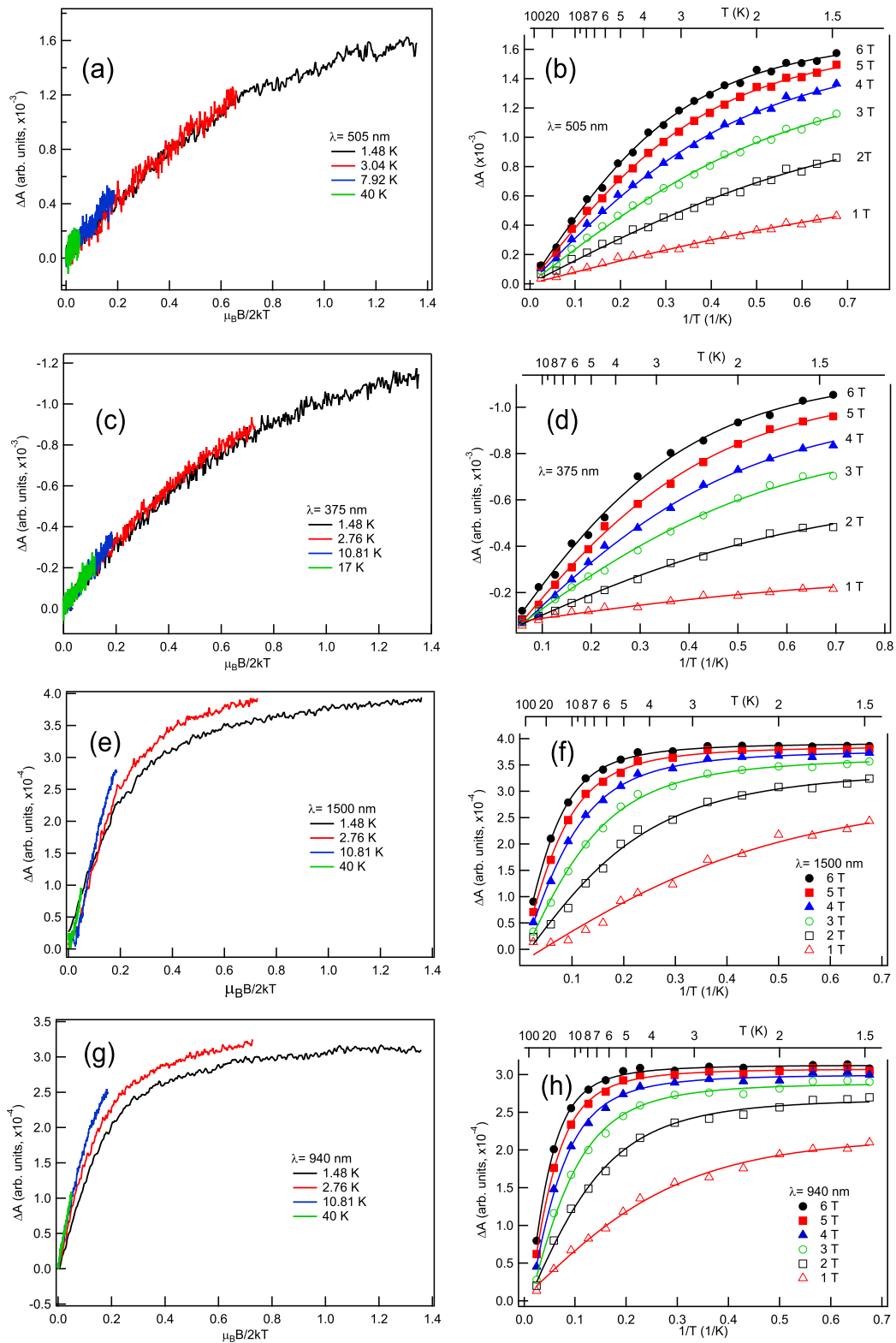
FIGURE 5.5: (a, c, e, g) Magnetic field dependences of ΔA measured at different temperatures; (b, d, f, h) temperature dependences at fixed MF's. Solid lines in (b, d, f, h) are global fit by Eq. (5.2) with $N = 1$.

contrary, when Δ_{MCPL} is plotted as a function of $1/T$, shown in Fig. 5.6(b), the saturation values of Δ_{MCPL} are different for each magnitude of the magnetic field. Such a behaviour of the MCPL signal can be explained by the low value of g-factor and relatively high zero-field splitting. Similar results (shown in Fig. 5.7) were obtained for the MCPL measured at 415 nm under excitation at 354 nm.
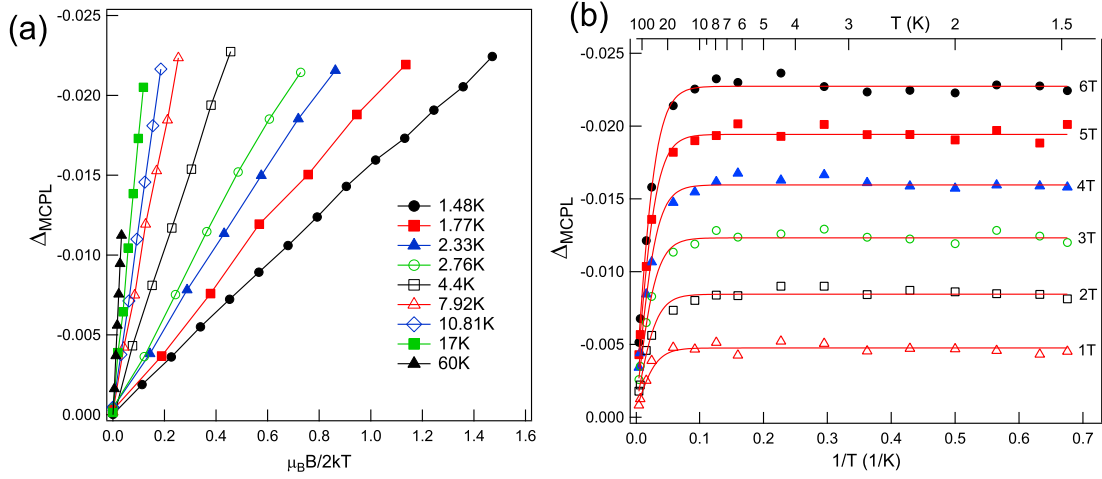
FIGURE 5.6: (a) Magnetic field dependences of Δ_{MCPL} measured at different temperatures; (b) temperature dependences at fixed MF's. $\lambda_{exc} = 532\,\text{nm}$, $P_{exc} = 12\,\text{mW}$, $\lambda_{det} = 1110\,\text{nm}$. Solid lines in (b) are the global fit by Eq. (5.3) with $N = 1$.
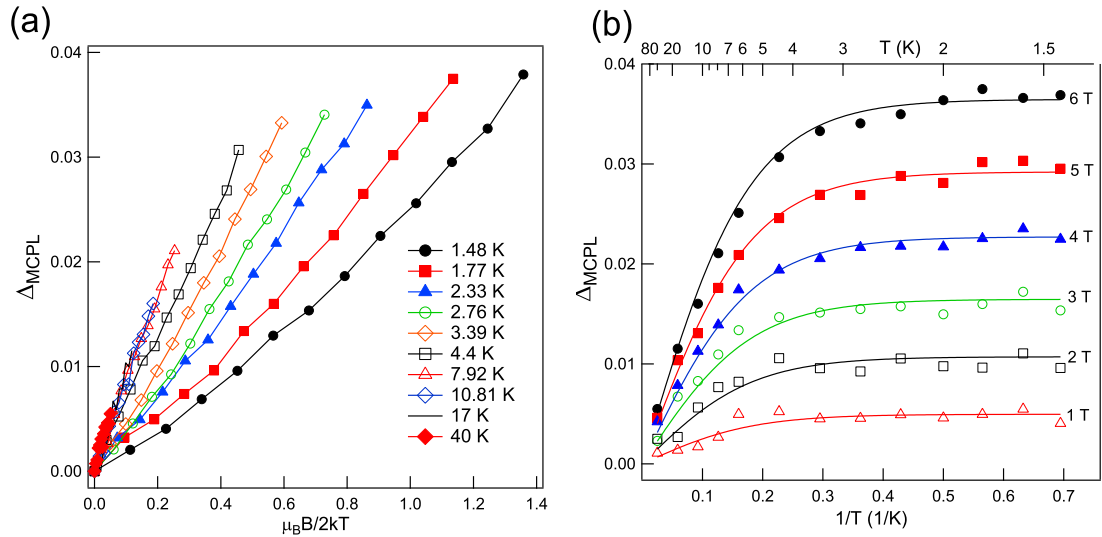
FIGURE 5.7: (a) Magnetic field dependences of Δ_{MCPL} measured at different temperatures; (b) temperature dependences at fixed MF's. $\lambda_{exc} = 354\,\text{nm}$, $P_{exc} = 12\,\text{mW}$, $\lambda_{det} = 415\,\text{nm}$. Solid lines in (b) are the global fit by Eq. (5.3) with $N = 1$.
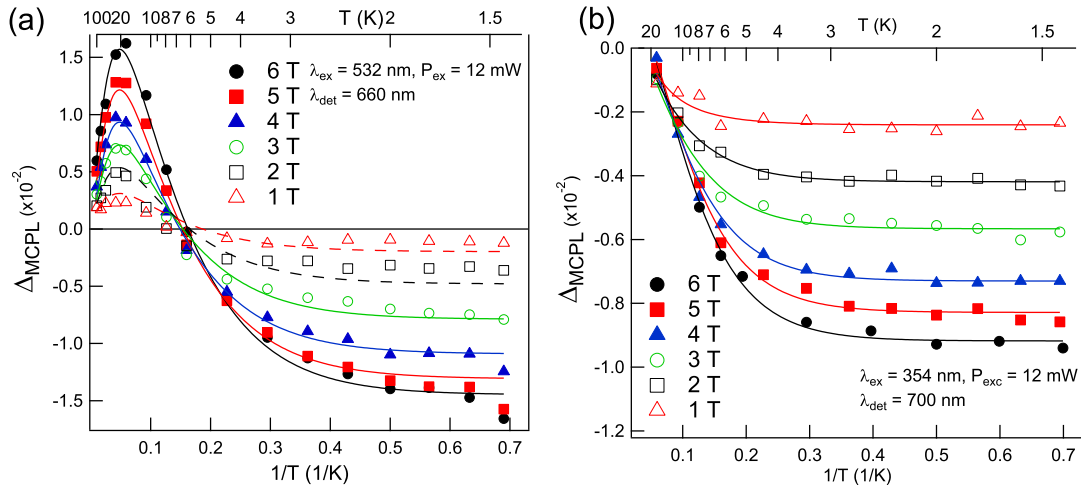
FIGURE 5.8: Temperature dependences of MCPL Δ_{MCPL} measured at 660 nm (a) and 700 nm (b). Solid lines are the global fit by Eq. (5.3) with $N = 2$.

Detailed investigation of the MCPL as a function of MF and temperature was also performed in the "red" luminescence at 660 and 700 nm, corresponding to the locations of the MCPL maximums under excitation at 532 and 354 nm, respectively. The temperature dependences recorded at 660 nm are shown in Fig. 5.8(a). They reveal a non-trivial form. It is seen that the MCPL signal increases with the decreasing temperature and reaches its maximum value $\Delta_{MCPL} = 0.016$ at 17 K and 6 T. Then the Δ_{MCPL} decreases and changes its sign near 6 K. As it was mentioned above, the only way to explain the opposite signs and this temperature behaviour of the MCPL is to assume that the emission is due to the transitions from two excited states with essentially different zero-field splitting energies. At first glance, the saturation curves measured at 700 nm under excitation at 354 nm, (Fig. 5.8(b)), exhibit usual temperature dependences. They are monotonic and do not change the sign. However, the fit of the experimental results was possible only in the assumption of the presence of two different transitions, like in the case of the excitation at 532 nm.

The analysis of the saturation curves were performed in terms of the effective

spin Hamiltonian (3.4) with an axial (D) and rhombic (E) zero-field splitting parameters, caused by the crystal field interaction (see details in Chapter 3). With the assumption that $g_\parallel = g_{zz} \gg g_\perp = g_{xx} = g_{yy}$ the Hamiltonian is

$$\mathscr{H} = D\left\{S_z^2 - \frac{1}{3}S(S+1)\right\} + E(S_x^2 - S_y^2) + g_\parallel \mu_B B S_z \cos\theta \qquad (5.1)$$

In order to produce the temperature dependent $\mathscr{C}$-term, the initial state must be a spin multiplet. For the integer effective spin, for example $S = 1$, it is possible only if the axial parameter $D < 0$. Then the spin multiplet $M_S = \pm 1$ is put to the lowest position and the rhombic component of the crystal field removes the residual degeneracy as it is shown in Fig. 3.9.

The saturation curves of the MCD and MCPL were fitted to the following equations:

$$\Delta A = \sum_{i=1}^{N} A_i^{sat} \int_0^1 \frac{\tilde{g}_i \mu_B B \cos^2\theta}{\sqrt{\Delta_i^2 + (\tilde{g}_i \mu_B B \cos\theta)^2}} \tanh\left(\frac{\sqrt{\Delta_i^2 + (\tilde{g}_i \mu_B B \cos\theta)^2}}{2kT}\right) d(\cos\theta),$$

$$(5.2)$$

$$\Delta_{MCPL} = \sum_{i=1}^{N} A_i^{sat} \int_0^1 \frac{\tilde{g}_i \mu_B B \cos^4\theta}{\sqrt{\Delta_i^2 + (\tilde{g}_i \mu_B B \cos\theta)^2}} \tanh\left(\frac{\sqrt{\Delta_i^2 + (\tilde{g}_i \mu_B B \cos\theta)^2}}{2kT}\right) d(\cos\theta).$$

$$(5.3)$$

These are the sum of N Eq. (3.20) with the summation over all transitions from different ES's observed at the given wavelength; $\tilde{g}_i$ is the effective g-factor, which is equal to $4g_\parallel$ or $2g_\parallel$ for $S = 2$ and $S = 1$, respectively. The results of the global fit are collected in Table 5.1.

At the first stage, all the saturation curves recorded in the MCD were fitted separately. It was found that parameters obtained for D3 and C2 bands are very close to those for D2 and C1, respectively. For this reason they were fitted together

TABLE 5.1: Results of the global fit

	λ, nm	A^{sat}, arb. units	$g_\parallel$		Δ, cm^{-1}
			$S = 1$	$S = 2$	
MCD (GS)	375, 505 (Defect)	$(-33.3 \pm 1.4) \times 10^{-4}$, $(38 \pm 0.1) \times 10^{-4}$	0.9 ± 0.03	0.45 ± 0.02	1.36 ± 0.13
	940, 1500 (Cluster)	$(69 \pm 1) \times 10^{-5}$, $(80 \pm 1) \times 10^{-5}$	4.4 ± 0.02	2.2 ± 0.01	2.77 ± 0.02
MCPL(ES)	415 (X354)	1.66 ± 10.4	0.16 ± 0.85	0.08 ± 0.43	7.43 ± 0.37
	660 (X532)	-1.52 ± 2.4	0.2 ± 0.5	0.1 ± 0.3	7.13 ± 1
		2.25 ± 0.18	0.5 ± 3.7	0.25 ± 1.85	36.3 ± 3.45
	700 (X354)	-0.21 ± 0.09	0.9 ± 0.25	0.45 ± 0.13	10.8 ± 3
		0.7 ± 0.17	0.35 ± 2	0.18 ± 1	27 ± 7
	1110 (X532)	-0.9 ± 2.2	0.9 ± 1.2	0.45 ± 0.6	43.3 ± 1.4

by pairs. It is seen from Table 5.1 that the obtained values of the fitting parameters, namely the zero-field splitting energy Δ and g-factor, are different for the MCD bands in D and C series. It proves the above assumption that the observed Di and Ci bands in the MCD spectrum belong to different centres, though they both are the even-electron systems. We believe that the C bands originate from the clusters of Bi ions due to the very high value of g-factor. Above it was mentioned that the saturation curves of the MCD in the D bands have a form similar to that expected for Kramers doublet. To clarify this point we compared the fits of D2 band saturation curves in the assumption of the Kramers ($\Delta = 0$) and non-Kramers ($\Delta \neq 0$) doublets, shown in Fig. 5.9. It is seen that the results are identical. It should be noted that this result is not surprising for very small value of zero-field splitting predicted by the model. However, the value of χ^2 (defines how well experimental data fits a model) is less for the case of the non-Kramers doublet. For these reasons we conclude that the MCD in the visible is due to the transitions from the non-Kramers doublet. The relatively high energy of zero-field splitting in GS's is the main reason why no ESR signal can be detected in X-band (9.8 GHz, 0.33 cm^{-1}). It is worth noting that the obtained g-factor for the GS associated with the MCD at 375 and 505 nm are essentially small. Summarizing these experimental results we assign all the Di bands, and the NIR PL at

1100 nm as well, to the defect in the glass network.
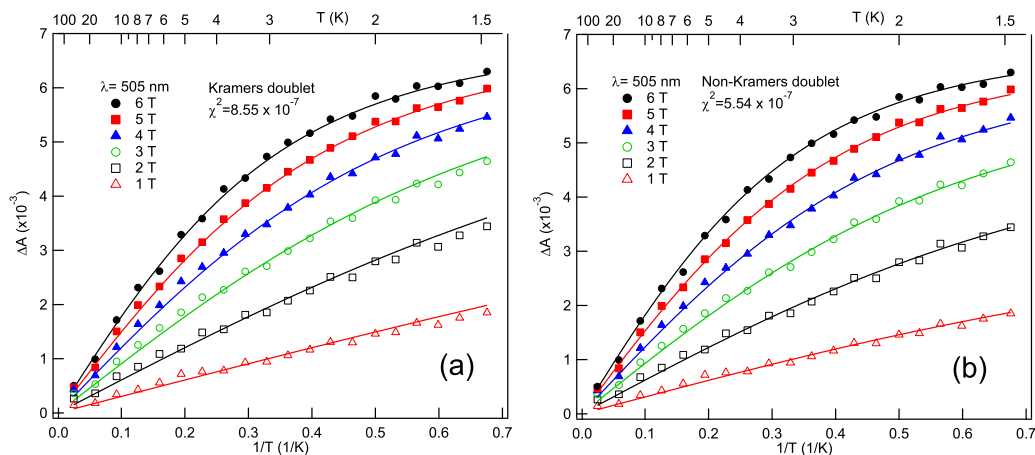
FIGURE 5.9: Comparison of saturation curves fits at 505 nm in the assumption of (a) Kramers and (b) non-Kramers doublets.

The fits of MCPL saturation curves have definitely revealed that the observed transition bands belong to centres with an even number of unpaired electrons. One can note the essential error in g-factor values. It is well-known that the fit parameters can be well determined only if they provide comparable contributions. When we are dealing with a non-Kramers doublet, the energy gap between its sublevels is a sum of two contributions — Zeeman and zero-field splitting energies. It is seen that even at high magnetic fields, the major splitting in the excited state is provided by the crystal field. For example in the first excited state, responsible for the NIR PL, the energy splitting consists of ZFS $\Delta = 43.3$ cm^{-1} and Zeeman energy $\tilde{g}\mu B \simeq 5$ cm^{-1} at the magnetic field B = 6 T. The latter is significantly lower, about one order of magnitude. On the contrary, the ground states investigated in the MCD have comparable energies of Zeeman and zero-field splitting, as a consequence, the fit errors are very small.

The MCPL of the 'red' luminescence consists of two oppositely signed components. The negative shortwavelength component has lower zero-field splitting energy comparing to that of the positive component. That is why it was possible

to distinguish them by measuring the MCPL spectrum at different temperatures. At low temperatures the negative component dominates. When the temperature is high enough it decays, while the positive component still has relatively strong polarization due to the high ZFS. As a result, the non-trivial temperature dependence of MCPL signal was observed. The obtained values of g-factors and ZFS energies Δ under excitation at 354 and 532 nm are the same within the fit error. We suppose that in both cases the excitation of the same states takes place, though the luminescence band is slightly shifted. The magnitude of the positive MCPL component under excitation at 354 nm is rather small. For this reason the corresponding fit parameters are not so accurate.

5.3   MCD detected via luminescence

Our experiments on MCD and MCPL do not provide directly the information about the degree of degeneracy of multiplets. The analysis of the transitions in the defect in the external magnetic field revealed that the ground and excited states of the centre may have effective spin $S = 1$ or $S = 2$ as well. To clarify this point we performed an additional experiment on the detection of MCD via luminescence.

In general, the idea of the experiment is to detect the influence of the MCD on the NIR PL intensity. Due to the effect of MCD, at low temperatures and high magnetic fields the intensity of the **total** luminescence under excitation by σ^- and σ^+ polarizations may be different. In the frame of the simplest model shown in Fig. 5.10(a), according to the selection rules the excitation of the first ES at low temperature can be performed by two channels: $|1, +1\rangle^g \longrightarrow |1, 0\rangle^e$ and $|1, -1\rangle^g \longrightarrow |1, 0\rangle^e$. Due to the spin relaxation processes the total PL will consist of transitions $|1, 0\rangle^e \longrightarrow |1, \pm1\rangle^g$ and $|1, \pm1\rangle^e \longrightarrow |1, 0\rangle^g$. Because of population difference the absorption from $|1, +1\rangle^g$ (σ^+ component) is stronger than from $|1, -1\rangle^g$
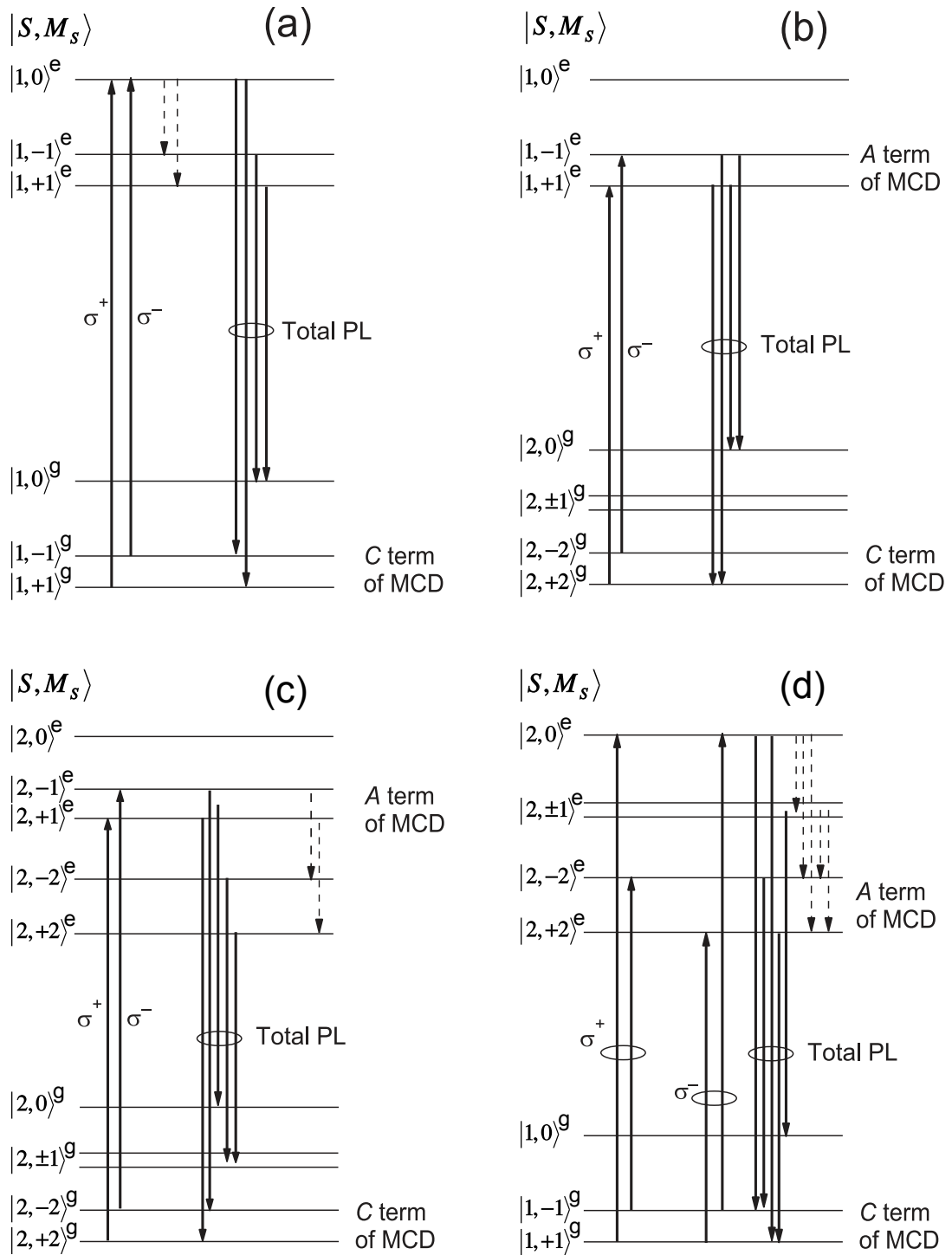
FIGURE 5.10: Energy level diagrams and transitions to explain the detection of MCD in NIR PL. Solid lines correspond to optical transitions, dashed lines – spin relaxation

(σ^- component). Obviously, this difference produces change of the **total** luminescence intensity when the excitation polarization is switched. In Fig. 5.10(b-d) we show more complicate cases, which involve spin quintets in the ground/excited states. The magnitude of the effect in the cases (b) and (c) should be comparable to that of the simplest scheme (a), since there are also only two excitation channels with the prevailing σ^+ component. The quantity we measure in the experiment is $\Delta I = \dfrac{I_{tot}(\sigma^+_{pump}) - I_{tot}(\sigma^-_{pump})}{I_{tot}(\sigma^+_{pump}) + I_{tot}(\sigma^-_{pump})}$, where $I_{tot}(\sigma^+_{pump})$ and $I_{tot}(\sigma^-_{pump})$ are the intensities of the PL under excitation by σ^+ and σ^- polarizations, respectively. The analysis of rate equations revealed that for these three cases signal should be of order 10^{-2} at least.

The most complicate case is shown in Fig. 5.10(d). In contrast to the previous cases, the excitation of the ES can be performed by four channels: $|1, +1\rangle^g \longrightarrow |2, 0\rangle^e$, $|1, -1\rangle^g \longrightarrow |2, 0\rangle^e$, $|1, -1\rangle^g \longrightarrow |2, -2\rangle^e$ and $|1, +1\rangle^g \longrightarrow |2, +2\rangle^e$. It is clear, that optical pumping produces a spin polarization within the ES. Nevertheless, because of the spin relaxation processes the equilibrium population distribution will be reached, though this process does not influence the total emission intensity. Like in the case of the excited state with $S = 1$, shown in Fig. 5.10(a), the absorption from $|1, +1\rangle^g$ state is stronger than from $|1, -1\rangle^g$ ($\mathscr{C}$ term in MCD). It is important that the absorption from the lowest GS sublevel with $M_S = +1$ may be caused by *lcp* and *rcp* light as well. The associated with $\mathscr{C}$ term difference in absorption of σ^+ and σ^- polarized light is

$$\Delta A = N_{+1} |\langle 1, +1|^g\, m_+\, |2, 0\rangle^e|^2 + N_{-1} |\langle 1, -1|^g\, m_+\, |2, -2\rangle^e|^2 - \\ N_{+1} |\langle 1, +1|^g\, m_-\, |2, +2\rangle^e|^2 - N_{-1} |\langle 1, -1|^g\, m_-\, |2, 0\rangle^e|^2, \tag{5.4}$$

where $N_{\pm i}$ is the population of corresponding state and $m_\pm = \mp 1/\sqrt{2}(m_x \pm im_y)$ is the transition operator. Let us denote the probabilities $|\langle 1, \pm 1|^g\, m_\pm\, |2, 0\rangle^e|^2 = A_{10}$

and $|\langle 1, \pm 1|^g\, m_\mp\, |2, \pm 2\rangle^e\,|^2 = A_{12}$. Then Eq. (5.4) can be rewritten

$$\Delta A = N_{+1}A_{10} + N_{-1}A_{12} - N_{+1}A_{12} - N_{-1}A_{10} = \Delta N(A_{10} - A_{12}), \qquad (5.5)$$

where $\Delta N = N_{+1} - N_{-1}$ is the population difference in the GS. It is seen that the difference in absorption of $\sigma^\pm$ light caused by MCD $\mathscr{C}$ term can be observed only if $\Delta N \neq 0$ and $A_{10} \neq A_{12}$. Therefore, the magnitude of the effect associated with the MCD $\mathscr{C}$ term can be extremely low or even absent if the transition probabilities A_{10} and A_{12} are equal. Even so, the analysis of rate equations showed that the changes in the total PL intensity of order 10^{-6} can be detected due to the diamagnetic $\mathscr{A}$ term of MCD. The measurements of magnetic field dependences at different temperatures can distinguish contributions of $\mathscr{A}$ and $\mathscr{C}$ terms.
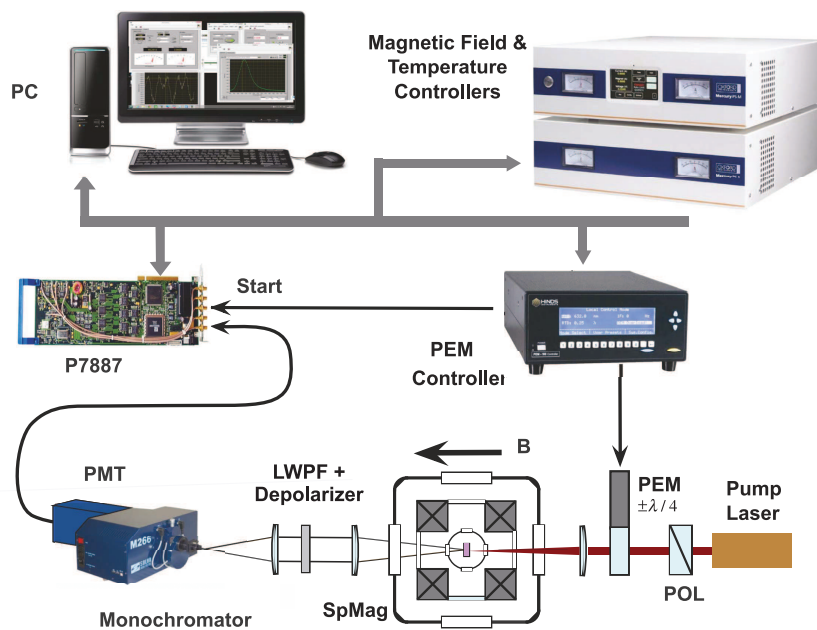
FIGURE 5.11: Experimental setup. LWPF - long wave pass filter; POL - polarizer; PEM - photoelastic modulator; SpMag - cryomagnetic system; PMT - photomultiplier tube; P7887 - photon-counting cart.

The scheme of the experimental setup is shown in Fig. 5.11. The beam of the pump laser (Ti:Sapphire, Coherent Inc.) tuned to 1010 nm is polarized vertically by the Glan-laser prism. The PEM with its birefringent axis oriented at 45° to the

plane of polarization of the light periodically transforms it to the σ^+/σ^- polarized light, as it was explained in Chapter 4. We take the following measures in order to weaken the influence of the pump beam in the recorded luminescence. First, the incident beam is slightly deviated ($\sim$1–2°), so that it is focused at 2–3 mm from the entrance monochromator's slit. Then it passes through the interference long wave pass filter with the edge wavelength 1086 nm and optical density >6 (Semrock, BLP01-1064R-25). Finally, we install the depolarizer to avoid the appearence of the polarization effect of the monochromator. Since we expected very low signal level, the photon-counting technique was implemented.
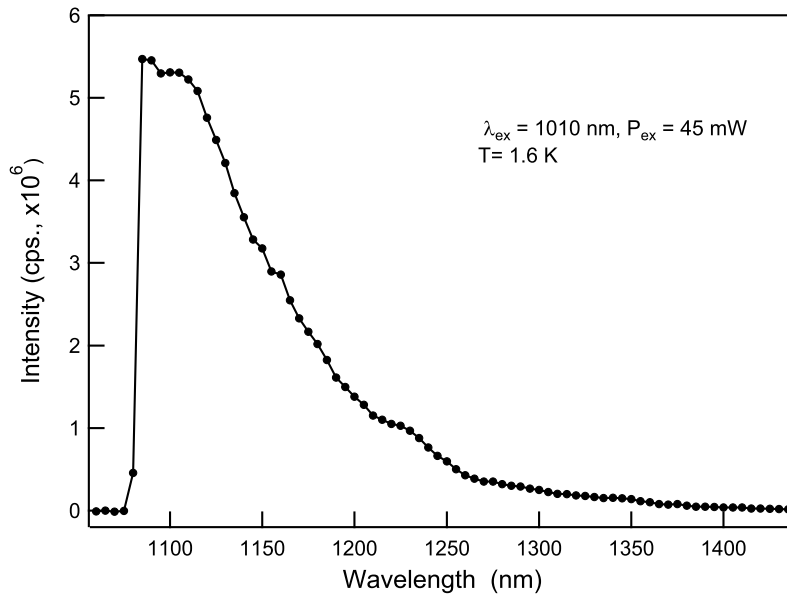
FIGURE 5.12: Spectrum of luminescence in Bi-doped Ma-Al-Si glass under excitation at 1010 nm.

In Fig. 5.12 we show the spectrum of the NIR PL recorded under excitation at 1010 nm at T = 1.6 K. Apart from the influence of the filter, this spectrum does not exhibit any particular features and it is similar to one shown in Fig. 5.2(a) ($\lambda_{exc} = 532$ nm).

The example of the recorded signal is shown in Fig. 5.13. It is seen that the total PL intensity is different for σ^+ and σ^- polarizations of the excitation light. The signal has a cosine form with a high intensity in the first half-cycle. It follows

that, the absorption of the σ^+ component is higher, which agrees with the sign of the MCD measured near 500 nm. The observed signal is very weak. For example at T = 1.6 K and in the magnetic field B = 6 T $\Delta I = (2.4 \pm 0.6) \times 10^{-4}$.
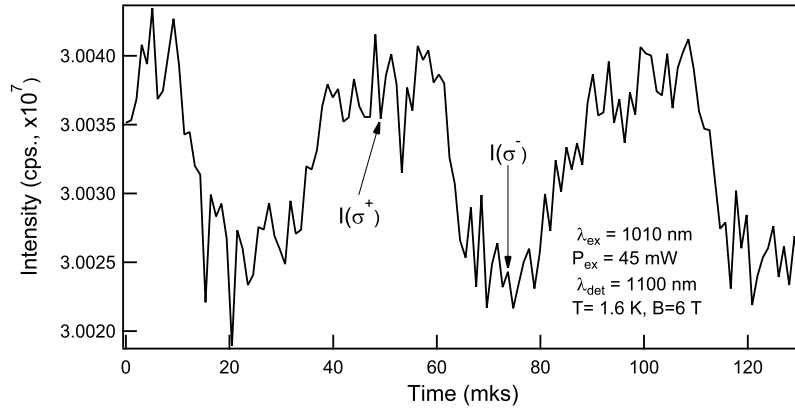
FIGURE 5.13: Intensity of total luminescence measured at 1100 nm under polarization modulated excitation. T = 1.6 K, B = 6 T.
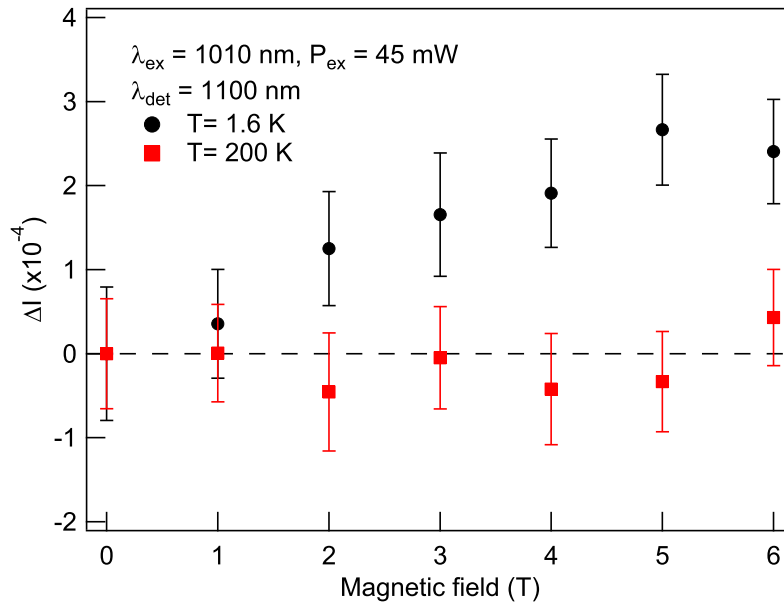
FIGURE 5.14: The magnetic field dependence of ΔI_{tot}

To check the origin of this signal we performed the measurements of the magnetic field dependences at various temperatures. In Fig. 5.14 we show the MF dependences recorded at T = 1.6 K and T = 200 K. It is seen that at low temperature the signal increases with the increase of MF. As it was mentioned above the field dependence of ΔI can be produced by any of the MCD terms. However,

at T = 200 K the signal magnitude fluctuates near its zero value within the experimental error. The total signal quenching is associated with the equalization of populations of the magnetic (spin) sublevels in the ground state. Thus, our experiment unequivocally proves that the GS of the centre associated with the NIR PL is a spin multiplet. Since the small magnitude of the signal was expected only for the case (d), we conclude that the ground and excited states of the defect centre are the spin triplet and quintet, respectively (Fig. 5.10(d)).

5.4 Model of the luminescent centres

In the previous sections we have shown experimentally that the transition bands of the D and B series in the absorption, excitation and MCD spectra should be assigned to the transitions within the defect and Bi^+ ion, respectively. We started the development of the consistent model of the optically active centres in Bi-doped aluminosilicate glass with the quantitative analysis of the electronic states of the Bi^+ ion. We performed the numerical calculations in terms of the theory of ligand field splittings of $p^{2,4}$ configurations following Davis et al. [42]. In this approximation the ligand field potential is a sum of the axial B_0^2 and rhombic B_2^2 components. The energy of the electronics states were calculated by the diagonalization of the Hamiltonian matrix (see details in Appendix B). This matrix was set up using the full basis set of 15 states because of the strong spin-orbit coupling, which can be comparable to the crystal field interaction.

In Fig. 5.15(a) we present the results of these calculations. The spin-orbit interaction splits the ground term ^3P into three levels $^3P_0, ^3P_1$ and $^3P_2$. The axial component of the crystal field B_0^2 further splits them producing two non-degenerate, A_2 ($^3P_1(0)$) and A_1 ($^3P_2(0)$), and three doubly degenerate, E ($^3P_1(\pm1)$, $^3P_2(\pm1)$ and $^3P_2(\pm2)$) excited states. In the notations used by Griffith [47, 69] these states are
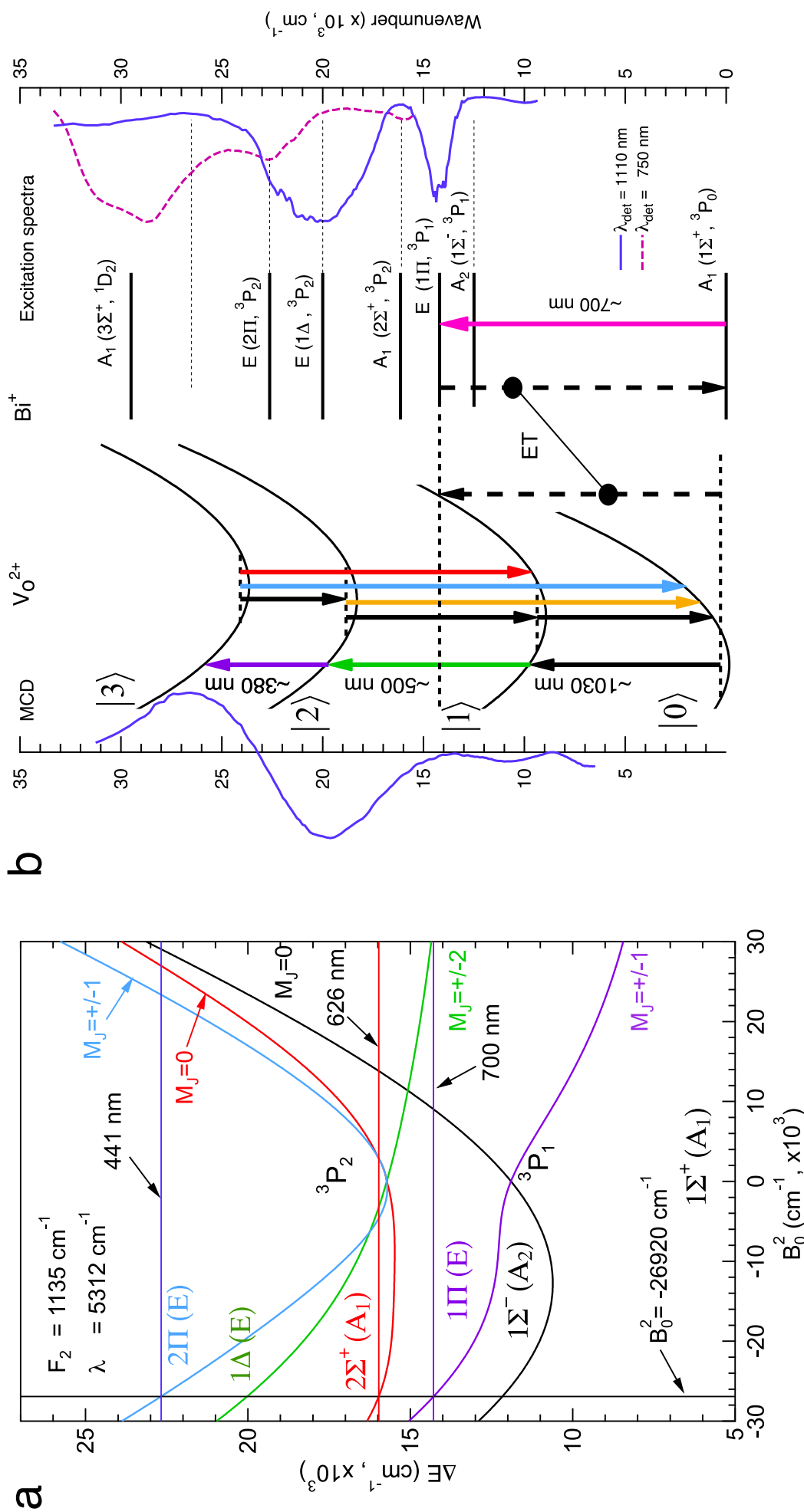
FIGURE 5.15: (a) Energy levels of Bi$^+$ ion in the ligand field as a function of the axial potential parameter B_0^2. Horizontal lines correspond to the experimental positions of the bands B1, B2, B3. (b) The model of the optically active centres with energy transfer processes between them indicated by the dashed lines. Pumping at ~500 nm leads to the excitation of the defect. It is followed by intracenter luminescence. Pumping at ~700 nm leads to the direct excitation of Bi$^+$ ion and it is followed by the energy transfer to the defect (process ET).

labelled as $1\Sigma^-$, $2\Sigma^+$, 1Π, 2Π and 1Δ, respectively. The ground state A_1 ($^3P_0$) corresponds to $1\Sigma^+$ notation. Varying the values of the Slater electron-repulsion integral F_2, spin-orbit coupling constant λ and potential parameter B_0^2 we fitted energies of states to the positions of corresponding bands in B series, namely 14285 (700 nm), 15974 (626 nm) and 22727 cm^{-1} (440 nm). The best fit was obtained for $F_2 = 1135$ cm^{-1}, $\lambda = 5312$ cm^{-1} and $B_0^2 = -26920$ cm^{-1}. It is worth noting that the obtained values of F_2 and λ are close to those of free Bi$^+$ ion, 1175 and 5840 cm^{-1}, respectively [70]. This indicates that Bi$^+$ ion occupies the interstitial position and it does not form the chemical bond with the environment.

The calculations revealed that the band B1 should be assigned to the transition from the ground state $1\Sigma^+$ to the 1Π doubly degenerate excited state, B2 and B3 — to the $1\Sigma^+ \longrightarrow 2\Sigma^+$ and $1\Sigma^+ \longrightarrow 2\Pi$ transitions, respectively. As it was pointed out by Bartram et al. [47] the transition A_1 ($1\Sigma^+$)$\longleftrightarrow A_2$($1\Sigma^-$) between GS and the first ES is rigorously forbidden in C$_{3v}$ local symmetry, in which the state A_2($1\Sigma^-$) is a pure state. The rhombic distortion will admix other states to that involved in this transition making the latter slightly allowed. Apparently, this is the reason why we were able to observe this transition in the anti-Stokes PL in Ga/Bi co-doped silica glass [71] (B1'* band in Fig. 5.16). Nevertheless, it remains very weak and difficult to observe. The similar arguments are valid for the transition A_1 ($1\Sigma^+$)$\longleftrightarrow$E (1Δ). In C$_{3v}$ local symmetry the state E (1Δ) is degenerate and consists mainly (about 90%) from the atomic state $|112 \pm 2\rangle$ with admixture (about 10%) of the components only with M$_J$ = ± 2 of the term $^1D_2$ ($|022 \pm 2\rangle$)^2. Obviously, the above transition is electric- and magnetic-dipole forbidden. The rhombic distortion makes this transition only slightly allowed. For this reason it is also very difficult to observe. While in Pb^0(2) centre in the crystalline SrF$_2$ [47,

---

^{2}Coefficients of the linear combinations of Russell-Saunders states are shown in Tab. B.2 of Appendix B
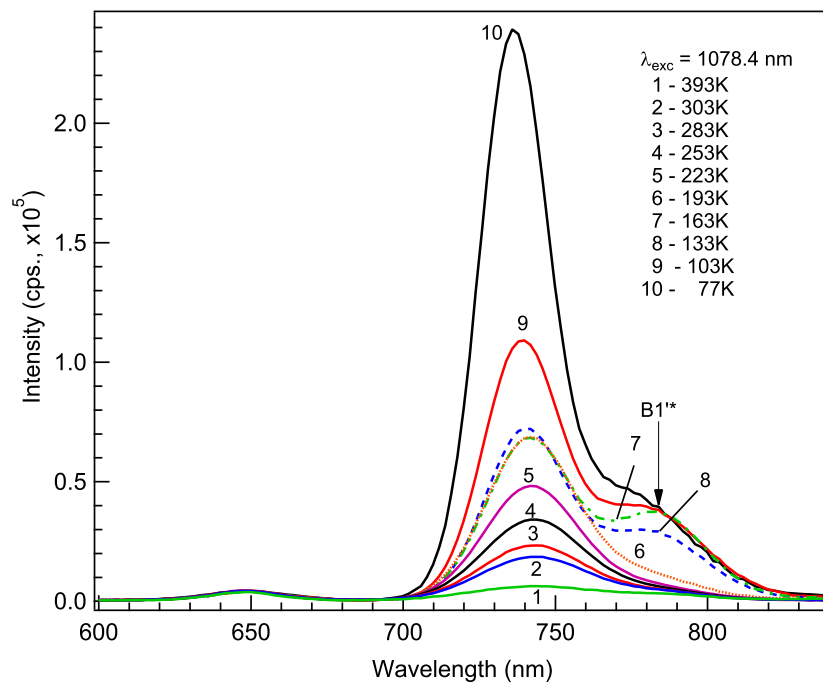
FIGURE 5.16: Anti-Stokes photoluminescence spectra recorded at different temperatures in the range 77-–873 K.

67] A_1 $(1\Sigma^+)\longleftrightarrow E$ (1Δ) transition was not observed for obvious reason, in the disordered silicate glasses it is hidden in the absorption and excitation spectra by the strong allowed transition at 500 nm in the lattice defect.

The estimated value of the axial potential parameter $B_0^2 \simeq -27000$ cm^{-1} is relatively high. The energy of $^1D_2$ states calculated in the frame of our presented model lies above 35000 cm^{-1}, while the transition energy associated with the B3 band is around 30000 cm^{-1}. We believe that at such a strong crystal field the model is at the limit of its applicability, at least for the high energy UV states. For this reason we still assign B4 band to the transition $^3P_0 \longrightarrow$ $^1D_2$ of Bi$^+$ ion.

In Fig. 5.15(b) we show schematically the energy levels of the interacting defect centre and Bi$^+$ ion together with the MCD and excitation spectra. The processes of energy transfer are also shown. It is seen that this diagram allows to rationalize all the peculiarities in the spectra. The NIR PL occurs as a transition $|1\rangle \longrightarrow |0\rangle$ from the first excited state of the defect. This emission can be also

observed under excitation at 700 nm into the E (1Π) ES of the Bi^+ ion due to the energy transfer process labelled as ET.

The absence of any absorption band in the NIR region indicates the forbidden character of the intracenter $|0\rangle \longrightarrow |1\rangle$ transition in the defect, which results in the millisecond lifetime in the first excited state. At the same time, it was shown in [72] that the transition $|1\rangle \longrightarrow |2\rangle$ should be allowed due to the strong ES absorption from the first excited state $|1\rangle$ for the wavelengths shorter than 1000 nm. Therefore the transition $|2\rangle \longrightarrow |1\rangle$ appears as a longwavelength shoulder of the NIR PL.

Usually so-called 'red' luminescence (Fig. 5.3) in Bi-doped materials is assigned to the transition $^2P_{3/2} \longrightarrow {}^2P_{1/2}$ in Bi^{2+} ion. This ion is a system with odd number of electrons (one unpaired electron), so it cannot exhibit zero-field splitting. However, our experimental results on MCPL revealed that this PL originates from two excited states with different ZFS energies. For this reason, Bi^{2+} ion cannot be considered as the origin of 'red' luminescence. In the frame of our proposed model this PL should be caused by the transition $|2\rangle \longrightarrow |0\rangle$ in the defect. It is worth noting that the transition $|3\rangle \longrightarrow |1\rangle$ should have its intensity maximum near 650 nm, thus it also can contribute to the 'red' PL band.

In Fig. 5.17 we show the simplest possible energy level diagram of the 'defect' centre. This model successfully explains the unusual temperature dependence of the MCPL measured at 660 and 700 nm (Fig. 5.8). In the frame of this model, all states are the spin triplets ($S = 1$) except the first ES, which has the effective spin $S = 2$. The pump at 532 nm excites two relatively close-lying states $|2\rangle$ and $|2'\rangle$. These transitions can be observed as a band D2 in the absorption and MCD spectra with the maximum intensity near 500 nm. Two MCPL bands centred at 660 and 690 nm with opposite circular polarizations occur due to the transitions from the lowest spin sublevels $M_S = +1$ and $M_S = -1$ of the $|2\rangle$ and $|2'\rangle$ states, respectively, to the ground state $|0\rangle$. The MCPL selection rules are
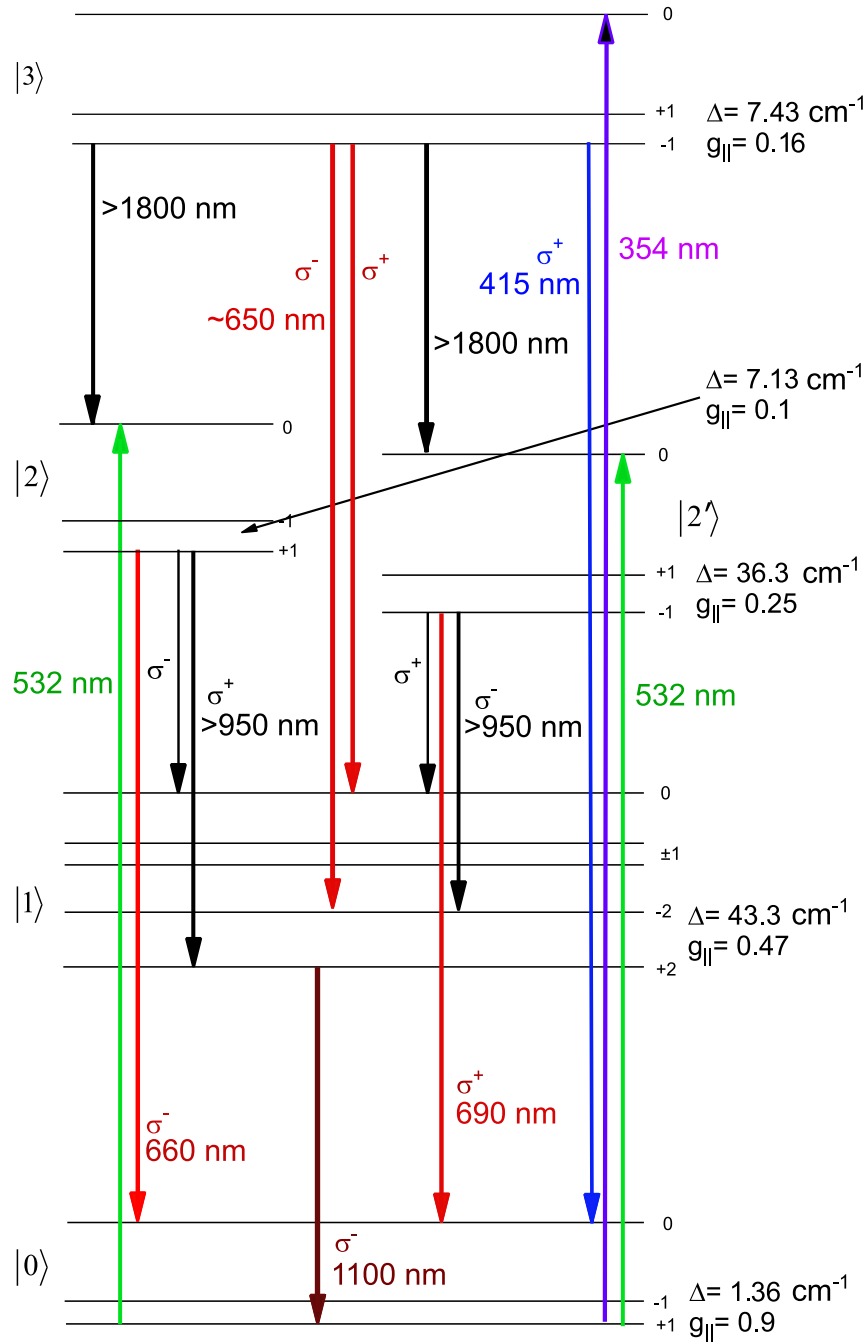
FIGURE 5.17: The energy level diagram to explain the origin of NIR and red luminescence.

$\Delta M_S = M_f - M_i = -1$ for *lcp* and $\Delta M_S = +1$ for *rcp* light. Therefore, the σ^- component of the MCPL corresponds to the transition from the $M_S = +1$ sublevel of the high energy state $|2\rangle$ to the $M_S = 0$ sublevel of the ground state. The σ^+ MCPL component originates from the transition $|2'\rangle\,(M_S = -1) \longrightarrow |0\rangle\,(M_S = 0)$. Pumping at $\lambda_{exc} = 354\,\text{nm}$ excites the third ES $|3\rangle$. The relaxation from this state can be performed by three channels. First channel is the transition $|3\rangle \longrightarrow |0\rangle$ and it was observed as PL band around $450\,\text{nm}$ with MCPL at $415\,\text{nm}$ (Fig. 5.4). Second channel $|3\rangle \longrightarrow |2, 2'\rangle$ should be observed in NIR at wavelength longer than $1.8\,\mu\text{m}$ and, to our knowledge, it had not been observed yet. The processes of spin-lattice relaxation cause the filling of the lowest sublevels of states $|2\rangle$ and $|2'\rangle$. As a result, two components of MCPL appear, like in the just discussed case of excitation at $\lambda_{exc} = 532\,\text{nm}$. Third relaxation channel is the transition $|3\rangle \longrightarrow |1\rangle$ and it should have its intensity maximum at wavelengths near $650\,\text{nm}$. In the frame of proposed model, the emission from the lowest sublevel $M_S = -1$ of the state $|3\rangle$ consists of two components, σ^+ ($|3\rangle\,(M_S = -1) \longrightarrow |1\rangle\,(M_S = 0)$) and σ^- ($|3\rangle\,(M_S = -1) \longrightarrow |1\rangle\,(M_S = -2)$), of comparable intensities. Therefore, total polarization of luminescence should be close to zero.

The model also explains the particular behaviour of the NIR PL kinetics. It had been shown that in the Bi-doped aluminosilicate glass it consists of the slow ($\tau_r \simeq 800\,\mu\text{s}$) and fast ($\tau_r \simeq 2\,\mu\text{s}$) components [26]. Similar behaviour was reported in Ga/Bi co-doped silica glass [29]. According to our model the NIR PL must consist of two components: transition from the first ES to GS $|1\rangle \longrightarrow |0\rangle$ and from the second to the first ES's $|2(2')\rangle \longrightarrow |1\rangle$. To prove this hypothesis we recorded the time resolved spectra under sub-nanosecond pulse excitation at $532\,\text{nm}$ (micro-chip single longitudinal mode laser with $\Delta\nu \simeq 1\text{GHz}$) in the wavelength range 900–$1600\,\text{nm}$ shown in Fig. 5.18. At the initial stage of PL, due to the intensive monochromatic excitation, one can observe the fluorescence line narrowing in the spectrum, which is dominated by two fast components. As it
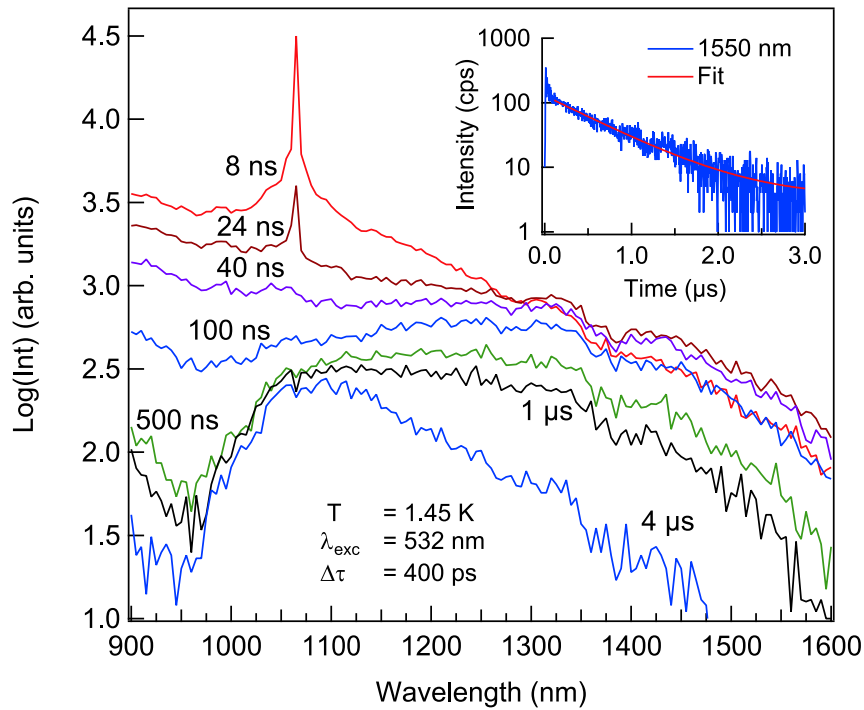
FIGURE 5.18: Time resolved spectra under pulsed excitation at 532 nm.
Inset: fast kinetics measured at 1550 nm.

was mentioned before, the transition $|1\rangle \longrightarrow |0\rangle$ is forbidden, while $|2\rangle \longrightarrow |1\rangle$ is the allowed one. It is seen that the short and long cut-off wavelengths of the forbidden transition are ~950 and 1500 nm. In the inset of Fig. 5.18 the luminescence kinetics measured at 1550 nm is shown. The fit of this kinetics revealed the single exponential decay with the lifetime $\tau_r = 0.64 \pm 0.01 \,\mu$s. Summarizing these experimental facts we assign the slow NIR luminescence to the $|1\rangle \longrightarrow |0\rangle$ transition and the fast one to the $|2(2')\rangle \longrightarrow |1\rangle$.

5.5 Conclusions

The detailed investigation of the Bismuth doped aluminosilicate glass was performed using the MCD and MCPL spectroscopies for the first time. Together with the methods of the conventional optical spectroscopy, we demonstrated the coexistence of at least three optically active centres.

The analysis of the magnetic field and temperature dependences of the MCPL and MCD revealed that all the three centres originate from the systems with an even number of electrons (holes). Two centres have degenerate ground states and they are responsible for the observed MCD signals. According to the MCD experiments, one of the centres exhibits a high value of g-factor in the ground state. For this reason we suppose that the NIR MCD bands Ci are originated from the clusters of Bismuth ions. Two other centres were identified as Bi^+ ion and some defect in the glass network that exchange their energy via the energy transfer.

The developed model of the optical centres successfully explains all the peculiarities observed in the experiments. In the frame of this model the NIR PL is a forbidden transition from the first excited state of the 'defect' centre. Due to the energy transfer this photoluminescence can be also observed under excitation into the ES's of the Bi^+ ion (700 nm). Also it was shown that the 'red' PL originates from the 'defect' centre due to the relaxation from its second ES.

Chapter 6

Bismuth doped pure silica glass

This chapter is devoted to the presentation and discussion of experimental results obtained on a Bi-doped silica glass without other co-dopants. The nanoporous silica glass in form of cylindrical rod with pores of mean diameter 24 nm was fabricated using the sol-gel technique [73, 74]. This xerogel rod was doped by Bismuth using the conventional solution doping technique. After the dehydroxylation procedure under chlorine/oxygen atmosphere the rod was sintered at 1300°C under He atmosphere. The bulk sample with the dimensions 2 mm×4 mm×5 mm was cut from this transparent, colourless monolithic preform. The molar ratio Bi/Si around 400 ppm was measured using the wavelength dispersive x-ray spectroscopy. The relatively high concentration of Bismuth in the synthesized sample results in the sufficiently intense PL, MCD and MCPL signal.

6.1 Absorption, excitation, photoluminescence and MCD/MCPL spectra

The absorption and attenuation spectra were presented previously in [48] in the Bi-doped silica preform and fiber, both fabricated using the same sol-gel technology. In Fig. 6.1(a) we show the absorption spectrum of the bulk preform recorded in the spectral region 300–750 nm. This spectrum consists of two bands with
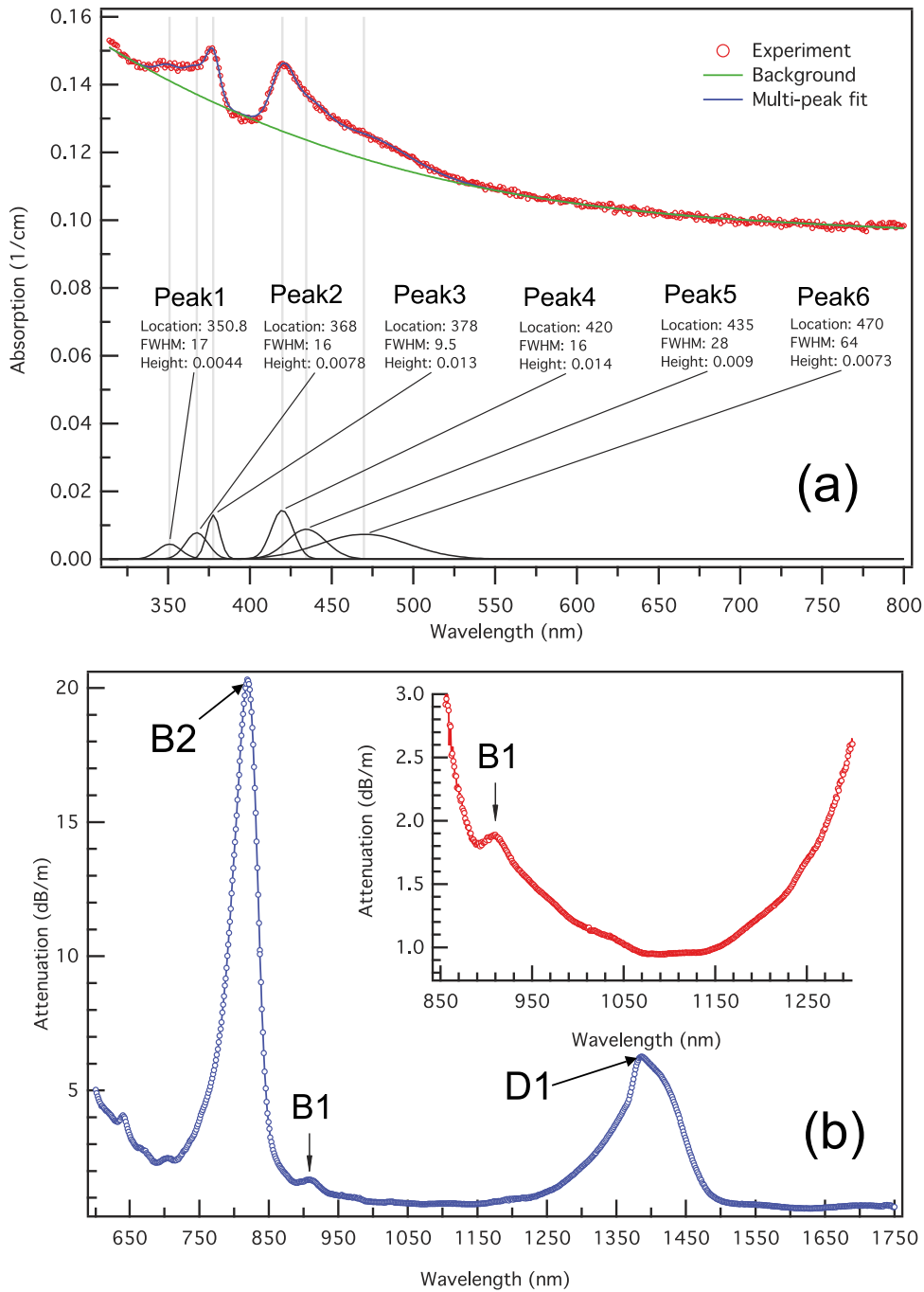
FIGURE 6.1: (a) Absorption spectrum of Bi-doped pure silica sol-gel pre-
form. (b) Attenuation spectrum of Bi-doped pure silica fiber in the range
625–1750 nm. Inset: Detailed view of the spectrum in the range 850–
1300 nm. After [48]

maximums near 380 and 420 nm. Each of these bands can be deconvoluted to three sub-bands as it is suggested by the Gaussian multi-peak fit also shown in Fig. 6.1(a). The Bismuth doping level and length of the bulk sample are too low to observe other absorption bands in visible and NIR regions. To overcome these difficulties the attenuation spectrum of the 3.4 m long piece of Bi-doped fiber was recorded in the range 600–1750 nm and it is shown in Fig. 6.1(b). It reveals the presence of two bands labelled B2 and D1 centred at 810 and 1386 nm, respectively, and a very weak band B1 at 910 nm[1].

The conventional optical spectroscopy of the bulk fiber preform prepared using the sol-gel method was performed by Razdobreev et al. [75]. Under excitation at $\lambda_{exc} = 405$ nm three luminescence bands were observed: two strong with peaks at 830 and 1393 nm and a weak band peaked at 906 nm. The PL spectrum recorded in the NIR region at $\lambda_{exc} = 808$ nm was very similar to that obtained at $\lambda_{exc} = 405$ nm. Under excitation at 532 nm authors reported on five PL bands peaked at 663, 860, 939, 1068 and 1402 nm.

In Fig. 6.2 we show the spectra of photoluminescence recorded under excitation at 375 nm. We observed two strong luminescence bands with the intensity maximums at 1440 and 830 nm labelled PL1 and PL2, respectively. Fig. 6.2 also shows the excitation spectra of these bands recorded at 1440 and 830 nm. There are two bands in the excitation spectrum of the luminescence band PL2 recorded in the spectral region 275–600 nm — bands B3 and B4 with intensity peaks at 415 and 375 nm, respectively. These bands can be put in correspondence to the peaks 3 and 4 of the Gaussian decomposition of absorption spectrum shown in Fig. 6.1(a). The excitation spectrum of the NIR PL1 band reveals similar two bands centred at 375 and 420 nm but with well-pronounced short- and longwavelength shoulders.

---

[1]Data on the absorption and excitation bands are collected in Appendix C
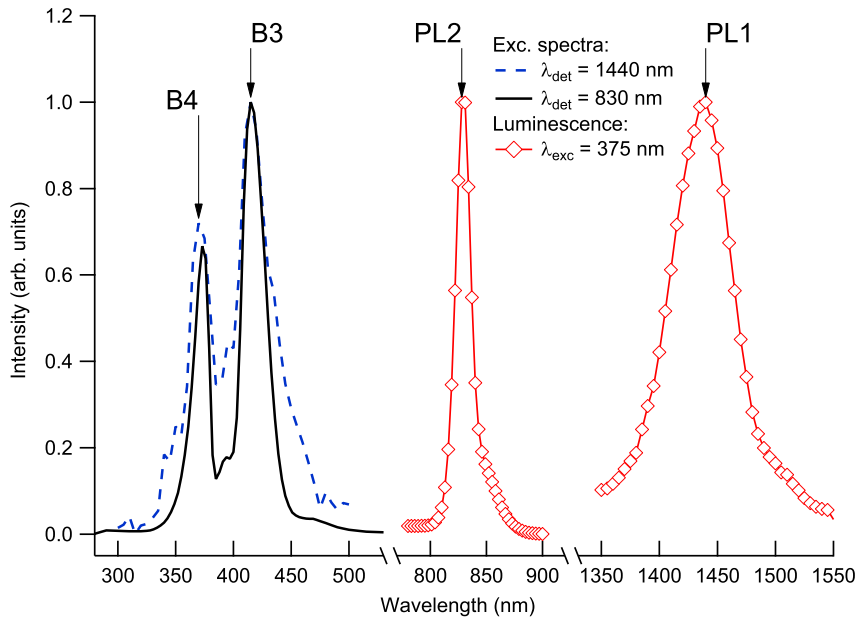
FIGURE 6.2: Normalized excitation and photoluminescence spectra.

The luminescence spectrum recorded in the region 540–900 nm under exci-
tation at 532 nm consists of two bands labelled PL3 and PL4, as it is shown in
Fig. 6.3(a). The most intense band PL4 has the intensity maximum at 650 nm and
the emission band PL3 is centred at 840 nm. In Fig. 6.3(a) we also show the exci-
tation spectrum of the PL4 band. It consists of two bands with peaks at 465 and
350 nm labelled D2 and D3, respectively. These bands cannot be put in correspon-
dence to the bands B3 and B4. Therefore, we conclude that the bands B2–B4 and
D2, D3 belong to different centres. Alternatively, D2 and D3 bands can be put in
direct correspondence to the peaks 1 and 6 of the Gaussian decomposition of the
absorption spectrum shown in Fig. 6.1(a).

The MCD spectra recorded at B = 6 T and different temperatures are shown in
Fig. 6.3(b). They reveals the presence of two bands that coincide with D2 and D3
bands. In the magnetic field B = 6 T and T = 1.45 K we measured $\Delta A = -0.63 \times 10^{-3}$
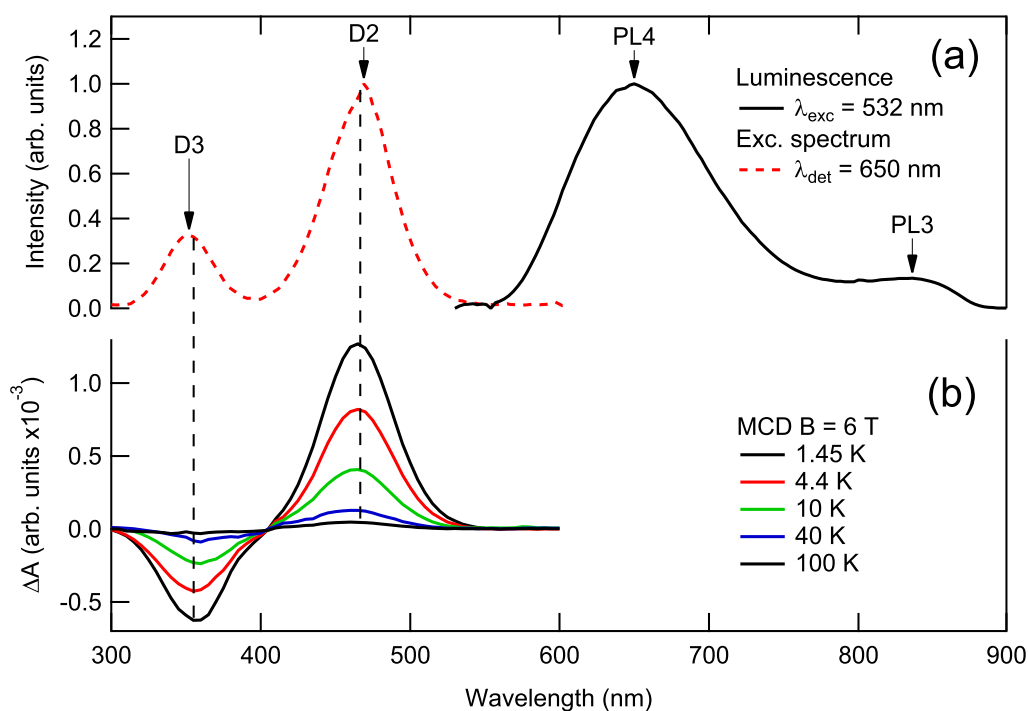
FIGURE 6.3: (a) Normalized excitation and photoluminescence spectra; (b) MCD spectra recorded at the magnetic field of 6 T and different temperatures

and 1.27×10^{-3} at 350 and 465 nm, respectively. The MCD spectrum is temperature dependent, which definitely indicates the spin multiplicity of the corresponding ground state(s). The MCD bands exhibit the same temperature dependence, so they should originate from the same optically active centre. In Chapter 5 the Bi-doped aluminosilicate glass was investigated and we observed additional two MCD bands in the NIR region. These bands were assigned to clusters of Bismuth ions. In Bi-doped silica glass no MCD signal was detected within the spectral region 550–1600 nm. This indicates that in the present sample Bi ions do not form clusters due to relatively low doping level.

The NIR luminescence band PL1 is often assigned to the transition $^3P_1 \longrightarrow ^3P_0$ of Bi^+ ion [18–21]. However, we have shown in Chapter 5 that in the ligand field approximation the crystal field cannot lower the energy of $^3P_1$ state so much (see also Chapter 2 and [42]). On the other hand, the absence of any MCD signal

near 810 nm indicates that the B2 band originates from the centre with a non-degenerate GS. For this reason and because Bi^+ ion has a non-degenerate ground state, we assign the band B2 to the transition $^3P_0 \longrightarrow ^3P_1(M_J = \pm 1)$ of the Bi^+ ion. Following this hypothesis we assign bands B1, B3 and B4 to the transitions $^3P_0 \longrightarrow ^3P_1(M_J = 0)$, $^3P_0 \longrightarrow ^3P_2(M_J = \pm 1)$ and $^3P_0 \longrightarrow ^1D_2$ in Bi^+ ion, respectively.
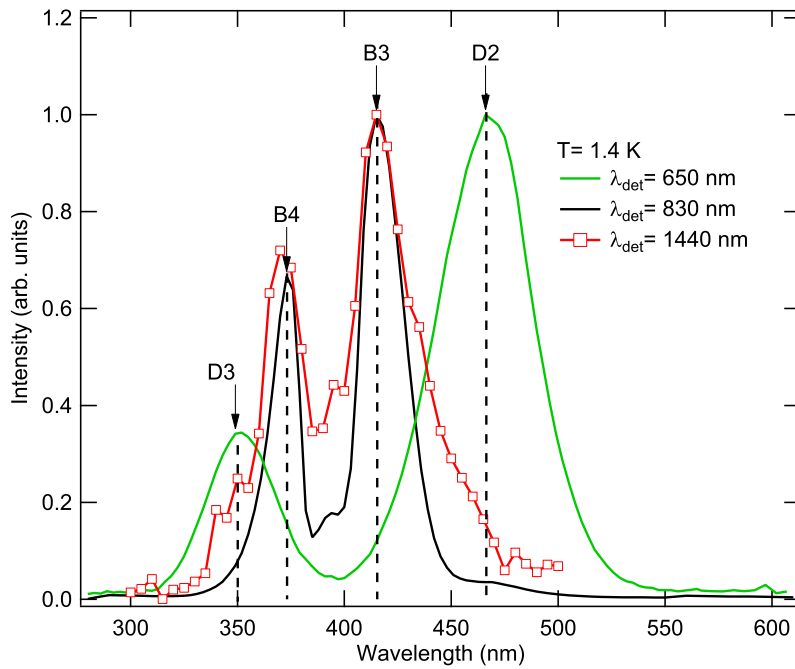
FIGURE 6.4: Normalized excitation spectra recorded at 650, 830 and 1440 nm.

In Fig. 6.4 we show the comparison of the normalized excitation spectra recorded at 650, 830 and 1440 nm, corresponding to the intensity maximums of the luminescence bands PL4, PL2 and PL1, respectively. It is seen that the bands D2 and D3 appear in the excitation spectrum of the NIR PL (1440 nm) as short- and longwavelength shoulders, respectively. This indicates the presence of the energy transfer between Bi^+ ion and the centre responsible for the bands in D series. One can notice a weak peak at 465 nm in the excitation spectrum of PL2 band (830 nm). Most probably this peak should be assigned to the excitation of

the broad luminescence band PL3 centred at 840 nm, which overlaps with PL2 band.
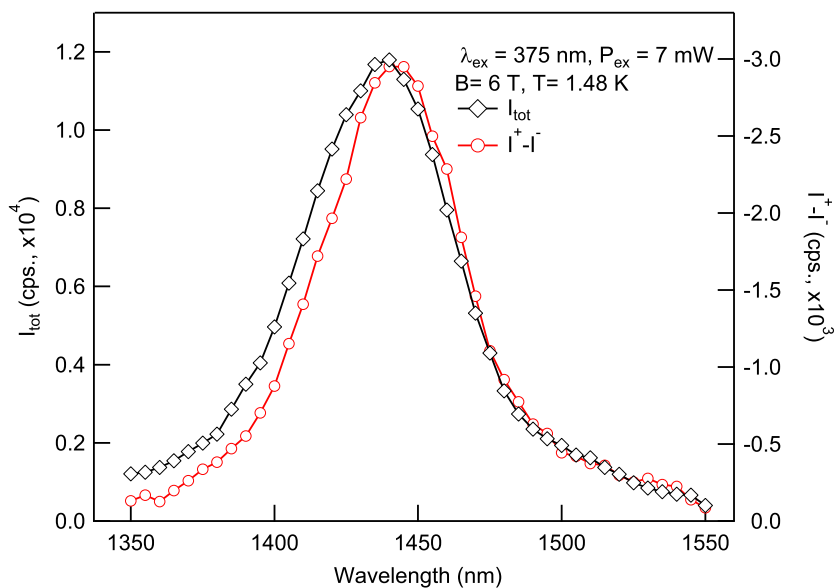
FIGURE 6.5: Spectra of the total intensity I_{tot} and MCPL $I^+ - I^-$ in NIR recorded at B = 6 T, T = 1.48 K.

The detailed investigation of excited states was performed using the MCPL technique. Fig. 6.5 shows the spectra of the total (I_{tot}) and MCPL ($I^+ - I^-$) intensities in the NIR spectral region under excitation at 375 nm. The MCPL is slightly red shifted comparing to the luminescence band (250 cm^{-1}) with the peak value of polarization $\Delta_{MCPL} = -0.28$ measured at 1440 nm in the magnetic field B = 6.5 T and T = 1.48 K. It is worth noting that the MCPL band is narrower than the PL band. The longwavelength side of bands almost coincide, while the short-wavelength side of MCPL is red shifted. This indicates that the PL band consists of two transitions: the shortwavelength shoulder is dominated by the transition from $M_S = 0$ sublevel, while the longwavelength by the transition from the spin degenerate sublevel of the excited state with the effective spin S. It is one more result which denies the assumption that this NIR PL originates from the $^3P_1$ state of Bi$^+$ ion. From Fig. 2.2 and Fig. 5.15(a) it is seen that the energy separation between $M_J = 0$ and $M_J = \pm 1$ components of $^3P_1$ state of Bi$^+$ ion increases rapidly

with the increase of the axial potential component B_0^2 of the crystal field. For example, if the degenerate state $M_J = \pm 1$ is lowered even to $9000\,\mathrm{cm}^{-1}$ ($1110\,\mathrm{nm}$), the energy of $M_J = 0$ level reaches $20000\,\mathrm{cm}^{-1}$ and, as a consequence, the energy gap between these substates should be much more than the measured $250\,\mathrm{cm}^{-1}$.
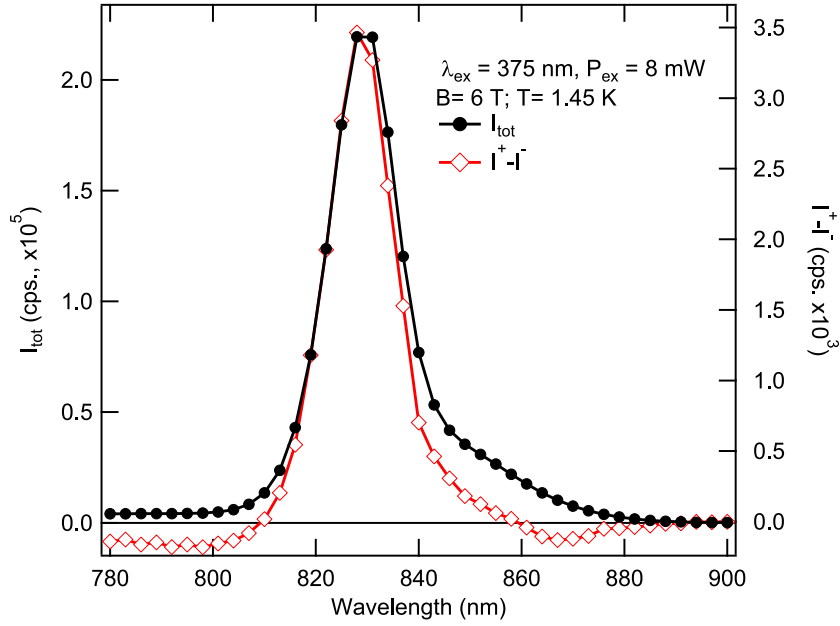
FIGURE 6.6: Spectra of the total intensity I_{tot} and MCPL ΔI recorded under excitation at 375 nm, B = 6 T, T = 1.45 K.

Spectra of PL and MCPL recorded in the region 780–900 nm under excitation at 375 nm are shown in Fig. 6.6. The PL spectrum consists of a strong band with the intensity peak at 830 nm and a longwavelength shoulder (see also Fig. 6.2). The strong positive MCPL band is centred at 830 nm with the maximum degree of polarization $\Delta_{MCPL} = +0.016$ measured at B = 6 T and T = 1.45 K. Also there is a weak, broad MCPL band with $I^+ - I^- < 0$. This negative weak MCPL component should be assigned to the weak residual emission of the band PL3 observed under excitation at 532 nm. Gaussian multi-peak fit of the recorded PL spectrum is shown in Fig. 6.7. The deconvolution reveals the presence of three bands. The low energy band peaked at $11792\,\mathrm{cm}^{-1}$ ($848\,\mathrm{nm}$) causes the longwavelenth shoulder of the luminescence spectrum. The PL2 band consists

of two sub-bands with peaks at $12054\,\text{cm}^{-1}$ (830 nm) and $12092\,\text{cm}^{-1}$ (827 nm). Below we will show that the measurements of the MCPL saturation in this band also reveal the presence of two transitions in PL2 band.
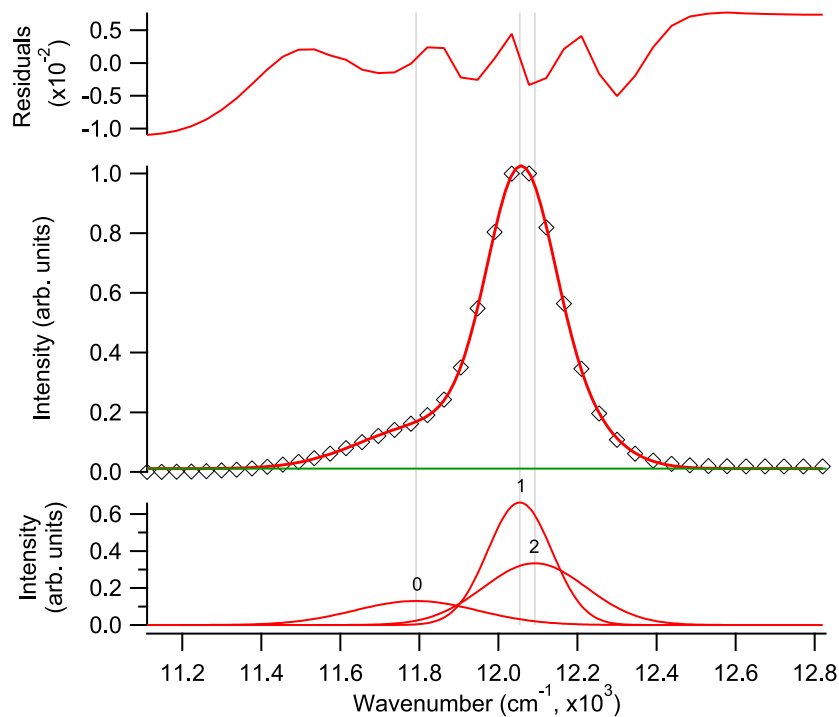
FIGURE 6.7: Gaussian multi-peak fit of the spectrum of total intensity Im_{tot} recorded under excitation at 375 nm, B = 6 T, T = 1.45 K.

In Fig. 6.8(a) and Fig. 6.8(b) we show the spectra of the luminescence (I_{tot}) and MCPL (ΔI) recorded in the spectral range 550–900 nm under excitation at 532 and 450 nm, respectively. In the first case, there are two luminescence bands with the intensity peaks at 650 and 830 nm. The MCPL spectrum recorded in the magnetic field B = 6 T and temperature T = 1.47 K consists of two negative bands with peaks at 640 and 840 nm. It is seen that with increasing of the temperature the band at 640 nm changes its sign and slightly shifts to the longwavelength region with the peak at 650 nm at T = 13 K. In contrast, the longwavelength weak band at 840 nm exhibits simple temperature behaviour. Its polarization only decreases with increase of temperature and does not change sign. Under excitation at 450 nm (Fig. 6.8(b)) the luminescence bands PL4 and PL3 are blue shifted
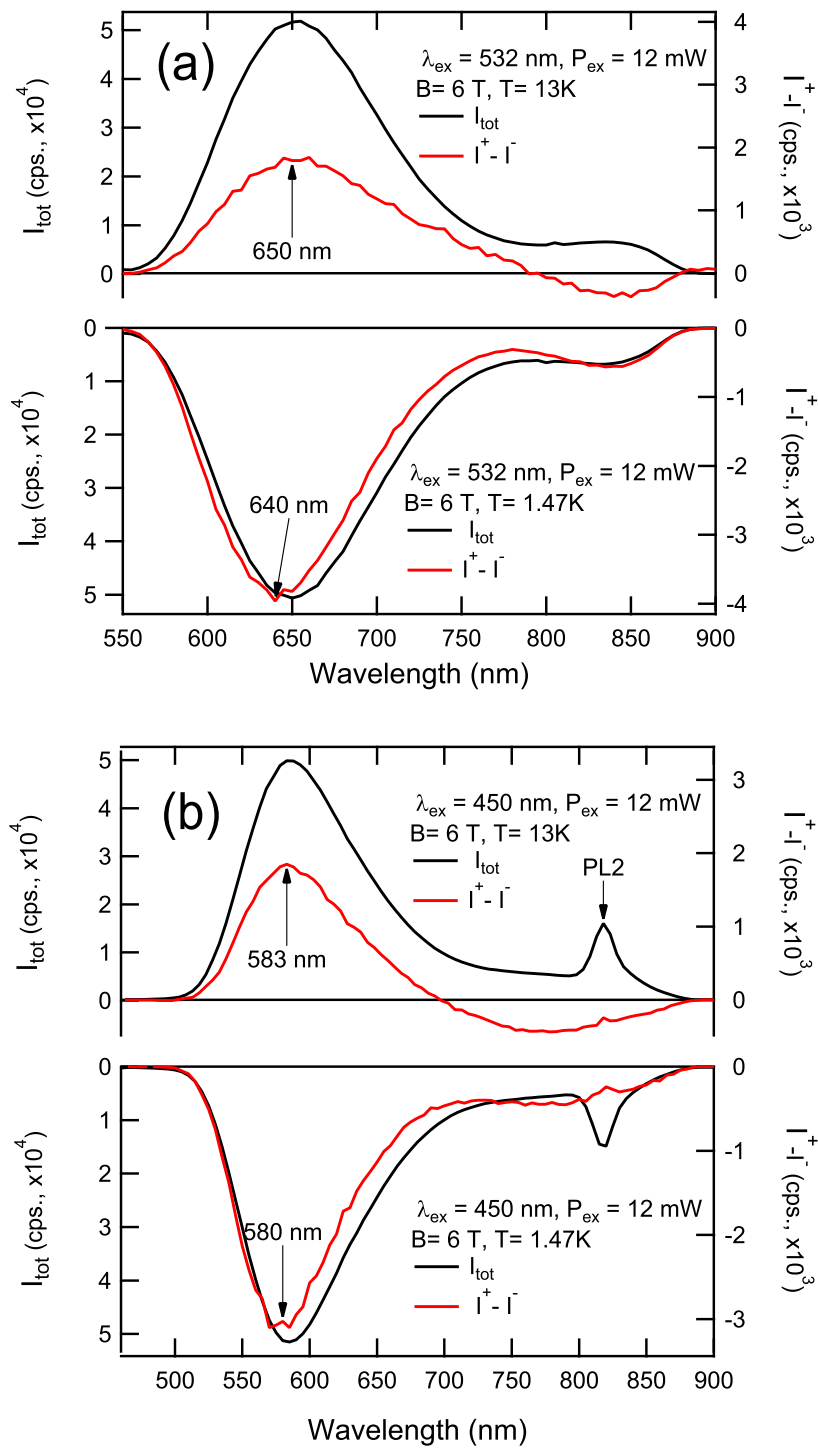
FIGURE 6.8: Spectra of the total intensity I_{tot} and MCPL ΔI recorded at 6 T and different temperatures under 532 nm (a) and 450 nm (b) excitations

and reveal a similar behaviour to those recorded under excitation at 532 nm. The strongest MCPL band exhibits the same unusual temperature dependence that one seen in Fig. 6.8(a). It changes the sign with temperature increase and the maximum intensity shifts from 580 to 583 nm. As it was shown in Chapter 5, such a behaviour of the MCPL can be explained only by the presence of at least two transitions. An additional narrow, well pronounced PL band peaked at 818 nm appears in the spectra, as it is seen in Fig. 6.8(b)). Obviously, it corresponds to the band PL2 observed under excitation at 375 nm.
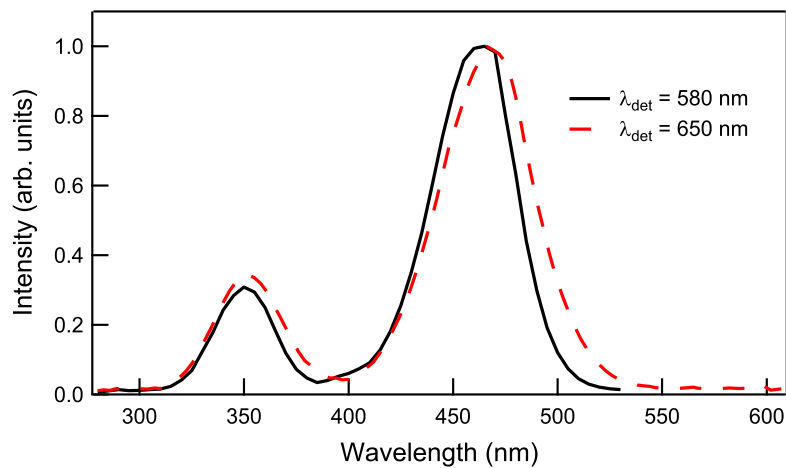
FIGURE 6.9: Normalized excitation spectra recorded at 580 and 650 nm.

To show that the yellow-red luminescence observed at the excitation wavelengths of 532 and 450 nm are of the same origin, we recorded their excitation spectra. In Fig. 6.9 we show the normalized excitation spectra recorded at 580 and 650 nm, corresponding to the locations of the PL maximums measured under excitation at 450 and 532 nm, respectively. It is seen that the excitation bands almost coincide. This indicates that the corresponding PL bands belong to the same type of centres and the difference can be explained by the non-homogeneous broadening. Usually this luminescence is assigned to the transition in Bi^{2+} ions [20, 44, 68, 76]. Relying on the experimental results we will show below that it cannot originate from Bi^{2+} ion.

6.2 MCD and MCPL saturation experiments

6.2.1 MCD saturation

Magnetic field dependences of the MCD, recorded at the peak of the positive band D2 (465 nm), are shown in Fig. 6.10(a). These dependences are plotted as a function of $\mu_B B/2kT$ and it is seen that the saturation curves exhibit a small degree of the nesting. The isotherms do not superimpose and tend towards the saturation at high MF and low temperature.
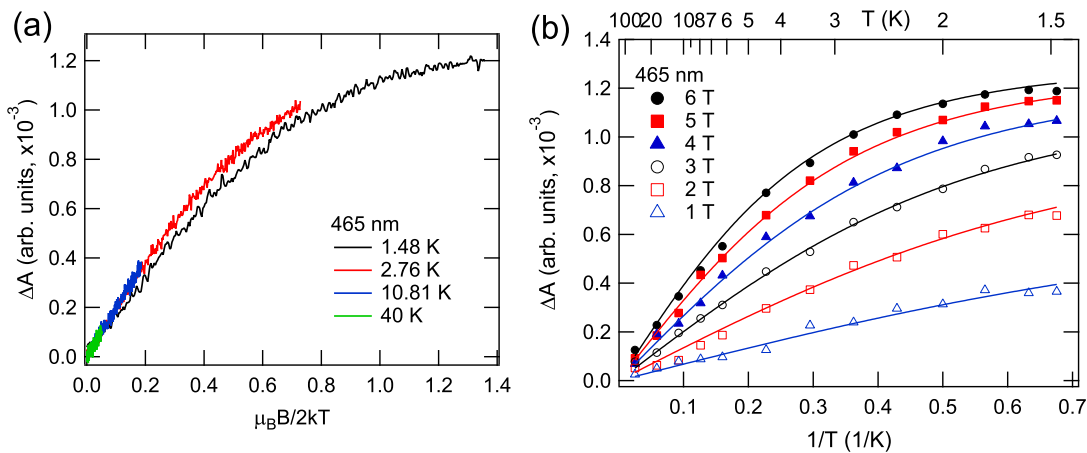
FIGURE 6.10: Magnetic field (a) and temperature (b) dependences of MCD at 465 nm. Solid lines in (b) represent the fit by Eq. (5.2) with $N = 1$

Fig. 6.10(b) shows the temperature dependences of the MCD recorded at fixed magnitudes of the external magnetic field and plotted as a function of $1/T$. They also do not show any unusual peculiarities. The MCD signal increases with a decrease in temperature and it becomes saturated at high magnetic field and low temperature. The presence of the temperature dependence of the MCD definitely indicates the spin multiplicity of the ground state of the corresponding optical centre. At first glance, this centre should have an odd number of electrons (or holes) since the form of the saturation curves is very similar to those inherent to the Kramers doublet (see Fig. 3.8). However, the simultaneous fit of the curves

in Fig. 6.10(b) revealed the presence of a small rhombic zero-field splitting, which is possible only for a system with an integer effective spin. MCD spectra shown in Fig. 6.3(b) revealed the same temperature dependence of D2 and D3 bands. Furthermore, in Chapter 5 we have shown that in Bi-doped Mg-Al-Si oxide glass two MCD bands in visible belong to the same GS.

6.2.2 MCPL saturation

The saturation curves of the MCPL in the NIR PL1 band recorded at the peak of the MCPL (1440 nm) are shown in Fig. 6.11. The isotherms in Fig. 6.11(a) exhibit a well pronounced nesting and there is a tendency towards the saturation at high MF and low temperatures. When the MCPL signal is plotted as a function of $1/T$, the saturation values of Δ_{MCPL} are different for each magnitude of the magnetic field, as it is seen in Fig. 6.11(b). Such a behaviour of the MCPL signal can be explained by the relatively high zero-field splitting.
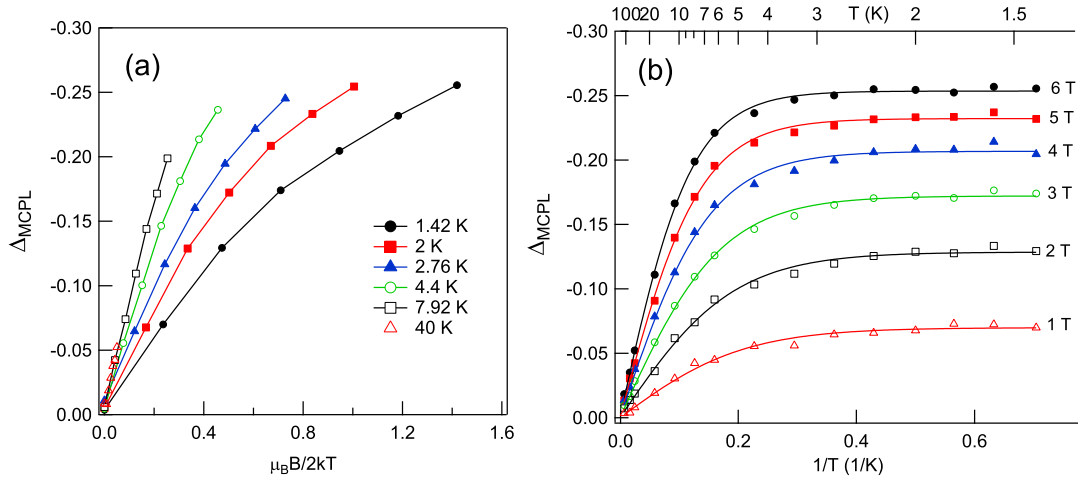
FIGURE 6.11: (a) Magnetic field dependences of Δ_{MCPL} measured at different temperatures; (b) temperature dependences at fixed MF's. $\lambda_{exc} = 375$ nm, $P_{exc} = 7$ mW, $\lambda_{det} = 1440$ nm. Solid lines in (b) are global fit by Eq. (5.3) with $N = 1$.

Detailed investigation of the MCPL in PL4 band as a function of MF and temperature was also performed at 640 and 580 nm, corresponding to the locations of
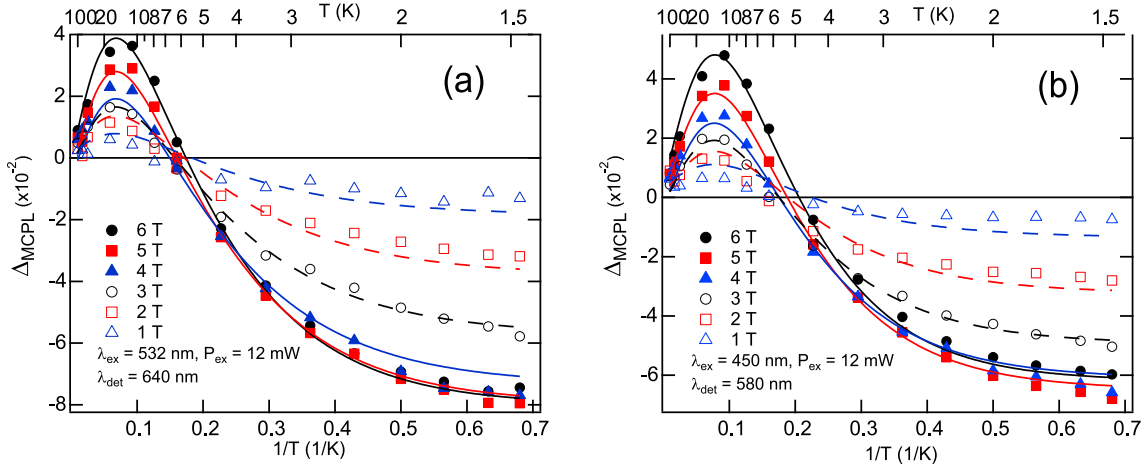
FIGURE 6.12: Temperature dependences of Δ_{MCPL} at 640 nm ($\lambda_{exc} = 532$ nm) (a) and 580 nm ($\lambda_{exc} = 450$ nm) (b). Saturation curves are fitted using Eq. (5.3) with $N = 2$.

the MCPL maximums under excitation at 532 and 450 nm, respectively. The temperature dependences recorded at 640 nm are shown in Fig. 6.12(a). They reveal a non-trivial form. It is seen that the MCPL signal increases with the temperature decrease and reaches its maximum value $\Delta_{MCPL} = +0.04$ at T = 17 K and B = 6 T. Then Δ_{MCPL} decreases and changes its sign near T = 6 K. As it was shown above, the only way to explain such an unusual temperature behaviour of the MCPL is to assume that the emission is caused by the transitions from two excited states with significantly different zero-field splitting energies. Saturation curves recorded at 580 nm under excitation at 450 nm exhibit the same temperature behaviour. Moreover, the global fit of the temperature dependences at various MF in Fig. 6.12(a) and (b) results in very close values of the zero-field splitting and g-factor with the difference within the experimental error. This unambiguously proves the above assumption that the PL bands at 640 and 580 nm originate from the same type of excited states. The presence of ZFS indicates that PL4 luminescence band originates from the even-electron system. As a consequence, this orange-red PL cannot be assigned to Bi^{2+} ion.

Saturation curves of the MCPL in the luminescent band PL3 were recorded at 850 nm under excitation at 532 nm to reduce the influence of the strong PL4 band.
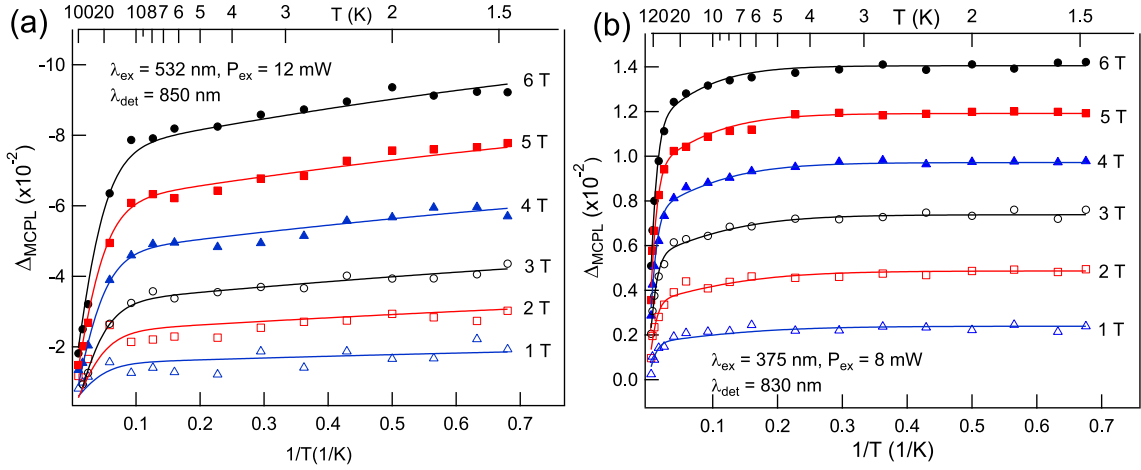
FIGURE 6.13: Temperature dependences of Δ_{MCPL} measured at (a) 850 nm and (b) 830 nm. Saturation curves are fitted using Eq. (5.3), with $N = 2$.

Fig. 6.13(a) shows the MCPL signal Δ_{MCPL} plotted as a function of $1/T$. At first glance, the MCPL has rather simple temperature dependence. The MCPL signal does not change sign and remains negative in the whole measured temperature range. Nevertheless, the fit of the experimental results was possible only in the assumption of the presence of two different transitions.

In Fig. 6.13(b) we show the temperature dependences of the MCPL measured at 830 nm, that corresponds to the PL and MCPL band PL2 under excitation at 375 nm. These saturation curves are monotonic, though the saturation effect occurs at rather high temperature, namely around 20 K. It is worth noting that the global fit of the temperature dependences revealed the presence of two transitions.

6.2.3 Analysis of saturation curves

The analysis of the saturation curves were performed in terms of the effective spin Hamiltonian (5.1) with an axial (D) and rhombic (E) components of the zero-field splitting (see details in Chapter 2 and 5). The saturation curves of MCD and MCPL were fitted to Eq. (5.2) and (5.3) and the results of the global fit were collected in Table 6.1.

TABLE 6.1: Results of the global fit

	λ, nm	A^{sat}, arb. units	$g_\parallel$		Δ, cm^{-1}
			$S = 1$	$S = 2$	
MCD (GS)	465	$(2.8 \pm 0.03) \times 10^{-3}$	1.08 ± 0.02	0.54 ± 0.0	1.22 ± 0.11
MCPL(ES)	580 (X450)	-1.8 ± 0.3	0.7 ± 0.08	0.35 ± 0.04	5.1 ± 0.4
		11 ± 0.6	0.22 ± 3	0.11 ± 1.5	17 ± 2
	640 (X532)	-1.4 ± 0.2	0.64 ± 0.07	0.32 ± 0.04	4.5 ± 0.3
		7.6 ± 0.5	0.28 ± 4	0.14 ± 2	21 ± 2.5
	830 (X375)	$(1.32 \pm 1) \times 10^{-2}$	2.19 ± 1.23	1.09 ± 0.62	6.9 ± 1.5
		1.26 ± 0.08	0.7 ± 10	0.35 ± 5	97 ± 6
	850 (X532)	-0.25 ± 0.9	0.15 ± 0.6	0.08 ± 0.3	2.1 ± 3.2
		-7.3 ± 0.7	0.22 ± 4.1	0.11 ± 2.05	25.5 ± 3
	1440 (X375)	-1.38 ± 0.06	2.14 ± 0.07	1.07 ± 0.04	6.18 ± 0.24

It was shown above that the saturation curves of the MCD have a form similar to that expected for the case of Kramers doublet. To clarify this point we compared the fits of MCD saturation at 465 nm in the assumption of the Kramers ($\Delta = 0\,\text{cm}^{-1}$) and non-Kramers ($\Delta \neq 0\,\text{cm}^{-1}$) doublets. The results of these two fits are shown in Fig. 6.14. It is seen that they are almost identical. It should be emphasized that this is not surprising and can happen in cases of a small value of the zero-field splitting energy. Nevertheless, the value of the function χ^2 (defines how well experimental data fits the model) is less for the case of the non-Kramers doublet. Moreover, it is seen from Table 6.1 that all the observed MCPL bands exhibit zero-field splitting. This reliably indicates that all emitting centres are the even-electron systems. For these reasons we assign the observed MCD to the transitions from the non-Kramers doublet of the ground state. The obtained value of the GS g-factor is very small. Summarizing these experimental results we assign all the Di bands, and the NIR PL at 1440 nm as well, to the defect in the glass network.

The modelling of the MCPL saturation curves have definitely revealed that the observed transition bands belong to centres with an even number of electrons or holes. One can notice the significant error in the obtained values of g-factors.
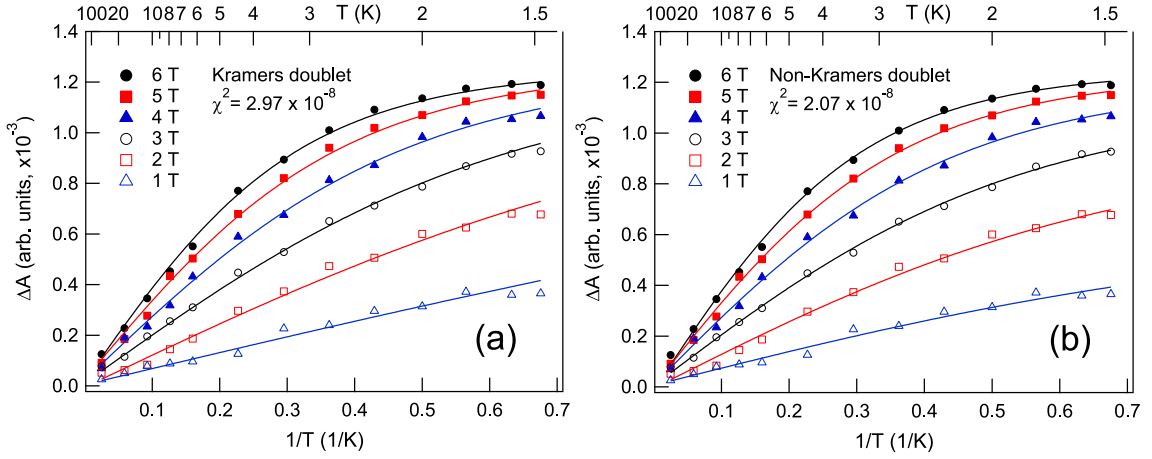
FIGURE 6.14: Comparison of saturation curves fits at 465 nm in the assumption of (a) Kramers and (b) non-Kramers doublets.

As it was explained in Chapter 5, this error appears because of the significant difference in the energies associated with the Zeeman and zero-field splittings. For example, the excited state, associated with the positive MCPL at 640 nm (PL4 band), has a relatively high value of the ZFS energy $\Delta = 21\,\text{cm}^{-1}$ and low contribution from Zeeman energy $\tilde{g}_\parallel \mu_B B = 1.7\,\text{cm}^{-1}$ at $B = 6$ T. On the contrary, when the Zeeman and ZFS energies are comparable the fit errors are small.

The analysis of the MCPL saturation curves at 580 and 640 nm confirmed the presence of two oppositely signed components. The negative shortwavelength component has low zero-field splitting energy comparing to the positive component. For this reason it was possible to distinguish them by measuring the MCPL spectrum at different temperatures. At low temperatures the spectral component with negative MCPL dominates. With an increase in temperature its polarization decays faster than that of the component with positive MCPL. The reason is clear from the comparison of ZFS: $\Delta^- \simeq 5$ and $\Delta^+ \simeq 20\,\text{cm}^{-1}$. As a result, the non-trivial temperature dependence of the MCPL signal with the maximum near 17 K was observed. The obtained values of g-factors and ZFS energies Δ under excitation at 450 and 532 nm are very close with the difference within the fit error. It is another confirmation that in both cases the excitation of the same states takes

place, though the luminescence band is slightly shifted.

The fit of MCPL saturation curves recorded at 830 nm under excitation at 375 nm (Fig. 6.13(b)) results in two components with positive polarization. Obviously, they correspond to the peaks 1 and 2 of Gaussian decomposition shown in Fig. 6.7. Unfortunately, these MCPL component cannot be distinguished by measuring the MCPL spectrum at different temperatures because they both have positive polarization. The strong component has very high ZFS energy $\Delta = 97\,\mathrm{cm}^{-1}$, while for the weak one we obtained $\Delta = 6.9\,\mathrm{cm}^{-1}$. The magnitude of the strong MCPL component is two orders higher than that of the weak one. For this reason the corresponding fit parameters are not so accurate.

6.3   MCD detected via luminescence

The detection of MCD via luminescence can directly prove that the NIR PL band is originated from the defect centre. In Chapter 5 we discussed in details the theoretical aspects of such an experiment. Briefly, the idea of the experiment is to detect the influence of the MCD on the NIR PL intensity. At low temperature the MCD can be regarded effectively as a modulation of the pump intensity. This effective modulation will cause the periodical changes of the luminescence intensity. In general, both diamagnetic $\mathscr{A}$ and paramagnetic $\mathscr{C}$ terms can affect the PL intensity. For this reason, it is necessary to record magnetic field dependences at different temperatures to distinguish the contributions from $\mathscr{A}$ and $\mathscr{C}$ terms.

The experimental setup was described in Chapter 5 (Fig. 5.11). In the present experiment we used the laser diode (1270 nm, LD-1270, Innolume GmbH) as an excitation source. The long wave pass filter was replaced by the bandpass one (FB1400-12, ThorLabs) with the centre wavelength at 1405 nm and full width at

half maximum $\Delta\lambda = 12$ nm. The quantity that we measure in the experiment is

$$\Delta I = \frac{I_{tot}(\sigma^+_{pump}) - I_{tot}(\sigma^-_{pump})}{I_{tot}(\sigma^+_{pump}) + I_{tot}(\sigma^-_{pump})}, \tag{6.1}$$

where $I_{tot}(\sigma^+_{pump})$ and $I_{tot}(\sigma^-_{pump})$ are the intensities of the PL under excitation by σ^+ and σ^- polarizations, respectively.

In Fig. 6.15 we show the spectrum of the NIR PL recorded under excitation at 1270 nm at T = 1.5 K. The band pass of the filter is relatively narrow, as a consequence, the spectrum replicates the transmission curve of the filter.
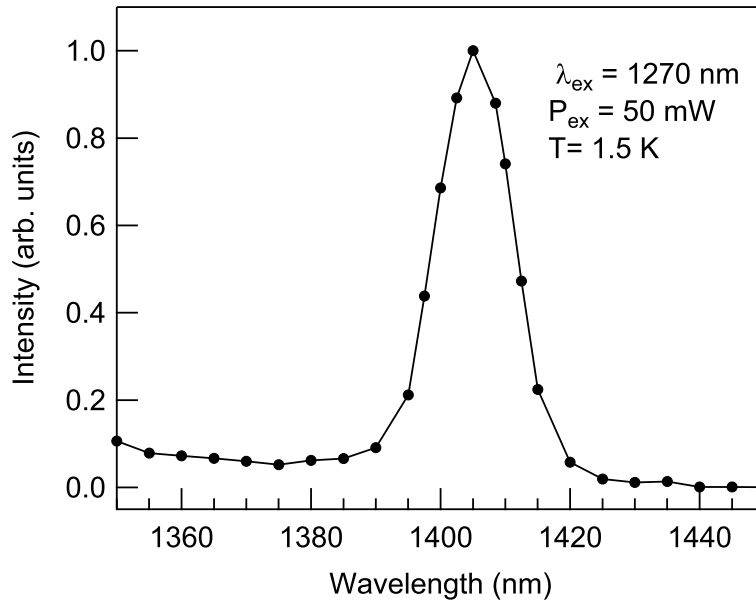
FIGURE 6.15: Spectrum of photoluminescence in Bi-doped silica glass under excitation at 1270 nm with the bandpass filter.

Magnetic field dependence of ΔI was recorded at the peak of PL intensity $\lambda_{det} = 1405$ nm and it is shown in Fig. 6.16. It is seen that even at the temperature T = 1.5 K the signal magnitude fluctuates near its zero value within the experimental error. At first glance, one can assume that the ground state is nondegenerated and the NIR PL cannot be assigned to the defect centre. However, the experiments on the MCPL definitely revealed the spin multiplicity of the excited state in the NIR transition. Therefore, we should be able to observe a signal
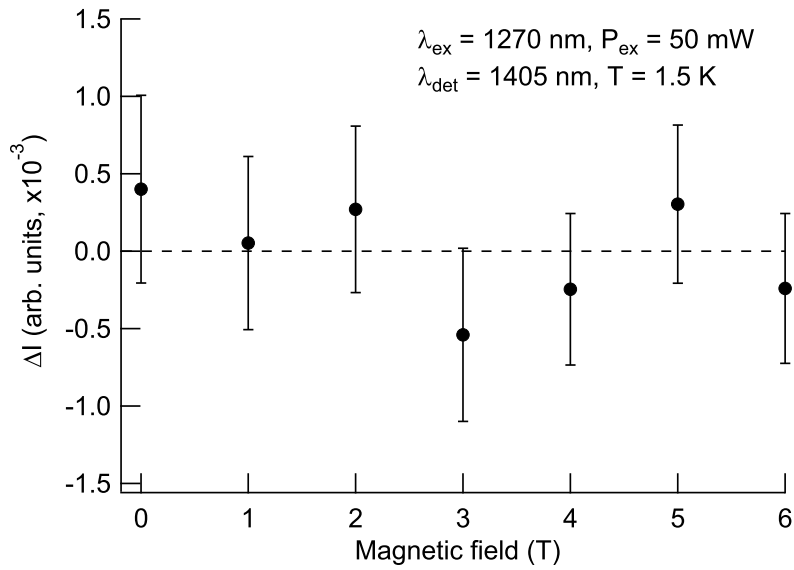
FIGURE 6.16: Magnetic field dependence of ΔI at 1405 nm and 1.5 K.

associated with the diamagnetic $\mathscr{A}$ term at least, which is field dependent. For this reason, we believe that the low doping level of the available sample and low absorption at 1270 nm are the main reasons for the negative result in this experiment.

6.4   Model of the luminescent centres

In previous sections we attributed the transition bands of the D and B series in the spectra to the transitions within the lattice defect and Bi^+ ion, respectively. Following the approach described in Chapter 5, we calculated the energy levels of Bi^+ ion in pure silica glass and tried to fit them to the positions of the bands in B series. In the frame of the ligand field theory the agreement of the calculated and experimental data was not satisfactory. We believe that the main reason of this failure is a rather strong interaction of Bi^+ ion with the environment, so that the crystal field approximation becomes inaccurate. Therefore, we still assign the bands B1, B2, B3 and B4 to the transitions $A_1\,(1\Sigma^+,{}^3P_0) \longrightarrow A_2\,(1\Sigma^-,{}^3P_1)$, $A_1\,(1\Sigma^+,{}^3P_0) \longrightarrow E\,(1\Pi,{}^3P_1)$, $A_1\,(1\Sigma^+,{}^3P_0) \longrightarrow E\,(2\Pi,{}^3P_2)$ and $A_1\,(1\Sigma^+,{}^3P_0) \longrightarrow$

A_1 ($3\Sigma^+$,$^1D_2$) in Bi^+ ion, respectively. In Chapter 5.4 we explained that in the case of Bi-doped aluminosilicate glass the transition A_1 ($1\Sigma^+$) $\longrightarrow$ A_2 ($1\Sigma^-$) is strictly forbidden in C_{3v} local symmetry, in which the state A_2 ($1\Sigma^-$) is pure. However, in Bi-doped sample investigated in the present Chapter the first excited state of Bi^+ ion A_2 ($1\Sigma^-$) is not pure due to the mixing with other states. Therefore, this transition occurs as a weak peak at 910 nm in the attenuation spectrum. The luminescence from this level was also observed previously in [75]. Narrow luminescence band PL2 observed under excitation at 375 nm consists of two transitions as it have revealed Gaussian multi-peak fit (Fig. 6.7) and analysis of MCPL saturation data recorded at 830 nm. In the frame of our model, these two components are caused by transitions 2Π $\longrightarrow$ 1Π and 1Π $\longrightarrow$ $1\Sigma^+$ in Bi^+ ion. Excited states 1Π and 2Π are degenerated ($M_J = \pm 1$), so both transitions exhibit magnetic circular polarization.

In Fig. 6.17 we show schematically the energy levels of the interacting defect centre and Bi^+ ion together with the MCD, excitation and attenuation spectra. The process of energy transfer is also shown. This model is close to that suggested for the Bi-doped aluminosilicate glass in Chapter 5. It is seen that this diagram allows to rationalize all the peculiarities in the spectra. The NIR PL occurs as a transition $|1\rangle \longrightarrow |0\rangle$ from the first excited state of the defect. This emission can be also observed under excitation into the excited states of Bi^+ ion due to the energy transfer process labelled as ET.

The weak absorption band D1 in the NIR region, shown in Fig. 6.1(b), indicates the forbidden character of the intracenter $|0\rangle \longrightarrow |1\rangle$ transition in the defect, which results in the millisecond lifetime in the first excited state. At the same time, as it was discussed in Chapter 5.4, the transition $|1\rangle \longrightarrow |2\rangle$ should be allowed. Therefore, the transition $|2\rangle \longrightarrow |1\rangle$ appears as a luminescence band PL3. Moreover, it is seen from Table 6.1 that the values of g-factor and ZFS Δ obtained from the measurements at 640 and 850 nm under excitation $\lambda_{exc} = 532$ nm are
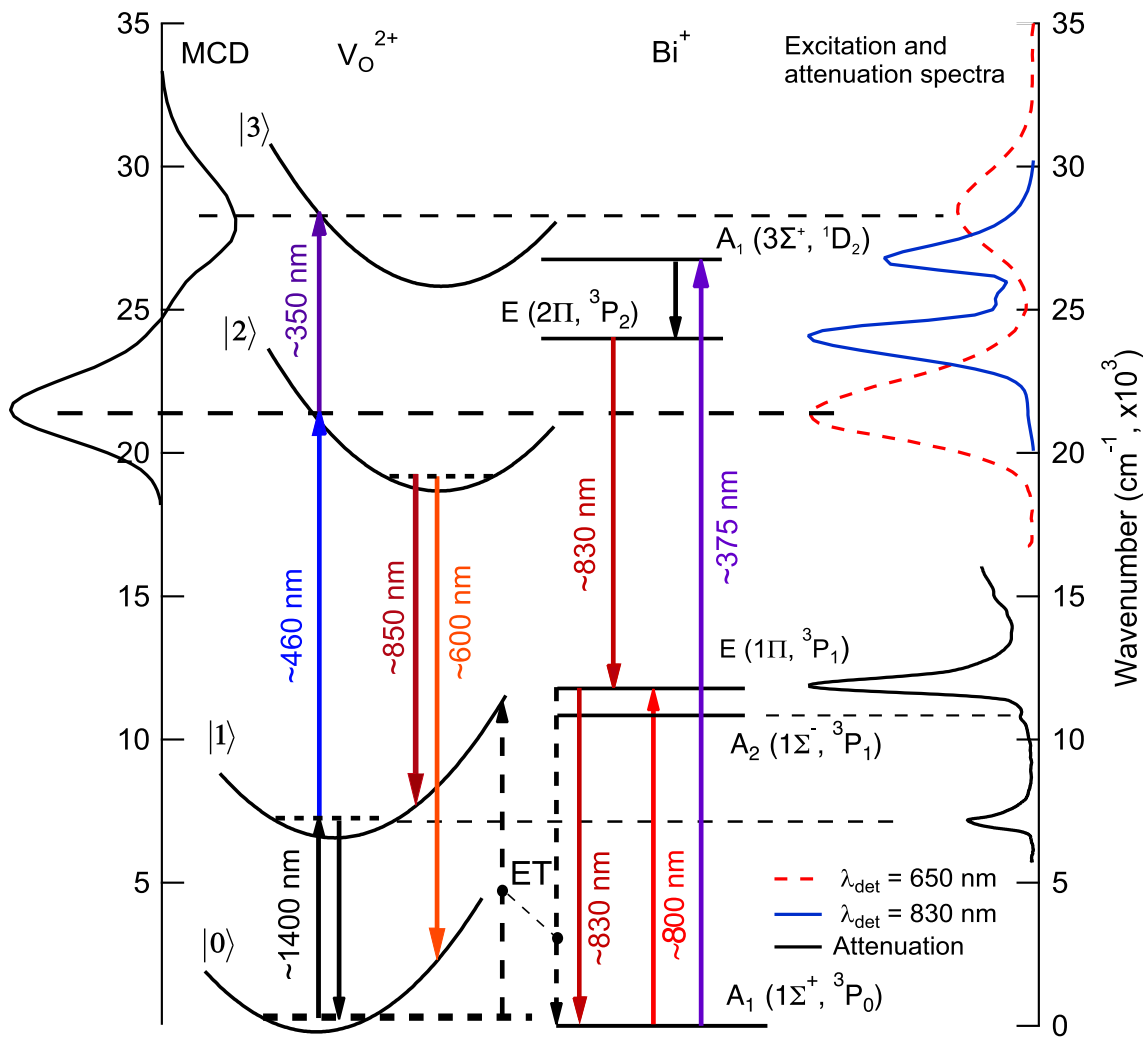
FIGURE 6.17: The model of the optically active centres with energy transfer process between them indicated by the dashed line. Pumping at ∼532 nm leads to the excitation of the defect. It is followed by intracenter luminescence to the states |1⟩ and |0⟩. Pumping at ∼800 nm and ∼375 nm leads to the direct excitation of Bi^+ ion. In the latter case the intracenter transitions precede the energy transfer to the defect.

close within the fit error. This clearly indicates that the luminescence bands PL3 and PL4 originate from the same excited state $|2\rangle$ of the defect centre.

It is worth noting that the PL4 band is much more intense than the band PL3. It indicates that the main channel of the relaxation from state $|2\rangle$ is the radiative transition to the ground state $|0\rangle$. As a consequence, population of the first ES $|1\rangle$ under excitation at $\lambda_{exc} \simeq 460\,$nm (D2 band) is low and NIR PL band is very weak. Moreover, the low intensity of the emission band PL2 (830 nm) under same excitation into the D2 band ($\simeq 460\,$nm) indicates that the energy transfer between the states $|2\rangle$ of defect and 2Π of Bi^+ ion is weak. For these reasons, the excitation spectrum of NIR PL1 band mainly consists of excitation bands of Bi^+ ion.

In Fig. 6.18 we show the simplest possible energy level diagram of the 'defect' centre, which is a counterpart of the model proposed for bismuth doped Mg-Al-Si glass in Chapter 5. This model successfully explains the unusual temperature dependence of the MCPL recorded at 580 and 640 nm (Fig. 6.12). In the frame of this model the ground $|0\rangle$ and $|2\rangle, |2'\rangle$ excited states are the spin triplets ($S = 1$) barring the first ES $|1\rangle$, which has the effective spin $S = 2$. The pump at 532 nm excites two relatively close-lying states $|2\rangle$ and $|2'\rangle$. Transitions $|0\rangle \longrightarrow |2, 2'\rangle$ can be observed as a band D2 in the MCD spectra with the maximum intensity near 460 nm. Two MCPL bands centred at 640 and 650 nm with different circular polarizations occur due to the transitions from the lowest spin sublevels $M_S = +1$ and $M_S = -1$ of the $|2\rangle$ and $|2'\rangle$ states, respectively, to the ground state $|0\rangle$. The MCPL selection rules are $\Delta M_S = M_f - M_i = -1$ for *lcp* and $\Delta M_S = +1$ for *rcp* light. Therefore, the σ^- component of the MCPL corresponds to the transition from the $M_S = +1$ sublevel of the high energy state $|2\rangle$ to the $M_S = 0$ sublevel of the ground state. The σ^+ MCPL component originates from the transition $|2'\rangle (M_S = -1) \longrightarrow |0\rangle (M_S = 0)$.

Transitions $|2'\rangle \longrightarrow |0\rangle$ (650 nm) and $|2'\rangle \longrightarrow |1\rangle$ (850 nm) have different circular polarizations. It is possible only if the final states $|1\rangle$ and $|0\rangle$ of these transitions
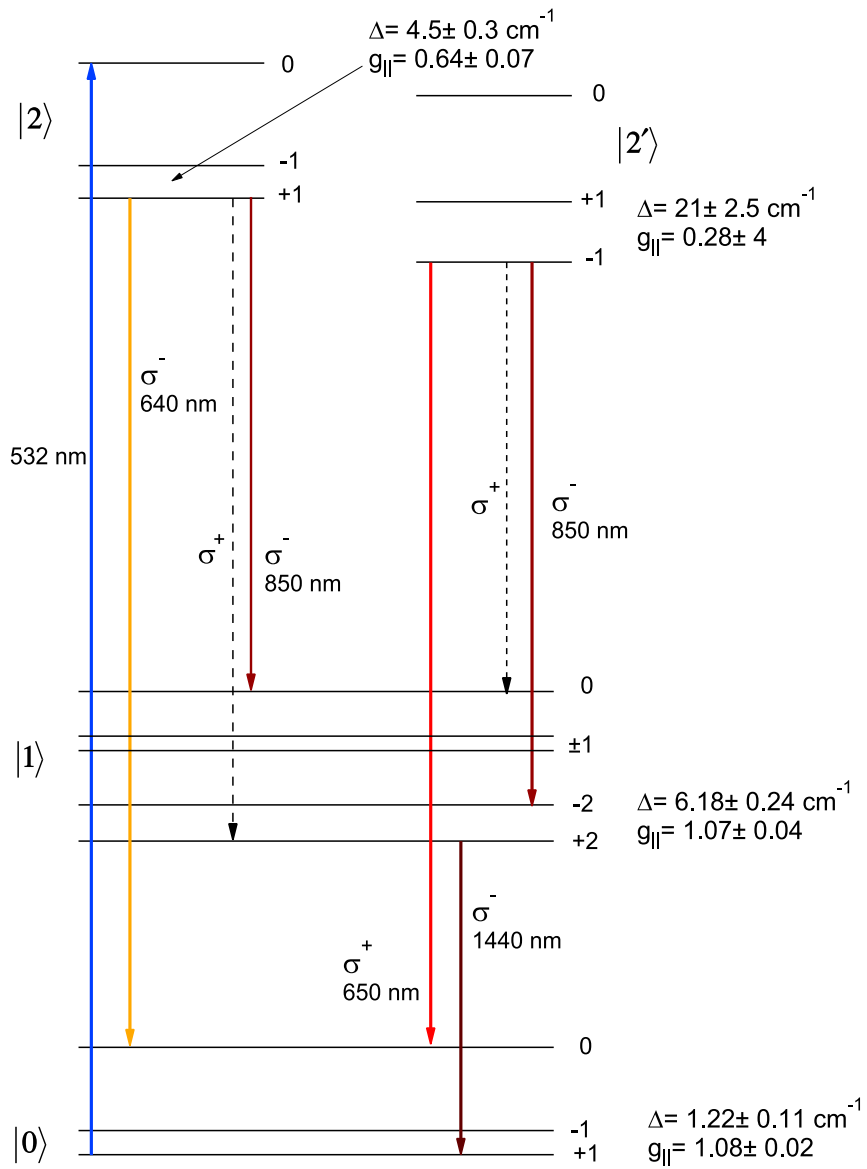
FIGURE 6.18: The energy level diagram to explain the origin of NIR and red luminescence.

have different effective spins. For this reason we assume that the first excited state of the defect centre is a spin quintet. According to our model at low temperature the MCPL at 850 nm should consist of four transitions: $|2, +1\rangle \longrightarrow |1, 0\rangle$, $|2, +1\rangle \longrightarrow |1, +2\rangle$, $|2', -1\rangle \longrightarrow |1, 0\rangle$ and $|2', -1\rangle \longrightarrow |1, -2\rangle$. The global fit of the saturation curves recorded at 850 nm under excitation wavelength $\lambda_{exc} = 532$ nm revealed that the main contribution to the degree of emission polarization is produced by the transition from the excited state with higher ZFS, e. g. $|2'\rangle$ state. Unfortunately, the detailed structure of the defect centre is unknown yet, thus we cannot estimate the transition probabilities. Nevertheless, taking into account the experimental results we assume that transitions $|2, +1\rangle \longrightarrow |1, +2\rangle$ and $|2', -1\rangle \longrightarrow |1, -2\rangle$ (dashed arrows in Fig. 6.18) are weak and they do not make observable contribution to the MCPL.

6.5 Conclusions

The detailed investigation of the Bismuth doped silica glass without other co-dopants was performed using the MCD and MCPL spectroscopies for the first time. Together with the methods of the conventional optical spectroscopy we demonstrated the coexistence of at least two optically active centres.

The analysis of the magnetic field and temperature dependences of the MCPL and MCD revealed that all the centres originate from the systems with an even number of electrons (holes). These centres were identified as Bi^+ ion and some defect in the glass network that interact due to the energy transfer process. The 'defect' centre has a degenerate ground state and it is responsible for the observed MCD signals.

The developed model of the optical centres satisfactorily explains the main peculiarities observed in the experiments. In the frame of this model the NIR PL is a forbidden transition from the first excited state of the 'defect' centre. Due to

the energy transfer this photoluminescence can be also observed under excitation into the excited states of the Bi^+ ion (375, 415, 800 nm). Also it was shown that the 'red' PL near 600 nm originates from the 'defect' centre due to the radiative transition from its second ES. Unfortunately, the low doping level of the sample did not allow us to detect the MCD via luminescence in the NIR spectral region.

Chapter 7

Optically detected magnetic resonance in a Bi-doped aluminosilicate glass

This Chapter describes the ODMR spectrometer operating in the microwave V band (58–62 GHz) and the results of ODMR experiments performed on the Bismuth doped aluminosilicate glass. In the ODMR experiment we detect the electron spin resonance by measuring the changes in the MCD or MCPL under resonance microwave radiation. It is clear that the ODMR signal is proportional to the MCD/MCPL intensity, thus bulk samples are desirable. On the other hand, large samples may significantly change the resonator parameters. Firstly, the introduction of a bulk sample shifts the resonance frequency. Secondly, the large samples dramatically impairs the coupling of the cavity to the waveguide. That is why the choice of the sample size is a compromise between the signal intensity and conservation of the cavity parameters. The bulk sample investigated in Chapter 5 was cut in two pieces and one of them was gradually ground off. We found that the optimal dimensions of the sample was $4 \times 1 \times 0.75$ mm. It does not shift the loaded resonator frequency out of the microwave generator operating limits and keeps the coupling at sufficient level.

In Chapter 5 we measured the energy of zero-field splitting and g-factor of the ground and excited states. It is seen from Table 5.1 that due to the high ZFS in the excited state the ODMR measurements in V band and at available MF 0–7 T are possible only in the ground state. For this reason, we performed the ODMR experiments only in absorption — so-called MCD 'tagged' by ESR [37].

One of the main purposes of the ODMR experiment is the measurement of the spin relaxation time. For such experiments the implementation of the photon-counting technique is strongly desirable. For this reason we decided to detect the ODMR in the ground state via luminescence. The
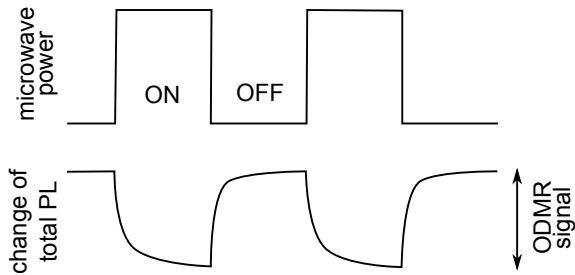
FIGURE 7.1: Evolution of ΔI under modulated microwave radiation.

idea of the experiment is based on the fact that the MCD influences the **total** intensity of the corresponding PL band (see details in Chapter 5.3 'MCD detected via luminescence'). The resonant microwave radiation leads to the equalization of populations within the spin sublevels of GS. As a result, the influence of MCD on the PL intensity (ΔI) decreases, as it is shown in Fig. 7.1. In this Chapter we demonstrate the possibility of the ODMR detection in MCD via luminescence. This is the first step toward the experiments on the spin relaxation time. We recorded the ODMR spectra at different values of the incident microwave power. Such experiments require the continuous sweep of the magnetic field. Hence, at this stage we used the phase-sensitive detection to record the spectra.

7.1 Microwave cavity

The microwave cavity is one of the substantial components of the spectrometer. It concentrates the microwave power and provides an oscillating magnetic field

B_1 with a component perpendicular to the static magnetic field **B**. Only this component of microwave field induces magnetic dipole transitions between Zeeman levels.
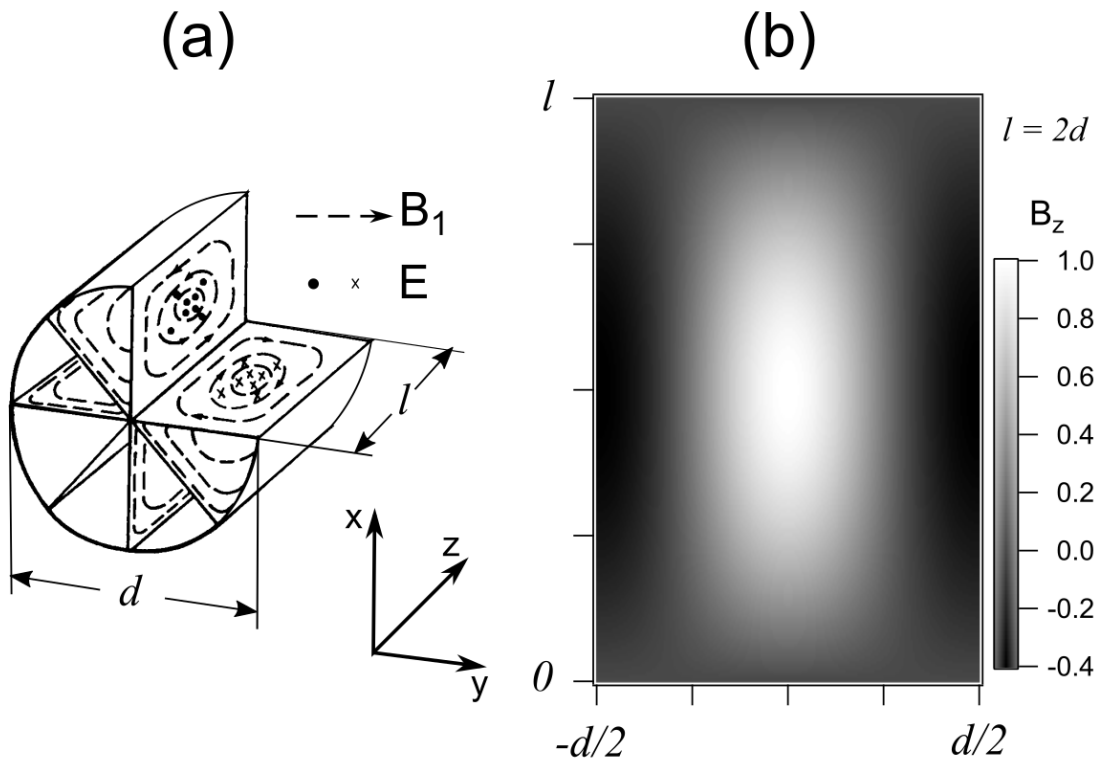
FIGURE 7.2: (a) Diagrammatic sketch of the TE_{011} cylindrical resonant cavity mode. Adapted from [77]. (b) Normalized intensity of z-component of the B_1 magnetic field. The static magnetic field B is applied in xy plane.

In general, in ODMR spectrometers the rectangular or cylindrical resonators are used. We decided to use a cylindrical design with the TE_{011} mode. Such a resonator has much higher quality factor Q comparing to a rectangular cavity [78]. The Q factor of cylindrical resonator depends on the diameter to length ratio d/l. The maximum value of Q can be achieved when the diameter is equal to the length of the resonator $d = l$, though the decrease of d/l leads only to the weak reduction of the quality factor. Fig. 7.2(a) schematically shows the distribution of electric and magnetic fields of the TE_{011} mode. In our experimental setup the external magnetic field B is applied in the xy plane. Therefore, the transitions between spin levels are induced by z-component (B_z) of the microwave field B_1.

Fig. 7.2(b) shows the intensity distribution of B_z in xz plane; it is invariant under rotation around z-axis. The maximum field strength can be achieved along the resonance axis. For this reason the sample should be placed at the centre of the cavity. It is worth noting that there is no rf current flow between the cylinder and end walls. Moreover, the electric current flows only in the angular direction since TE$_{011}$ mode has only angular component of the electric field. It allows to use the adjustable end wall (tuning plunger) for the frequency tuning. Also if there is a small gap between the piston edge and the wall other modes will be suppressed since they require the current flow across this gap. This useful trick helps to reduce the TM$_{111}$ mode that is degenerated by the TE$_{011}$ mode. Therefore, such a cylindrical cavity with the TE$_{011}$ mode is considered as the best option for the ODMR experiments. Another advantage of a cylindrical resonator is the relatively simple fabrication. The cavity interior is a hollow cylinder and it can be easily turned from a bulk work piece. Usually, the inner surface is silver or gold plated to improve the conductivity and quality factor Q.

In ODMR experiments the strongest signal is obtained when the magnetic dipole transitions between spin levels are saturated. In order to fulfil this condition the resonant cavity must be coupled to the waveguide so that the reflected power is minimal. Usually it is done by means of an iris. The diaphragm is located at the point with the maximum of magnetic field in the waveguide. The maximum coupling to the cavity can

FIGURE 7.3: End plate method of coupling to the TE$_{011}$ mode in a cylindrical resonator.

be obtained if the iris is also placed at the point where the magnetic field in the resonator is oriented in the same direction as the field in the waveguide. In our cryostat, due to the limited inner space, the resonator can be placed only vertically and the coupling to the waveguide is performed through the iris in the upper wall, as it is shown in Fig. 7.3. The waveguide axis is shifted from the resonator axis where the radial component of B_1 is minimal. In this coupling method the B_1 vector at the cavity side can be regarded as a natural continuation of the MF vector at the waveguide side of the diaphragm. The maximal value of the microwave field B_z (in units of G) in the centre of cavity can be calculated by the following equation [78]:

$$B_z^2 = 24.66 \times 10^{-3} P_w Q_L \frac{V_w}{V_c}, \tag{7.1}$$

where P_w is the incident power in mW, Q_L is the loaded Q factor, V_w and V_c are the volume of a section of waveguide one guide wavelength long and the cavity volume, respectively. It is seen that the straightforward way to increase the magnetic field in the cavity is to increase of the source power. However, in the case of helium cryostat it can cause the increase of temperature. The situation is even worst for a closed loop cryostat like one used in our setup. For this reason, the only possible approach is to improve the resonator quality.

In our experimental setup we use the cylindrical cavity with diameter $d = 0.6$ cm. The bottom wall is adjustable (a tuning plunger) which allows the frequency tuning by changing the cavity length in the range 0.5–1.6 cm. The resonator was fabricated from the beryllium bronze and its inner surface was silver plated. Two coaxial apertures for optical access were drilled at 2.5 mm below the upper plate. A set of irises with different diameters was fabricated. We found that the optimal diameter of the iris for our resonator was 1.2 mm. This diaphragm provides good coupling and does not decrease quality factor Q.
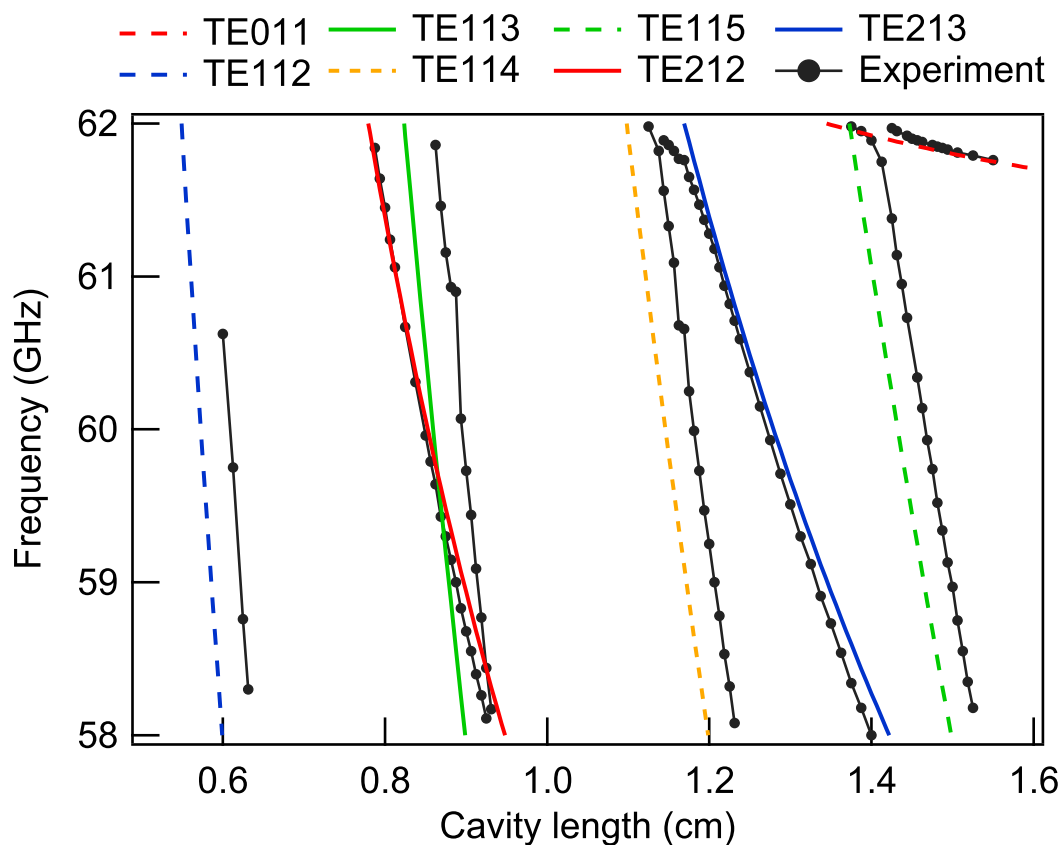
FIGURE 7.4: Calculated (lines) and measured (dots) mode frequencies as a function of the cavity length l in air at T = 300 K.

The frequency of the TE$_{mnp}$ mode in a cylindrical resonant cavity with no apertures in the walls can be calculated using the following equation [78, 79]:

$$f_{mnp} = \frac{1}{d}\sqrt{\left(\frac{cx_{mn}}{\pi}\right)^2 + \left(\frac{cp}{2}\right)^2 \left(\frac{d}{l}\right)^2}, \tag{7.2}$$

where $(x)_{mn}$ is the n-th root of the first derivative of the m-order Bessel function $J_m(k_c r)$, c is the speed of light in the medium inside the resonator. In Fig. 7.4 we show the calculated and measured mode frequencies as a function of the cavity length. The observed modes where identified as TE$_{112}$, TE$_{212}$, TE$_{113}$, TE$_{114}$, TE$_{213}$, TE$_{115}$ and TE$_{011}$. It is seen that the measured frequencies of TE$_{11p}$ modes are shifted relative to the theoretical ones. This type of modes are affected by the strong influence of the apertures due to the particular field distribution.
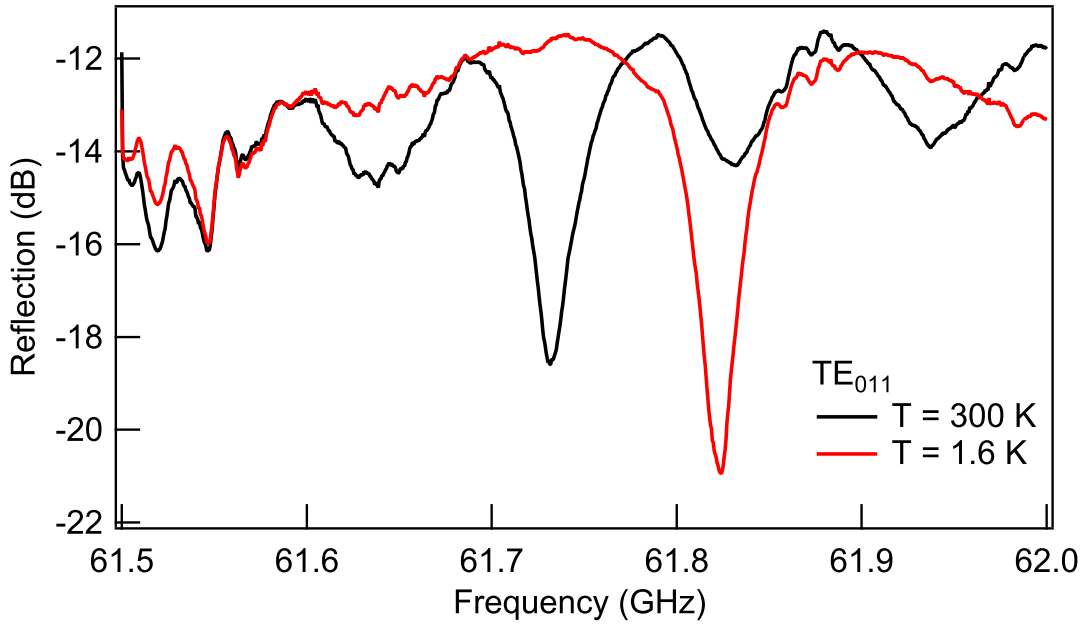
FIGURE 7.5: Resonance curves of TE_{011} mode at T = 300 and 1.6 K.

In Fig. 7.5 we show the measured resonance curve of the TE_{011} mode at room temperature and T = 1.6 K with the sample of Bi-doped aluminosilicate glass attached to the top plate of the cavity. The average reflection base level about -13 dB indicates that the power loss in the waveguide section is 6.5 dB. At T = 300 K we measured the full width at half maximum $\Delta f = 25$ MHz which corresponds to the loaded quality factor $Q = 2500$. Because of the thermal expansion the inner volume of the cavity decreases with decreasing temperature. For this reason at T = 1.6 K the resonance curve is shifted by $\simeq 100$ MHz to higher frequencies. Also, the resonance is slightly narrowed so that the loaded quality factor becomes higher $Q \simeq 3000$. Substituting the numeric values Eq. 7.1 can be simplified so that $B_z \simeq 3\sqrt{P_w}$ G. The output power of our microwave source at 61.8 GHz is about 40 mW. Taking into account the 6.5 dB losses in the waveguide section, the incident power should be about $P_w \simeq 10$ mW. Thus, the magnetic field in the centre of cavity can be estimated as $B_z = 9.5$ G.

7.2 ODMR spectrometer
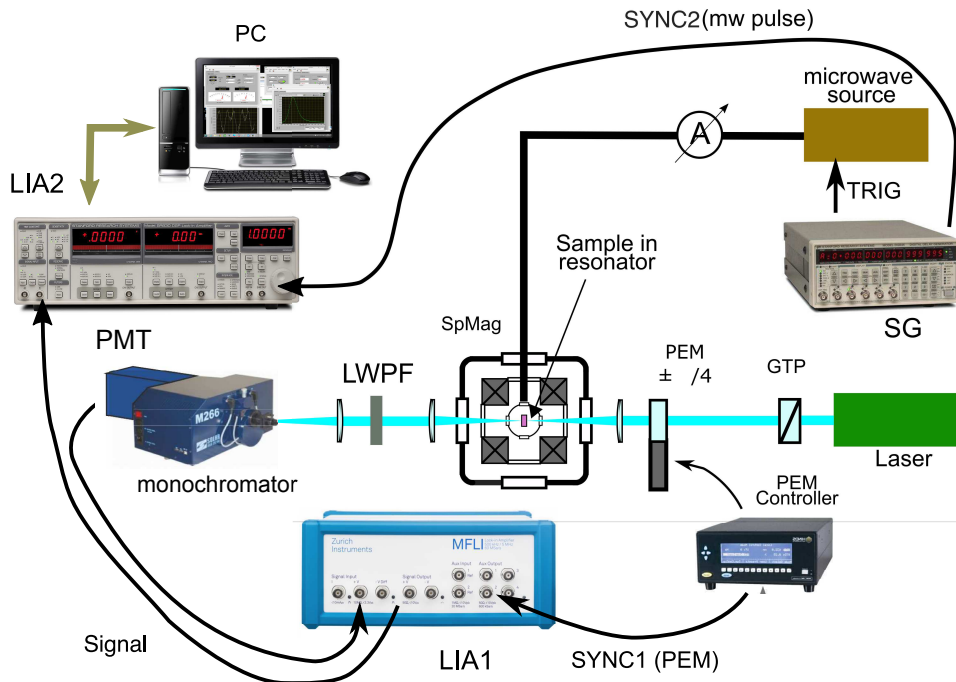
FIGURE 7.6: Experimental setup for ODMR measurements. GTP – Glan-Thompson polarizer, PEM – photoelastic modulator, SpMag – cryomagnetic system, LWPF – long wave pass filter, PMT – photomultiplier, SG – signal generator, LIA1, LIA2 – lock-in amplifiers, A – variable MW attenuator.

The experimental setup for the optical detection of magnetic resonance is shown in Fig. 7.6. The beam of the pump laser (532 nm) is polarized vertically by the Glan-Thompson polarizer (GTP) and it propagates along the external magnetic field **B**. The photoelastic modulator (PEM) with its birefringent axis oriented at 45° to the polarization plane of light periodically transforms it to the σ^+/σ^- polarized light at the frequency $f_{PEM} = 20$ KHz (see Chapter 4 for details). Then the polarization modulated light is focused on the sample placed in the microwave resonator. The collimated beam of the PL emission passes through the long wave pass filter (LWPF) and is focused on the entrance slit of the monochromator coupled to the GaAs photomultiplier (R943-02, Hamamatsu Inc.). The signal generator (DG645, Stanford Research Systems) generates two TTL signals at the frequency $f_{mw}^{mod} \ll f_{PEM}$. These pulses are used as reference signals for the

microwave source (G4-60/1E, Elmika Inc.) and second lock-in amplifier (SR830, Stanford Research Systems). The photocurrent of photomultiplier is converted to the voltage by the current to voltage amplifier (C7319, Hamamatsu Inc.) In this experimental arrangement, the signal from PMT is doubly modulated. At the first stage the signal is demodulated at the frequency f_{PEM} and it is proportional to the MCD intensity. Then it is demodulated at the low frequency f_{mw}^{mod} by the second LIA. The microwave power is guided by the 'nickel silver' waveguide that significantly lowers the hit flow to the measuring section.

The quantity we measure in the experiment is

$$\Delta\rho = \frac{\Delta I^0 - \Delta I^{mw}}{\Delta I^0 + \Delta I^{mw}} \tag{7.3}$$

$$\Delta I = I_{tot}(\sigma_{pump}^+) - I_{tot}(\sigma_{pump}^-), \tag{7.4}$$

where ΔI^0 and ΔI^{mw} stand for ΔI in the absence and presence of the microwave radiation, respectively; $I_{tot}(\sigma_{pump}^+)$ and $I_{tot}(\sigma_{pump}^-)$ are the intensities of the PL under excitation by σ^+ and σ^- polarizations, respectively.

7.3 ODMR spectra

In Chapter 5 we have shown that the defect centre responsible for the NIR PL has a strong MCD band at 500 nm (Fig. 5.1). The radiation emission from this level to the ground state is observed as a luminescence band at 700 nm shown in Fig. 5.3. We used this photoluminescence to record the ODMR spectra, namely the magnetic field dependences of the quantity $\Delta\rho$ in Eq. 7.4. From the MCD saturation measurements we obtained $g_\parallel = 0.9\pm0.03$ and $\Delta = 1.36\pm0.13\,\mathrm{cm}^{-1}$ for the ground state (Table 5.1). The energy gap between the sublevels of $M_S = \pm1$ doublet of the ground state is given by Eq. 3.6. According to this equation the electron spin resonance should occur at the magnitude of the external magnetic
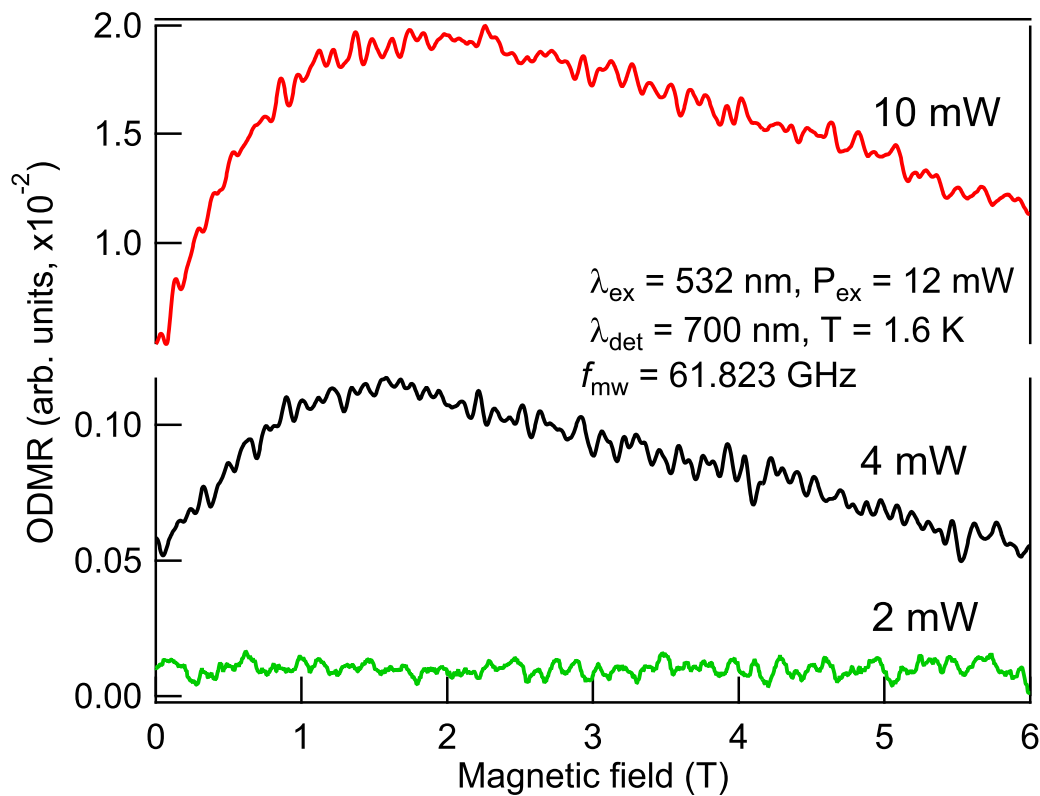
FIGURE 7.7: ODMR spectra measured at T = 1.6 K and different microwave power attenuations.

field $B_0 = 1.83 \pm 0.14$ T when the cavity is tuned to $f_{mw} = 61.823$ GHz. The ODMR spectra recorded at several values of the microwave power are shown in Fig. 7.7. The resonance curves are extremely wide and exhibit non-symmetric form, which is not surprising for glasses. For example, in the ODMR experiments on rare-earth-doped glasses performed in [80–83] authors recorded very broad ODMR spectra using a technique based of the Faraday effect (Fig. 7.8).

The measured resonance magnetic field $B_0 = 1.87$ T, at the microwave source power $P = 10$ mW, is in good agreement with the predicted value based on the MCD experiments. However, at higher attenuation level it is shifted to lower MF's so that $B_0 = 1.6$ T. The increase of the microwave power level leads to the signal increase. We measured $\Delta \rho = 1.96 \times 10^{-2}$ at B = 1.87 T and A = 6 dB. This indicates that the relative change of MCD induced by the microwave radiation
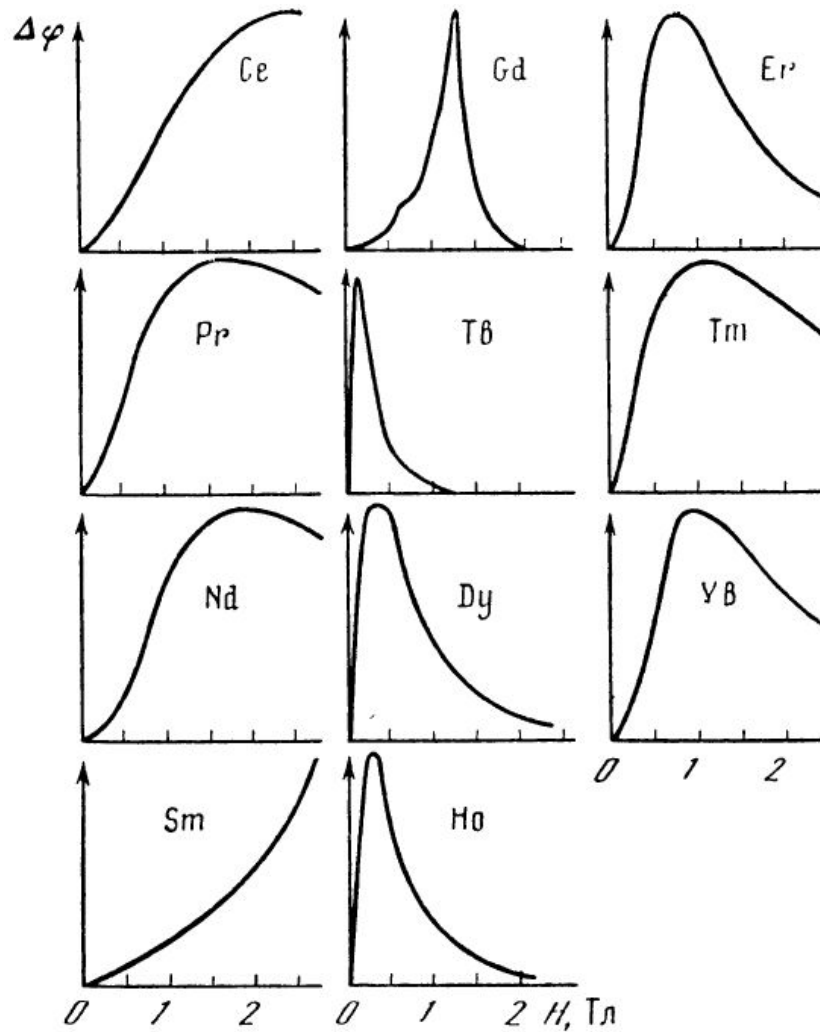
FIGURE 7.8: Examples of recorded ODMR spectra using a technique based on the Faraday effect in glasses doped by different ions. Magnetic field is given in units of T. After [81]

is less than 2%. It is clear that there is no saturation of the transitions between spin sublevels of the GS. The subsequent increase of the MW power leads to the temperature increase of the sample.

There are two important remarks concerning the recorded ODMR spectra: they have *(a)* well-pronounced background signal that does not depend on the MF and *(b)* non-zero signal at low magnetic fields. Both effects are considered as a result of the microwave electric field absorption and they should not be associated with the defect or impurity centres [83, 84]. Since these undesirable signals

are of non-magnetic origin, they can be directly eliminated by the modulation of magnetic field. The double field modulation approach is the most useful. In this method the magnetic field is amplitude modulated at high frequency (10–100 KHz), then it is 'chopped' at low frequency (0.1–1 KHz). The ODMR signal is obtained by the demodulation at the low frequency. Such a technique was implemented in [83]. Authors compared two ODMR spectra recorded under modulation of the microwave power and magnetic field. They found that the main difference was the absence of the ODMR signal at low MF's in the spectrum recorded using the second technique.

7.4 Conclusions

The ODMR spectrometer for the microwave V-band (58–62 GHz) was created built on the basis of the helium closed-cycle magneto-optical cryostat. This spectrometer allows to perform the ODMR experiments in the UV–NIR spectral range, namely 350–1600 nm, in magnetic fields up to 7 T and in the temperature range 1.6–300 K. We showed that the ODMR in the ground state can be detected via luminescence. The next step toward the experiments on the investigation of spin relaxation processes is the implementation of the photon-counting technique instead of the phase- sensitive detection.

The ODMR spectra in Bi-doped Mg-Al-Si oxide glass were measured at different levels of the incident microwave power. The spectra are very wide, which is the usual case of doped glasses.

Chapter 8

Conclusions and Prospects

8.1 Conclusions

Magneto-optical methods of spectroscopy are very powerful instruments for the investigation of condensed matter. Advanced spectroscopical techniques, such as MCD and MCPL, allow performing qualitative and quantitative investigations of paramagnetic centres. These non-resonant methods are widespread due to the relative technical simplicity and the variety of information that can be obtained.

We developed the experimental setup for MCD and MCPL measurements that cover UV to NIR spectral range, namely 350–1600 nm, in magnetic fields up to 7 T and at temperatures 1.4–300 K. On the basis of this setup the ODMR spectrometer operating at the microwave V-band (58–62 GHz) was also built.

For the first time, Bi-doped silica glasses were studied using the MCD and MCPL spectroscopies. We have shown experimentally that all optically active centres in Bismuth-doped Mg-Al-Si oxide glass and Bismuth-doped silica glass without other co-dopants originate from the systems with even number of electrons or holes. This indicates that systems with unpaired electrons, such as BiO molecules, Bi^0 atoms, Bi_2^- dimers, cannot be responsible for the NIR photoluminescence.

Our experimental results revealed that both investigated samples have two

centres — one with a degenerate and another with a non-degenerate ground states. An additional type of centres associated with the clusters of Bi ions was observed in the aluminosilicate sample due to the high doping level. The experiments on a detection of the MCD via luminescence definitely proves that the ground state of the centre associated with the NIR photoluminescence is a spin multiplet. Therefore, Bi^{5+} and Bi^+ ions cannot be considered as an origin of this luminescence, as it was suggested in many anterior works, for example in [18, 68]. Also this indicates that, in general, the ESR signal can be detected. However, all the ESR experiments in Bismuth-doped glasses were performed using the conventional spectrometers operating in the microwave X-band (9.8 GHz). It is seen from Table 5.1 and Table 6.1 that this microwave frequency is too low to match the ZFS ($\simeq$40 GHz). Another complication consists in the extremely large width of the resonance lines. As a consequence, the amplitude of the ESR signal is below the sensitivity of the spectrometer. In such conditions, the optical detection of the magnetic resonance should be implemented.

We suggested a model of Bi^+ ion and some defect centre in the glass network interacting through the energy transfer processes. In the frame of this model, the near-infrared photoluminescence is a forbidden transition from the first excited state of the defect centre. Point defects or localized states caused by the presence of *6p* (Bi, Pb) and *5p* (Sn, Sb) ions were considered as an origin of the NIR PL for the first time by Sharonov et al. [28, 55]. Authors also emphasized that the main absorption and emission bands can originate from different optical centres. Recently, Dianov et al. [31, 32] proposed a model where Bi^{2+} ion and oxygen deficiency centre ODC (II) form a single molecular unit. According to the model, this centre is an even-electron system with the total angular momentum $J = 1/2$ in the ground state. Obviously, this model contradicts our experimental results obtained from the MCD and MCPL studies.

Usually, the so-called 'red' luminescence with the peak intensity at 650 and

700 nm in the Bi-doped silica and aluminosilicate glasses, respectively, is assigned to Bi^{2+} ion [20, 44, 68, 76]. We have shown experimentally that it cannot be Bi^{2+} ion, since it has one unpaired electron and the ground state $^2P_{1/2}$ is a Kramers doublet. In the frame of our model this luminescence appears as a radiative transition from the second excited state of the defect centre.

We have demonstrated the possibility of the ODMR detection in the ground state via luminescence. The implementation of the photon-counting technique will allow us to study the spin relaxation processes. Particularly, the investigation of the temperature and field dependences of the spin relaxation time T provides useful information about the spin-lattice relaxation mechanisms.

8.2 Prospects

The main achievement of this thesis is that we have directly connected the MCD active defect centre with the NIR PL. However, the exact nature of this defect remains unclear. In our opinion, the most probable route of the formation of optically active defect is the transfer of two electrons from the oxygen vacancy to Bi^{3+} ion, thus forming a positively charged oxygen vacancy V_O^{2+} and Bi^+ ion in its environment. Obviously, the further studies have to be devoted to the investigation of the microscopical structure of the defect and the mechanisms of its formation. Usually, this problem is solved by means of the ESR based techniques. Unfortunately, in Bi-doped oxide glasses the conventional ESR methods are not applicable due to the extremely large width of the resonance line.

The range of measurable spin relaxation times T_1 in our ODMR spectrometer is limited by the switching rate of the light polarization, i.e. by the PEM frequency, so that the minimal T_1 that can be measured is around $50\,\mu$s. The straightforward solution is the usage of a high speed modulator. However, the recent development of the high speed acquisition electronic devices allows the

implementation of so-called spin noise spectroscopy (SNS), that also removes this limitation.

In the spin noise spectroscopy we deal with the fluctuation of spins at thermal equilibrium. In general, the fluctuation-dissipation theorem [85, 86] gives the relationship between the response of the system to a small perturbation and its thermal equilibrium fluctuation. In application to the magnetic medium this theorem states that the Fourier transform of the correlation function of magnetic moments is proportional to the imaginary part of the susceptibility. In other words, the fluctuation of spins carries an information about the dynamics of the spin system.
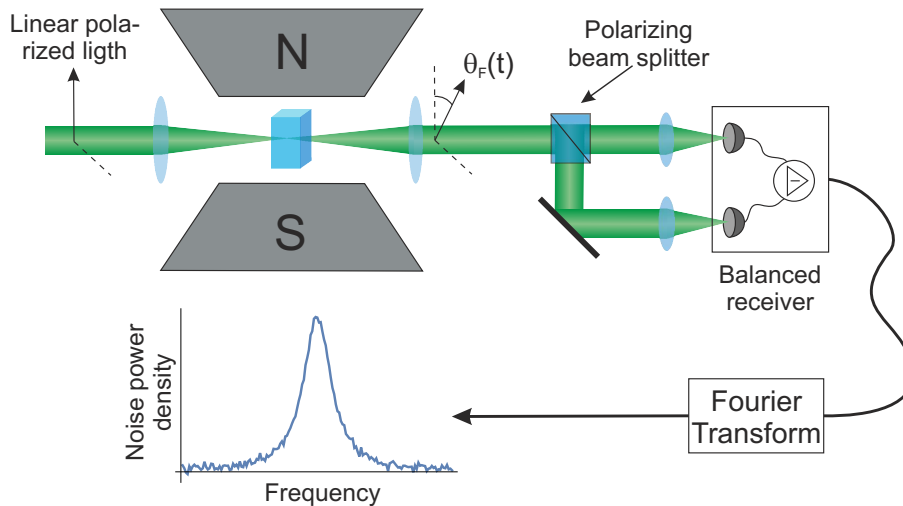
FIGURE 8.1: Basic experimental setup for SNS in the Faraday rotation

In Fig. 8.1 we show the basic experimental principles of the spin noise spectrometer based on the Faraday effect. The linearly polarized light propagates through the sample placed in the magnetic field. Due to the Faraday effect the spin noise is transformed to the fluctuations of the Faraday rotation angle $\theta_F(t)$. The noise power spectrum is obtained by the Fourier transform of the signal from a balanced photoreceiver. The peak position of the spectrum yields the Larmor frequency, the width of the curve is inversely proportional to the transverse spin relaxation time T_2 and the area under the curve is proportional to the spin noise

power. The main technical problem in the conventional SNS is the relatively low bandwidth of the balanced detectors — the commercially available models operate below several GHz making such an approach suitable for the investigations of effective Kramers doublets with relatively long spin dephasing times (ns-μs region). However, in Bismuth-doped oxide glasses the strong crystal field creates large zero-field splitting, so even in low magnetic fields the Larmor frequency is much higher than the receiver's bandwidth. Fortunately, there are several advanced experimental techniques that extend the frequency range to the THz region.

Another promising area of research is the study of the MCD/MCPL dependence on the Bismuth doping level of samples. Such experiments can provide some additional information on the defect formation processes.

Appendix A

Transition bands in Bi-doped Mg-Al-Si glass

Band	WL (nm)	E (cm^{-1})	Observed in
B1	700	14285	A, X
B1'*	780	12820	
B2	626	15974	X
B3	441	22727	X
B4	340	29412	X
D1	1030	9709	X, M*
D2	500	20000	A, X, M
D3	375	26667	M
C1	1400–1500	6667–7143	M
C2	900–920	10870–11111	M

A — absorption spectrum

X — excitation spectrum

M — MCD spectrum

M* — MCD observed via luminescence

B1'* — observed in the anti-Stokes PL in Ga/Bi co-doped silica glass

Appendix B

Matrix elements between Russell-Saunders states of p^2 electron configuration in the crystal field of C_2 symmetry.

The energy of electronic states of Bi^+ ion were calculated by the numerical diagonalization of the Hamiltonian matrix with elements collected in Table B.1. The diagonalization was performed using the Wolfram Mathematica software with the built-in functions 'Eigensystem' and 'Eigenvalues'.

116

Appendix B. Matrix elements between Russell-Saunders states of p^2 electron configuration in the crystal field of C_2 symmetry.

TABLE B.1: Non-zero matrix elements between Russell-Saunders states $|SLJM_J\rangle$ of p^2 electron configuration in the crystal field of C_2 symmetry. F_2 is the Slater electron-repulsion integral, λ is the spin-orbit coupling constant, $x = B_0^2/10$ and $y = B_2^2/(5\sqrt{2})$.

	$\langle0000\|$	$\langle022\bar{2}\|$	$\langle02\bar{2}\bar{1}\|$	$\langle0220\|$	$\langle0221\|$	$\langle0222\|$	$\langle11\bar{2}\bar{2}\|$	$\langle11\bar{2}\bar{1}\|$	$\langle11\bar{2}0\|$	$\langle11\bar{2}1\|$	$\langle11\bar{2}2\|$	$\langle11\bar{1}\bar{1}\|$	$\langle11\bar{1}0\|$	$\langle11\bar{1}1\|$	$\langle1100\|$
$|0000\rangle$	$10F_2$	$-4y$	·	$-4\sqrt{2}x$	·	$-4y$	·	·	·	·	·	·	·	·	$-2\sqrt{2}\lambda$
$|022\bar{2}\rangle$	$-4y$	F_2-4x	·	$-2\sqrt{2}y$	·	·	$\sqrt{2}\lambda$	·	·	·	·	·	·	·	·
$|02\bar{2}\bar{1}\rangle$	·	·	F_2+2x	·	$-2\sqrt{3}y$	·	·	$\sqrt{2}\lambda$	·	·	·	·	·	·	·
$|0220\rangle$	$-4\sqrt{2}x$	$-2\sqrt{2}y$	·	F_2+4x	·	$-2\sqrt{2}y$	·	·	$\sqrt{2}\lambda$	·	·	·	·	·	·
$|0221\rangle$	·	·	$-2\sqrt{3}y$	·	F_2+2x	·	·	·	·	$\sqrt{2}\lambda$	·	·	·	·	·
$|0222\rangle$	$-4y$	·	·	$-2\sqrt{2}y$	·	F_2-4x	·	·	·	·	$\sqrt{2}\lambda$	·	·	·	·
$|11\bar{2}\bar{2}\rangle$	·	$\sqrt{2}\lambda$	·	·	·	·	$-5F_2+\lambda+2x$	·	$\sqrt{2}y$	·	·	·	$\sqrt{6}y$	·	$2y$
$|11\bar{2}\bar{1}\rangle$	·	·	$\sqrt{2}\lambda$	·	·	·	·	$-5F_2+\lambda-x$	·	$\sqrt{2}y$	·	$-3x$	·	$\sqrt{3}y$	·
$|11\bar{2}0\rangle$	·	·	·	$\sqrt{2}\lambda$	·	·	$\sqrt{2}y$	·	$-5F_2+\lambda-2x$	·	$\sqrt{2}y$	·	·	·	$2\sqrt{2}x$
$|11\bar{2}1\rangle$	·	·	·	·	$\sqrt{2}\lambda$	·	·	$\sqrt{2}y$	·	$-5F_2+\lambda-x$	·	$-\sqrt{3}y$	·	$3x$	·
$|11\bar{2}2\rangle$	·	·	·	·	·	$\sqrt{2}\lambda$	·	·	$\sqrt{2}y$	·	$-5F_2+\lambda+2x$	·	$-\sqrt{6}y$	·	$2y$
$|11\bar{1}\bar{1}\rangle$	·	·	·	·	·	·	·	$-3x$	·	$-\sqrt{3}y$	·	$-5F_2-\lambda-x$	·	$-y$	·
$|11\bar{1}0\rangle$	·	·	·	·	·	·	$\sqrt{6}y$	·	·	·	$-\sqrt{6}y$	·	$-5F_2-\lambda+2x$	·	·
$|11\bar{1}1\rangle$	·	·	·	·	·	·	·	$\sqrt{3}y$	·	$3x$	·	$-y$	·	$-5F_2-\lambda-x$	·
$|1100\rangle$	$-2\sqrt{2}\lambda$	·	·	·	·	·	$2y$	·	$2\sqrt{2}x$	·	$2y$	·	·	·	$-5F_2-2\lambda$

Appendix B. Matrix elements between Russell-Saunders states of p^2 electron configuration in the crystal field of C_2 symmetry.

117

TABLE B.2: The ligand field states of Bi$^+$ ion as linear combinations of Russell-Saunders states $|i\rangle = \sum_j a_j\,|SLJM_J\rangle$.

$$F_2 = 1135\,\text{cm}^{-1},\ \lambda = 5312\,\text{cm}^{-1},\ B_0^2 = -26920\,\text{cm}^{-1},\ B_2^2 = 180\,\text{cm}^{-1}.$$

$$a_j^2$$

$|i\rangle$	$|0000\rangle$	$|022\bar{2}\rangle$	$|022\bar{1}\rangle$	$|0220\rangle$	$|0221\rangle$	$|0222\rangle$	$|112\bar{2}\rangle$	$|112\bar{1}\rangle$	$|1120\rangle$	$|1121\rangle$	$|1122\rangle$	$|111\bar{1}\rangle$	$|1110\rangle$	$|1111\rangle$	$|1100\rangle$
A$_1$ (^{3}P$_0$)	0.2	10^{-7}	0	0.217	0	10^{-7}	10^{-6}	0	0.071	0	10^{-6}	0	0	0	0.51
A$_2$ (^{3}P$_1$, $M_J=0$)	0	10^{-6}	0	0	0	10^{-6}	10^{-4}	0	0	0	10^{-4}	0	$\sim$1	0	0
E (^{3}P$_1$, $M_J=\pm1$)	0	0	0.081	0	0.081	0	0	0.147	0	0.147	0	0.272	0	0.272	0
A$_1$ (^{3}P$_2$, $M_J=0$)	0.019	0	0	0.611	0	0	0	0	0	0	0	0	0	0	0.37
E (^{3}P$_2$, $M_J=\pm2$)	10^{-7}	0.06	0	10^{-4}	0	0.06	0.44	0	10^{-6}	0	0.44	0	10^{-4}	0	10^{-4}
E (^{3}P$_2$, $M_J=\pm1$)	0	0	0.32	0	0.32	0	0	0.015	0	0.015	0	0.165	0	0.165	0
A$_1$ (^{1}D$_2$, $M_J=0$)	0.144	10^{-5}	0	0.0053	0	10^{-5}	10^{-7}	0	0.847	0	10^{-7}	0	0	0	0.003
E (^{1}D$_2$, $M_J=\pm1$)	0	0	0.095	0	0.095	0	0	0.339	0	0.339	0	0.066	0	0.066	0
E (^{1}D$_2$, $M_J=\pm2$)	10^{-4}	0.44	0	10^{-4}	0	0.44	0.06	0	10^{-4}	0	0.06	0	10^{-6}	0	10^{-5}
A$_1$ (^{1}S$_0$)	0.643	10^{-4}	0	0.166	0	10^{-4}	10^{-5}	0	0.076	0	10^{-5}	0	0	0	0.114

Appendix C

Transition bands in Bi-doped silica glass

Band	WL (nm)	E (cm^{-1})	Observed in
B1	910	10990	A
B2	810	12346	A, X
B3	415	24100	A, X
B4	375	26667	A, X
D1	1386	7215	A, X, M*
D2	465	21505	A, X, M
D3	350	28571	A, X, M

A — absorption/attenuation spectrum

X — excitation spectrum

M — MCD spectrum

M* — MCD observed via luminescence

Appendix D

List of publications

Papers

1. O. Laguta, H. El Hamzaoui, M. Bouazaoui, V. Arion and I. Razdobreev, "Anti-Stokes photoluminescence in Ga/Bi co-doped sol-gel silica glass", *Optics Letters*, 40(7), pp. 1591–1594 (2015).

2. O. Laguta, H. El Hamzaoui, M. Bouazaoui, V. Arion and I. Razdobreev, "Magnetic circular polarization of luminescence in bismuth-doped silica glass", *Optica*, 2(8), pp. 663–666 (2015).

3. O. Laguta, B. Denker, B. Galagan, S. Sverchkov and I. Razdobreev, "Magnetic optical activity in Bi-doped Mg-Al-Si glass", *Optical and Quantum Electronics*, 48(2), p. 123 (2016).

Conferences

1. O. Laguta, H. El Hamzaoui, V. Arion, M. Bouazaoui, I. Razdobreev, "On the optical centers in Bi/Ga(Al) co-doped silica glass", *International conference on Advanced Laser Technologies*, Cassis, France, October 6–10, 2014.

2. O. Laguta, H. El Hamzaoui, M. Bouazaoui, V. Arion, I. Razdobreev, "Magnetic circular polarization of luminescence in Ga/Bi and Al/Bi co-doped silica glasses", *The European Conference on Laser and Electro-Optics*, Munich, Germany, June 21–25, 2015, Paper # CE_P_14 (Poster).

3. O. Laguta, H. El Hamzaoui, V. Arion, M. Bouazaoui, I. Razdobreev, "Anti-Stokes photoluminescence in Ga/Bi co-doped sol-gel silica glass", *The European Conference on Laser and Electro-Optics*, Munich, Germany, June 21–25, 2015, Paper # CE_P_15 (Poster).

4. O. Laguta, B. Denker, B. Galagan, S. Sverchkov and I. Razdobreev, "Magnetic optical activity in Bi-doped Mg-Al-Si glass", *International conference on Advanced Laser Technologies*, Faro, Portugal, September 7–11, 2015, Paper #LS-I-9 (Invited talk).

5. O. Laguta, B. Denker, B. Galagan, S. Sverchkov, I. Razdobreev, "Magneto-optical investigations of bismuth-doped Mg-Al-Si glass. On the nature of near-infrared luminescence", *Russian Fiber Lasers*, Novosibirsk, Russia, September 5-9, 2016 (Invited talk)

Bibliography

[1] B. Disraeli, *Endymion*, London: Spottiswoode and Co., 1880, p. 331.

[2] J.-D. Colladon, "Sur les réflexions d'un rayon de lumiére à l'intérieur d'une veine liquide parabolique", *Comptes rendus*, 15, p. 800 (1842).

[3] J. Babinet, "Note sur la transmission de la lumière par des canaux sinueux", *Comptes rendus des séances de l ' Académie des sciences*, 15, p. 802 (1842).

[4] F. J. Duarte, *Tunable Laser Applications*, 3rd ed., New York: CRC Press, 2016, p. 428.

[5] M. Guy, D. Noske, A. Boskovic, and J. Taylor, "Femtosecond soliton generation in a praseodymium fluoride fiber laser.", *Optics letters*, 19(11), pp. 828–830 (1994).

[6] S. Firstov, S. Alyshev, V. Khopin, M. Melkumov, A. Guryanov, and E. Dianov, "Photobleaching effect in bismuth-doped germanosilicate fibers", *Optics Express*, 23(15), pp. 19226–19233 (2015).

[7] Y. Fujimoto and M. Nakatsuka, "Infrared luminescence from Bismuth-doped silica glass", *Japanese Journal of Applied Physics*, 40(3B), pp. L279–L281 (2001).

[8] Y. Fujimoto, "Local Structure of the Infrared Bismuth Luminescent Center in Bismuth-Doped Silica Glass", *Journal of the American Ceramic Society*, 93(2), pp. 581–589 (2010).

[9] O. Laguta, H. El Hamzaoui, M. Bouazaoui, V. Arion, and I. Razdobreev, "Magnetic circular polarization of luminescence in bismuth-doped silica glass", *Optica*, 2(8), pp. 663–666 (2015).

[10] Y. Fujimoto and M. Nakatsuka, "Optical amplification in bismuth-doped silica glass", *Applied Physics Letters*, 82(19), pp. 3325–3326 (2003).

[11] H.-T. Sun, J. Yang, M. Fujii, Y. Sakka, Y. Zhu, T. Asahara, N. Shirahata, M. Ii, Zh. Bai, J.-G. Li, and H. Gao, "Highly fluorescent silica-coated Bismuth-doped aluminosilicate nanoparticles for near-infrared bioimaging", *Small*, 7(2), pp. 199–203 (2011).

[12] M. Gaft, R. Reisfeld, G. Panczer, G. Boulon, T. Saraidarov, and S. Erlish, "The luminescence of Bi, Ag and Cu in natural and synthetic barite BaSO4", *Optical Materials*, 16(1-2), pp. 279–290 (2001).

[13] I. Bufetov and E. Dianov, "Bi-doped fiber lasers", *Laser Physics Letters*, 6(7), pp. 487–504 (2009).

[14] O. Laguta, B. Denker, B. Galagan, S. Sverchkov, and I. Razdobreev, "Magnetic optical activity in Bi-doped Mg–Al–Si glass", *Optical and Quantum Electronics*, 48(2), p. 123 (2016).

[15] E. Dianov, "Bismuth-doped optical fibers: a challenging active medium for near-IR lasers and optical amplifiers", *Light: Science Applications*, 1, pp. 1–7 (2012).

[16] E. Dianov, V. Dvoyrin, V. Mashinsky, A. Umnikov, M. Yashkov, and A. Gur'yanov, "CW bismuth fibre laser", *Quantum Electronics*, 35(12), pp. 1083–1084 (2005).

[17] M. Peng, G. Dong, L. Wondraczek, L. Zhang, N. Zhang, and J. Qiu, "Discussion on the origin of NIR emission from Bi-doped materials", *Journal of Non-Crystalline Solids*, 357(11-13), pp. 2241–2245 (2011).

[18] X.-G. Meng, J.-R. Qiu, M.-Y. Peng, D.-P. Chen, Q.-Zh. Zhao, X.-W. Jiang, and C.-Sh. Zhu, "Infrared broadband emission of bismuth-doped barium-aluminum-borate glasses", *Optics Express*, 13(5), p. 1635 (2005).

[19] J. Ren, J. Qiu, D. Chen, X. Hu, X. Jiang, and C. Zhu, "Luminescence properties of bismuth-doped lime silicate glasses", *Journal of Alloys and Compounds*, 463(1-2), pp. L5–L8 (2008).

[20] J. Ren, G. Dong, Sh. Xu, R. Bao, and J. Qiu, "Inhomogeneous broadening, luminescence origin and optical amplification in Bismuth-doped glass", *The Journal of Physical Chemistry A*, 112(14), pp. 3036–3039 (2008).

[21] A. Romanov, Z. Fattakhova, A. Veber, Ol. Usovich, E. Haula, V. Korchak, V. Tsvetkov, L. Trusov, P. Kazin, and V. Sulimov, "On the origin of near-IR luminescence in Bi-doped materials (II). Subvalent monocation Bi^+ and cluster Bi_5^{3+} luminescence in $AlCl_3/ZnCl_2/BiCl_3$ chloride glass", *Optics Express*, 20(7), pp. 7212–7220 (2012).

[22] J. Ren, L. Yang, J. Qiu, D. Chen, X. Jiang, and C. Zhu, "Effect of various alkaline-earth metal oxides on the broadband infrared luminescence from bismuth-doped silicate glasses", *Solid State Communications*, 140(1), pp. 38–41 (2006).

[23] T. Murata and T. Mouri, "Matrix effect on absorption and infrared fluorescence properties of Bi ions in oxide glasses", *Journal of Non-Crystalline Solids*, 353(24-25), pp. 2403–2407 (2007).

[24] S. Khonthon, Sh. Morimoto, Y. Arai, and Y. Ohishi, "Luminescence characteristics of Te- and Bi-doped glasses and glass-ceramics", *Journal of the Ceramic Society of Japan*, 115(1340), pp. 259–263 (2007).

[25] V. Sokolov, V. Plotnichenko, and E. Dianov, "Origin of broadband near-infrared luminescence in bismuth-doped glasses", *Optics Letters*, 33(13), pp. 1488–1490 (2008).

[26] B. Denker, B. Galagan, V. Osiko, I. Shulman, S. Sverchkov, and E. Dianov, "The IR emitting centers in Bi-doped Mg-Al-Si oxide glasses", *Laser Physics*, 19(5), pp. 1105–1111 (2009).

[27] M. Peng, C. Zollfrank, and L. Wondraczek, "Origin of broad NIR photoluminescence in bismuthate glass and Bi-doped glasses at room temperature", *Journal of Physics: Condensed Matter*, 21(28), p. 285106 (2009).

[28] M. Sharonov, A. Bykov, V. Petricevic, and R. Alfano, "Spectroscopic study of optical centers formed in Bi-, Pb-, Sb-, Sn-, Te-, and In-doped germanate glasses", *Optics Letters*, 33(18), pp. 2131–2133 (2008).

[29] I. Razdobreev, H. El Hamzaoui, V. Arion, and M. Bouazaoui, "Photoluminescence in Ga/Bi co-doped silica glass", *Optics Express*, 22(5), p. 5659 (2014).

[30] V. Sokolov, V. Plotnichenko, and E. Dianov, "The origin of near-IR luminescence in bismuth-doped silica and germania glasses free of other dopants: First-principle study", *Optical Materials Express*, 3(8), pp. 1059–1074 (2013).

[31] V. Sokolov, V. Plotnichenko, and E. Dianov, "Origin of near-IR luminescence in Bi_2O_3–GeO_2 and Bi_2O_3–SiO_2 glasses: first-principle study", *Optical Materials Express*, 5(1), pp. 163–168 (2015).

[32] E. Dianov, "Nature of Bi-related near IR active centers in glasses: state of the art and first reliable results", *Laser Physics Letters*, 12(9), p. 095106 (2015).

[33] E. Solomon, E. Pavel, K. Loeb, and C. Campochiaro, "Magnetic circular dichroism spectroscopy as a probe of the geometric and electronic structure of non-heme ferrous enzymes", *Coordination Chemistry Reviews*, 144, pp. 369–460 (1995).

[34] E. Solomon, T. Brunold, M. Davis, J. Kemsley, S.-K. Lee, N. Lehnert, Fr. Neese, A. Skulan, Y.-Sh. Yang, and J. Zhou, "Geometric and Electronic Structure/Function Correlations in Non-Heme Iron Enzymes", *Chemical Reviews*, 100(1), pp. 235–350 (2000).

[35] W. Mason, *A practical guide to magnetic circular dichroism spectroscopy*, New Jersey: John Wiley & Sons, Inc., 2008, p. 322.

[36] F. Liu, L. Biadala, A. Rodina, D. Yakovlev, D. Dunker, C. Javaux, J.-P. Hermier, A. Efros, B. Dubertret, and M. Bayer, "Spin dynamics of negatively charged excitons in CdSe/CdS colloidal nanocrystals", *Physical Review B*, 88(3), p. 035302 (2013).

[37] J.-M. Spaeth, J. Niklas, and R. Bartram, *Structural Analysis of Point Defects in Solids*, vol. 43, Springer Series in Solid-State Sciences, Berlin, Heidelberg: Springer, 1992, p. 287.

[38] B. Henderson and G. F. Imbusch, *Optical Spectroscopy of Inorganic Solids*, New York: Oxford University Press, 2006, p. 645.

[39] S. Geschwind, G. Devlin, R. Cohen, and S. Chinn, "Orbach relaxation and hyperfine structure in the excited E (2E) state of Cr^{3+} in Al_2O_3", *Physical Review*, 308(4), A1087 (1965).

[40] K. Murata, Y. Fujimoto, T. Kanabe, H. Fujita, and M. Nakatsuka, "Bi-doped SiO_2 as a new laser material for an intense laser", *Fusion Engineering and Design*, 44, p. 437 (1999).

[41] L. Skuja, "Optically active oxygen-deficiency-related centers in amorphous silicon dioxide", *Journal of Non-Crystalline Solids*, 239(1-3), pp. 16–48 (1998).

[42] H. Davis, N. Bjerrum, and G. Smith, "Ligand field theory of $p^{2,4}$ configurations and its application to the spectrum of Bi^+ in molten salt media", *Inorganic Chemistry*, 6(6), pp. 1172–1178 (1967).

[43] A. Okhrimchuk, L. Butvina, E. Dianov, N. Lichkova, V. Zagorodnev, and
      K. Boldyrev, "Near-infrared luminescence of RbPb$_2$Cl$_5$:Bi crystals", *Optics
      Letters*, 33(19), p. 2182 (2008).

[44] J. Ruan, L. Su, J. Qiu, D. Chen, and J. Xu, "Bi-doped BaF$_2$ crystal for broad-
      band near-infrared light source", *Optics Express*, 17(7), pp. 5163–5169 (2009).

[45] L. Su, J. Yu, P. Zhou, H. Li, L. Zheng, Y. Yang, F. Wu, H. Xia, and J. Xu,
      "Broadband near-infrared luminescence in γ-irradiated Bi-doped α-BaB$_2$O$_4$
      single crystals", *Optics Letters*, 34(16), pp. 2504–2506 (2009).

[46] A. Romanov, A. Veber, Z. Fattakhova, D. Vtyurina, M. Kouznetsov, K. Zara-
      menskikh, I. Lisitsky, V. Korchak, V. Tsvetkov, and V. Sulimov, "Spectral
      properties and NIR photoluminescence of Bi+ impurity in CsCdCl$_3$ ternary
      chloride", *Journal of Luminescence*, 149, pp. 292–296 (2014).

[47] R. Bartram, M. Fockele, F. Lohse, and J.-M. Spaeth, "Crystal-field model of
      the Pb^0(2) centre in SrF$_2$", *Journal of Physics: Condensed Matter*, 1(1), pp. 27–
      34 (1989).

[48] I. Razdobreev, H. El Hamzaoui, L. Bigot, V. Arion, G. Bouwmans, A. Le
      Rouge, and M. Bouazaoui, "Optical properties of Bismuth-doped silica core
      photonic crystal fiber", *Optics Express*, 18(19), p. 19479 (2010).

[49] O. Shestakov, R. Breidohr, H. Demes, K. Setzer, and E. Fink, "Electronic
      states and spectra of BiO", *Journal of Molecular Spectroscopy*, 190(1), pp. 28–
      77 (1998).

[50] J. Ren, Ch. Dan-Ping, Y. Guang, X. Yin-Sheng, Z. Hui-Dan, and Ch. Guo-
      Rong, "Near infrared broadband emission from Bismuth–Dysprosium codoped
      chalcohalide glasses", *Chinese Physics Letters*, 24(7), pp. 1958–1960 (2007).

[51] K. Schwartz, D. Leong, and R. McConville, "Structural chemistry of synthetic cordierite: Evidence for solid solutions and disordered compositional domains in Bi-flux-grown Mg-cordierites", *Physics and Chemistry of Minerals*, 20(8), pp. 563–574 (1994).

[52] B. Denker, B. Galagan, V. Osiko, I. Shulman, S. Sverchkov, and E. Dianov, "Absorption and emission properties of Bi-doped Mg–Al–Si oxide glass system", *Applied Physics B*, 95(4), pp. 801–805 (2009).

[53] B. Denker, B. Galagan, V. Osiko, I. Shulman, S. Sverchkov, and E. Dianov, "Factors affecting the formation of near infrared-emitting optical centers in Bi-doped glasses", *Applied Physics B*, 98(2-3), pp. 455–458 (2010).

[54] E. Dianov, "On the nature of near-IR emitting Bi centres in glass", *Quantum Electronics*, 40(4), pp. 283–285 (2010).

[55] M Sharonov, A Bykov, and R R Alfano, "Excitation Relaxation Pathways in Bi- and Other 5p- and 6p - Elements Doped Germanate Laser Glasses", *Journal of the Optical Society of America B*, 26(7), pp. 1435–1441 (2009).

[56] M. Peng, C. Wang, D. Chen, J. Qiu, X. Jiang, and C. Zhu, "Investigations on bismuth and aluminum co-doped germanium oxide glasses for ultra-broadband optical amplification", *Journal of Non-Crystalline Solids*, 351(30-32), pp. 2388–2393 (2005).

[57] A. Abragam and B. Bleaney, *Electron paramagnetic resonance of transition ions*, vol. 1, Oxford: Oxford University Press, 1970, p. 911.

[58] J. H. Van Vleck, "Paramagnetic relaxation times for titanium and chrome alum", *Physical Review*, 57(5), pp. 426–447 (1940).

[59] R Orbach, "Spin-Lattice Relaxation in Rare-Earth Salts", *Proceedings of the Royal Society of London A: Mathematical, Physical and Engineering Sciences*, 264(1319), pp. 458–484 (1961).

[60] S. Piepho and P. Schatz, *Group theory in spectroscopy: with applications to magnetic circular dichroism*, New York: John Wiley & Sons, Inc., 1983.

[61] R. Serber, "The theory of the Faraday effect in molecules", *Physical Review*, 41(4), pp. 489–506 (1932).

[62] P. Stephens, "Excited state magnetic moments through moment analysis of magnetic circular dichroism", *Chemical Physics Letters*, 2(4), pp. 241–244 (1968).

[63] P. Stephens, "Theory of magnetic circular dichroism", *The Journal of Chemical Physics*, 52(7), pp. 3489–3516 (1970).

[64] J. Riehl, "General theory of circularly polarized emission and magnetic circularly polarized emission from molecular systems", *The Journal of Chemical Physics*, 65(3), pp. 1011–1021 (1976).

[65] J. Riehl and F. Richardson, "Theory of magnetic circularly polarized emission", *The Journal of Chemical Physics*, 66(5), p. 19881998 (1977).

[66] P. Schatz, R. Mowery, and E. Krausz, "M.C.D./M.C.P.L. saturation theory with application to molecules in $D_{\infty h}$ and its subgroups", *Molecular Physics*, 35(6), pp. 1537–1557 (1978).

[67] M. Fockele, F. Lohse, J.-M. Spaeth, and R. Bartram, "Identification and optical properties of axial lead centres in alkaline-earth fluorides", *Journal of Physics: Condensed Matter*, 1(1), pp. 13–26 (1989).

[68] S. Zhou, N. Jiang, B. Zhu, H. Yang, S. Ye, G. Lakshminarayana, J. Hao, and J. Qiu, "Multifunctional bismuth-doped nanoporous silica glass: From blue-green, orange, red, and white light sources to ultra-broadband infrared amplifiers", *Advanced Functional Materials*, 18(9), pp. 1407–1413 (2008).

[69] J. S. Griffith, *The Theory of Transition-Metal Ions*, Cambridge: Cambridge University Press, 1961, p. 455.

[70] C. E. Moore, *National Bureau of Standarts Circular 467*, vol. 3, Washington, D. C.: U. S. Government Pronting Office, 1958, p. 245.

[71] O. Laguta, H. El Hamzaoui, M. Bouazaoui, V. Arion, and I. Razdobreev, "Anti-Stokes photoluminescence in Ga/Bi co-doped sol-gel silica glass", *Optics Letters*, 40(7), pp. 1591–1594 (2015).

[72] M. Kalita, S. Yoo, and Jayanta Sahu, "Bismuth doped fiber laser and study of unsaturable loss and pump induced absorption in laser performance.", *Optics express*, 16(25), pp. 21032–21038 (2008).

[73] M. Bouazaoui, B. Capoen, H. El Hamzaoui, L. Bigot, and G. Bouwmans, "Monoliths of high-purity silica and its synthesis process", *European Patent*, EP2174916A (2010).

[74] H. El Hamzaoui, L. Courthéoux, V. N. Nguyen, E. Berrier, A. Favre, L. Bigot, M. Bouazaoui, and B. Capoen, "From porous silica xerogels to bulk optical glasses: The control of densification", *Materials Chemistry and Physics*, 121(1-2), pp. 83–88 (2010).

[75] I. Razdobreev, H. El Hamzaoui, V. Ivanov, E. Kustov, B. Capoen, and M. Bouazaoui, "Optical spectroscopy of bismuth-doped pure silica fiber preform", *Optics Letters*, 35(9), p. 1341 (2010).

[76] M. Peng, B. Sprenger, M. Schmidt, H. Schwefel, and L. Wondraczek, "Broadband NIR photoluminescence from Bi-doped $Ba_2P_2O_7$ crystals: Insights into the nature of NIR-emitting Bismuth centers", *Optics Express*, 18(12), p. 12852 (2010).

[77] J. F. Reintjes and G. T. Coate, *Principles of Radar*, New York: McGraw-Hill, 1952, p. 986.

[78] C. P. Poole, *Electron Spin Resonance*, New York: John Wiley, 1983, p. 780.

[79] C. G. Montgomery, *Technique of Microwave Measurements*, 1st ed., New York: McGraw-Hill, 1948, p. 959.

[80] A. A. Antipin and V. S. Zapasskii, "Faraday effect and and optical detection of EPR in crystals and glasses", *Optics and Spectroscopy*, 50, pp. 263–270 (1981).

[81] A. A. Antipin and V. S. Zapasskii, "Laser polarimetric investigations of EPR and relaxation in glasses", *Physics of Solid State*, 24, pp. 1843–1849 (1982).

[82] V. Zapasskii, "Optical detection of spin-system magnetization in rare-earth-activated crystals and glasses", *Spectroscopy of Solids Containing Rare-Earth Ions*, ed. by A. A. Kaplyanskii and R. M. Macfarlane, North-Holland: Elsevier Science Publishers, 1987, pp. 674–811.

[83] E. B. Alexandrov and V. S. Zapasskii, *Laser magnetic spectroscopy*, Moscow: Nauka, 1986, p. 280.

[84] J. J. Davies, "Signal enhancement by field modulation in optically-detected magnetic resonance experiments", *Journal of Physics C: Solid State Physics*, 11(9), pp. 1907–1919 (1978).

[85] L. Landau and E. Lifshitz, *Statistical Physics*, 2nd ed., Oxford: Pergamon press, 1969.

[86] R. White, *Quantum Theory of Magnetism*, 3rd ed., Springer Series in SOLID-STATE SCIENCES, Berlin, Heidelberg: Springer Berlin Heidelberg, 2007, p. 362.